Masterarbeit

Zur Erlangung des akademischen Grades Master of Science

Thema der Arbeit:

Design, Aufbau und Charakterisierung eines optischen Systems zum Fangen und Transport einzelner Atome in einem Experiment zur Resonator-Quantenelektrodynamik

Set-up, Characterization of an optical system to trap and transport single atoms in a cavity quantum electrodynamics experiment.

eingereicht von:	Lucas Pache
Gutachter/innen:	Prof. Dr. Arno Rauschenbeutel Dr. Tim Schröder

Eingereicht am Institut für Physik der Humboldt-Universität zu Berlin am: 14.01.2022

CONTENTS

INTRODUCTION 1

1. EXPERIMENTAL OVERVIEW 3
1.1 Cooling and Trapping of Neutral Atoms . . . 3
  1.1.1 Magneto-optical Trap . . . 3
  1.1.2 Dipole Trap . . . 6
1.2 Optical Setup . . . 9

2. FOCUS SPOT CHARACTERIZATION 15
2.1 Knife Edge Method . . . 16
  2.1.1 Test Measurement . . . 20
  2.1.2 Lens Characterization Measurements . . . 23
2.2 Imaging Method . . . 26
  2.2.1 Testing the Microscope Setup . . . 26
  2.2.2 Lens Characterization Measurements . . . 30
2.3 Scanning Nanofiber Method . . . 34
  2.3.1 Bare Nanofiber . . . 34
  2.3.2 Erbium-Doped Nanofiber . . . 37
  2.3.3 Experimental Challenges . . . 37
  2.3.4 Lens Characterization Measurements . . . 42
2.4 Summarizing the Characterization Methods . . . 45

3. TRAPPING OF SINGLE ATOMS 47
3.1 Observation of Single Atoms and Atom Lifetime . . . 49
3.2 Hanbury-Brown Twiss Measurment . . . 51

4. TOWARDS ATOM TRANSPORT INTO THE RESONATOR'S WGM 55
4.1 Atom Transport with an Electric Tunable Lens . . . 56
  4.1.1 Working Principle of Liquid Lenses . . . 56
  4.1.2 Characterizing the Electric Tunable Lens . . . 57
  4.1.3 Transient Behavior . . . 57
  4.1.4 Pointing Stability . . . 64
4.2 Discussion of the Standing Wave Trapping Potential . . . 66
  4.2.1 Trapping Near the Resonator's Surface . . . 66
  4.2.2 Measuring a Standing Wave Potential . . . 68

SUMMARY AND OUTLOOK 73

BIBLIOGRAPHY 74

ABSTRACT

Whispering-gallery-mode resonators are a class of optical resonators that combine ultra-high Q-factors with near lossless in- and out coupling of light using optical nanofibers. Furthermore, they provide a chiral (i.e. direction-dependent) light-matter interaction that allows for deterministic control of light in quantum applications. In this thesis, we developed an optical setup which should allow for deterministic trapping of single ^{85}Rb atoms and their transport into the evanescent field of the resonator's whispering-gallery-mode with the goal of reaching the strong coupling regime of cavity quantum electrodynamics. For this, we set up and characterized a confocal microscope to trap single atoms with an optical dipole trap that operates within the collisional blockade regime and that allows us to collect the atoms fluorescence. Using our configured microscope setup, we successfully trapped single ^{85}Rb atoms inside the dipole trap. From the measured telegraph-like signal and the measured photon anti-bunching, we conclude that only single atoms are trapped inside the optical tweezer. Since the cold Rubidium atoms are prepared in the magneto-optical trap at a distance of 1 mm from the resonator's surface, we have to transport the atoms inside the dipole trap to the resonator's surface. The atom transport should be realized by changing the focus position of the dipole trap with an electric tunable lens. In this thesis, we will investigate the feasibility of this method of atom transport by characterizing the switching behavior of the electric tunable lens and its effect on the trap focus position. When the focus of the dipole trap reaches the resonator's surface during the atom transport, a strong partial standing wave trapping potential is formed due to interference from the incoming and retroreflected beams. To counter this effect, we plan to use a spatial light modulator to generate a trapping field composed of higher-order Laguerre-Gaussian modes. The different standing wave patterns generated by these beams will largely remove the standing wave pattern and allow for a deterministic transport of a single atom to a distance of around 200 nm from the resonator's surface. In order to characterize this trapping potential, we developed a method to directly measure the electric field modulation of the trap laser close to the resonator's surface based on an Erbium-doped optical nanofiber. A proof-of-concept measurement of this method was successfully realized during this thesis.

KURZFASSUNG

Flüstergalleriemoden-Resonatoren sind eine Klasse neuartiger optischer Bauelemente, welche nicht nur eine hohe Güte besitzen, sondern auch ein nahezu verlustfreies Ein- und Auskoppeln von Licht mit optischen Nanoglasfasern ermöglichen. Des Weiteren weisen diese Resonatoren eine chirale (d.h. richtungsabhängige) Licht-Materie Wechselwirkung auf, welche die deterministische Kontrolle von Licht in Quantentechnologien ermöglichen kann. Im Rahmen dieser Masterarbeit haben wir einen optischen Aufbau entwickelt, der das Fangen von einzelnen ^{85}Rb-Atomen und deren deterministischen Transport in die Flüstergalleriemode an der Oberfläche des Resonators ermöglichen soll. Bei der Kopplung des Atoms mit dem evaneszenten Feld der Flüstergalleriemode kann das starke Kopplungsregime des Resonator-Quantenelektrodynamik erreicht werden. Zur Realisierung des Vorhabens haben wir ein Konfokalmikrosop, welches eine Dipolfalle zum Fangen einzelner Atome darstellt, aufgebaut und charakterisiert. Außerdem ist der Aufbau des Konfokalmikroskops so gestaltet, dass es uns ermöglicht, die Fluoreszenz eines einzelnen gefangenen Atoms zu detektieren. Mit dem charakterisierten Aufbau war es uns erfolgreich möglich, einzelne ^{85}Rb-Atome in der Dipolfalle zu fangen. Dieses Ergebnis wurde durch den Nachweis von Photonen-Antibunching im Fluoreszenzlicht nochmals bestätigt. In unserem Experiment werden die kalten Rubidium Atome in einer magneto-optischen Falle in einer Entfernung von 1 mm zur Oberfläche des Resonators präpariert. Daher müssen wir die Atome zum Resonator in der optischen Dipolfalle transportieren, um Experimente in der Resonator-Quantenelektrodynamik durchführen zu können. Durch die Fokusverschiebung der Dipolfalle mit Hilfe einer elektrisch einstellbaren Linse soll der Atomtransport durchgeführt werden. Im Rahmen dieser Arbeit untersuchen wir, ob solch eine Linse zum Atomtransport in unserem Experiment benutzt werden kann. Dazu analysieren wir die Fokusstabilität und das transiente Antwortverhalten der elektrisch einstellbaren Linse. Am Ende des Transportprozesses wird der Fokus der Dipolfalle auf der Resonatoroberfläche liegen. Durch die Interferenz des einkommenden Srahls mit dem von der Oberfläche zurückreflektieren Srahl wird ein stehwellenförmiges Fallenpotential erzeugt, welches das Fangen von Atomen nahe an der Resonatoroberfläche unwahrscheinlich macht. Um diesem Effekt entgegenzuwirken, planen wir einen räumlichen Lichtmodulator zu verwenden, der eine Überlagerung von Laquerre-Gaußmoden erzeugt. Die Überlagerung der verschiedenen Stehwellenmuster der Strahlen führen dann zur Unterdrückung des stehwellenförmiges Fallenpotentials, sodass ein deterministisches Fangen von Atomen in einer Entfernung von 200 nm der Resonatoroberfläche ermöglicht werden sollte. Zur Charakterisierung dieser Potentiale haben wir eine Methode entwickelt, die es uns erlaubt, mit Hilfe einer Erbium-dotierten optischen Nanoglasfaser, die Modulation des elektrischen Feldes im Stehwellenpotenzial direkt zu messen.

INTRODUCTION

Quantum electrodynamics (QED) describes, among other things, the interaction of the quantized electromagnetic field with light emitters i.e. atoms. A fully quantum mechanical treatment of one atom interacting with a single mode of the electromagnetic field was developed by Jaynes and Cummings in 1963 [1]. The description laid down the building blocks of quantum optics as it describes quantized energy levels and its non-linear scaling as well as the existence of Rabi oscillations and their collapse and revival. However in free space, the coherent interaction between a single atom and a mode of the electromagnetic field is typically very weak. In order to study the coherent behavior of such a system, the light-atom interaction can be enhanced by confining the volume of the electromagnetic field in a optical cavity. In these so-called cavity quantum electrodynamics (CQED) experiments, the light and the atom can be strongly coupled in the sense that the rate of coherent energy exchange between the light field and atom exceeds the incoherent damping of the system, given by the spontaneous emission rate and the energy loss rate of the cavity. The importance of the achievements in this field were underlined by rewarding Serge Haroche the Nobel Prize in physics in 2012 for his experiments studying light-matter interaction [2]. Using high finesse Fabry-Perot cavities, the trapping of single atoms inside such a resonator mode was achieved [3][4], which led to gound-breaking experiments [5] including fundamental tests of quantum mechanics [6].
In our group we use a different, novel class of optical resonators: so-called whispering-gallery-mode (WGM) microresonators [7] [8]. These types of resonator guide light in high quality whispering-gallery-modes near the curved surface by means of frustrated total internal reflection. At the same time, they offer near lossless in and out-coupling of light using optical nanofiber waveguides [9]. Additionally, WGM microresonators offer chiral, i.e. direction-dependent, light-matter interaction that allows for deterministic control of light in quantum applications [10]. In order to reach the strong coupling regime of CQED, the atom has to couple to the evanescent field of the whispering-gallery-mode at a distance of 100 nm to 200 nm from the resonator's surface. Furthermore, the atoms have to be trapped within that mode to reach the interaction times exhibited by Fabry-Perot cavities. Recently, our group demonstrated the strong coupling of single trapped ^{85}Rb atoms to the resonator's WGM [11] using a retroreflected optical tweezer for trapping [12]. However, this milestone was achieved with a probabilistic trap loading technique which in turn led to relatively hot atoms limiting the interaction time and experimental efficiency.

In the scope of this thesis, we therefore developed and characterized a new optical system which should allow for a more controlled approach to trap single atoms at the WGM resonator. Using a magneto-optical trap (MOT), we prepare a cloud of Rubidium atoms at a distance of 1 mm from the resonator's surface. Afterwards, we employ a tightly focused dipole trap with a waist of around 2 µm to pick a single atom from the cloud of cold atoms inside the MOT. Next, we transport the single ^{85}Rb-Atom from the MOT-position to the resonator's surface by changing the focus position of the dipole trap using an electric tunable lens. When the focus of the dipole trap beam reaches a position close to the resonator's surface, the incident beam and the beam reflected by the surface creates a standing wave trapping potential what will prevent the atom from reaching the resonator's surface. In order to maximize the coupling strength of the atom with resonator's whispering-gallery-mode, we want to trap the atom in the potential minima closest to the resonator, which is at a distance of $\lambda/4$ from the resonator's surface. Therefore to reduce the standing wave potential, we use a spatial light modulator to generate a superposition of higher-order Laguerre-Gaussian modes for our optical dipole trap. As these higher-order beams are subject to a different Gouy phase, the individual standing wave potentials quickly dephase with respect to each other such that only a potential minima at a distance of $\lambda/4$ from the surface remains. This allows us to realize nearly deterministic transport of a of single ^{85}Rb-atoms into the evanescent field of the whispering-gallery mode of the microresonator and to reach the strong coupling regime.

In the first chapter of this thesis, I explain the concepts needed to understand atom cooling and trapping within a MOT and dipole trap. Furthermore, I introduce the planned optical apparatus which will be used to realize the trapping of single ^{85}Rb-atoms inside the whispering-gallery mode of the microresonator. In the second chapter, I characterize the focus spot region of the confocal microscope used to trap single atoms within the dipole trap and to collect the atom's fluorescence light. In order to characterize the focus spot region, I employ three different techniques to measure the beam waist. In the first method, I use a sharp knife edge to cut laterally through the focus spot region in order to observe a decrease of power on a photo diode. As a second method, I image the focus spot using a high-quality optical microscope. Furthermore, to get a high resolution in situ image of the beam focus, we develop a third method based on a small diameter ($d = 300\,\mathrm{nm}$) Erbium-doped optical nanofiber which I scan through the focus spot region while collecting the photons scattered into the fiber. In the third chapter, I report on the successful trapping of single atoms inside the dipole trap which we verify by measuring the second order correlation function of the detected fluorescence light. In the last chapter, I will discuss the first steps towards to realization of atom transport and the potential effect of the transport via an electric tunable lens on the atoms. For the successful transport it is crucial to suppress the standing wave pattern. Thus, we also performed a first proof of concept measurement based with the already introduced Erbium-doped nanofiber method to directly measure and characterize the standing wave trapping potential. At the end of this thesis, I will give an outlook on the next steps needed to realize the trapping of single atoms within the resonator's WGM.

1

Experimental Overview

The first chapter gives an overview of the planned experimental setup. Due to the complexity of the apparatus, we split this chapter into two parts. The first part explains the theoretical concepts needed to understand the preparation of cold atoms inside a magneto-optical trap and the trapping of atoms inside a optical dipole trap. In the second part we describe the planned experimental setup required to trap single ^{85}Rb atoms and collect their florescence. Furthermore, we outline the techniques and apparatus needed to transport the trapped atoms close to the surface of a whispering-gallery-mode (WGM) resonator.

1.1 Cooling and Trapping of Neutral Atoms

Before we start to present the experimental setup for trapping, detecting and transporting single atoms, we have to explain how laser-cooled atoms are prepared. Thus, we give a brief introduction to the operation principles of magneto-optical traps and the trapping of single atoms in a dipole trap.

1.1.1 Magneto-optical Trap

A magneto-optical trap (MOT) consists of a six-laser beam arrangement that a region of overlap with each beam is created in a certain region. In our experiment, these beams are 16 MHz red detuned to the D2-transition ($5^2S_{1/2} \rightarrow 5^2P_{3/2}$) of ^{85}Rb at 780 nm to perform laser cooling. At the location of the atoms, where the laser beams overlap, a magnetic quadrupole field is applied such that the interaction of the atoms with polarized laser light leads to a velocity and position dependent force that at the same time cools and traps the atoms. The idea of cooling neutral atoms with laser light was proposed by T. Hänsch and A. Schawlow [13] in 1975 while Raab and coworkers [14] demonstrated the first working MOT at Bell Laboratories in 1987. The description of the working principle of a MOT follows the derivation presented in the book of Fox [15].

First, we introduce the concept of laser cooling. Let's consider an atom with transition angular frequency ω_0 moving into the +x-direction with velocity v_x. Counter-propagating to the moving atom, the electromagnetic wave of a laser is propagating with frequency $\omega_L = 2\pi c/\lambda$ slightly red-detuned to the transition frequency ω_0 by $\delta = \omega_0 - \omega_L$. Due to the Doppler effect the frequency of the laser in the frame of reference moving with the atom is shifted by

$$\omega_L' = \omega_L \left(1 + \frac{v_x}{c}\right) = (\omega_0 + \delta)\left(1 + \frac{v_x}{c}\right) \approx \omega_0 + \delta + \frac{v_x}{c}\omega_0 \tag{1.1}$$

with $v_x \ll c$ and $\delta \ll \omega_0$. Consequently, the laser will be closer to resonance with the atoms moving into the +x-direction. When the atom is subject to the laser beam, it will absorb a photon and subsequently be in an exited state. After the radiative lifetime τ, the atom re-emits a photon with the same frequency by spontaneous emission in a random direction. Since the absorption process transfers the photon momentum $\hbar k$ in -x-direction onto the atom while the emission occurs in a random direction with no average momentum transfer, the total momentum change of the atom is

$$\Delta p_x = \hbar k. \tag{1.2}$$

Averaging over many absorption-emission cycles of the atom, this process will lead to a scattering force given by the photon momentum and the scattering rate [16] as

$$F_{scatt} = -\hbar k \cdot R(I, \delta). \tag{1.3}$$

For a laser with Intensity I, that force is given by

$$F_{scatt} = -\frac{\hbar k \gamma}{2} \cdot \left(\frac{I/I_S}{1 + I/I_S + \left[2\left(\omega_L - \omega_0 + k v_x\right)/\gamma\right]^2} \right) = F_{scatt}(w_L), \tag{1.4}$$

where is $\gamma = 1/\tau$ and I_S depicts the saturation intensity of the atomic transition. At very high intensities $I \to \infty$ the scattering force is limited by the maximum rate of the spontaneous emission $\gamma/2$ as the population of the ground and exited level in a two-level system approach 1/2. In order to cool atoms in all three spatial directions (x,y,z), a six-laser beam arrangement consisting of three pairs of counter-propagating laser beams along each direction is needed. On every axes with counter-propagating laser beams, the difference between the scattering force in the positive and negative spatial dimension (x,y,z) can be expressed as:

$$F = F_{scatt}(\omega_L - \omega_0 - kv) - F_{scatt}(\omega_L - \omega_0 - kv) \simeq -2\frac{\partial F_{scatt}}{\partial \omega_L} kv. \tag{1.5}$$

Here we assumed small atomic velocities $|kv_{x,y,z}| \ll \gamma$ and $|kv_{x,y,z}| \ll \delta$. The Doppler effect shifts the red-detuned laser in the frame of the moving atom closer to resonance and increases the scattering rate. The resulting imbalance of the directional scattering forces slows the atom down, which is called Doppler cooling. The force shows a linear dependence on the velocity with the damping coefficient β as:

$$F = -\beta v. \tag{1.6}$$

The damping coefficient is given for intensities below the saturation intensity by

$$\beta = 2k\,\frac{\partial F_{scatt}}{\partial \omega_L} = 4\hbar k^2 \frac{I}{I_S} \frac{-2\delta/\gamma}{\left[1 + (2\delta/\gamma)^2\right]^2}. \tag{1.7}$$

Because the atom experiences a decelerating force proportional to the its velocity v as in a viscous fluid, this technique of cooling atoms using counter-propagating laser beams is called optical molasses. The cooling forces reduce the kinetic energy of the atom to a minimum energy limited by the recoil heating of the atom when undergoing spontaneous emission. Therefore, the equilibrium kinetic energy is reached when the cooling and heating are equal. It is given by

$$E_{min} = k_B T_{Doppler} \quad \text{with} \quad T_{Doppler} = \frac{\gamma \hbar}{2k_B}, \tag{1.8}$$

where $T_{Doppler}$ is the minimum temperature or Doppler temperature.*

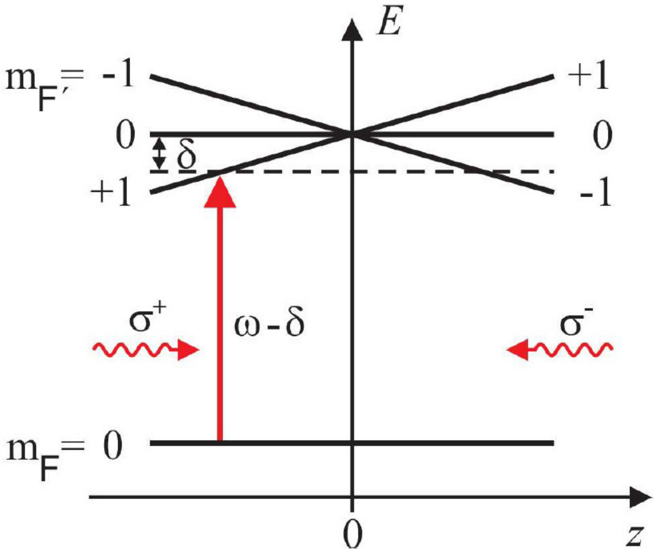

Figure 1.1: Position dependent Zeeman splitting of the magnetic sub levels of the $F = 1$ exited state along the z-axes in the magnetic quadrapole field (visualization adapted from [17])

In order to not just cool but also to confine atoms in a given volume, an additional position dependent force is needed. Therefore, a magnetic quadrapole field - typically produced by two coils in anti-Helmholtz configuration - is applied to the optical molasses such that the minimum of the B-field coincides with the overlap region of the beam arrangement. The magnetic field B leads to a spatial-dependent Zeeman shift of the atomic magnetic sub-levels $M_J = 0, \pm 1$ as

$$E = g\mu_B |\vec{B}(\vec{r})| M_J. \tag{1.9}$$

Here g is the Landé factor and μ_B is Bohr's magneton. For one spatial dimension (z) this energy level shift is presented in Fig. 1.1. If the incident laser beams are σ_+ or σ_- polarized, conservation of angular momentum leads to excitation of the atom in the $M_J = \pm 1$ transition. If two counter propagating lasers have a frequency $\omega_L = \omega_0 - \delta$ with σ_+ polarization for the beam propagating in the positive z-direction and σ_- polarization for the beam propagating in the negative z-direction, the light field predominantly excites the atoms to the magnetic sub-levels which are shifted into resonance by the magnetic field as showcased in fig. 1.1. Thus, an atom traveling in the z-direction away from the point of zero magnetic field and interacting with the σ_- polarized light is pushed back by the scattering force and is therefore trapped in the center region of the MOT.

---

[*] Note that in typical laser cooling setups much smaller temperatures are reached as other, so-called sub-Doppler cooling mechanisms like Sisyphus cooling can occur. For a description of these mechanisms see for example [16].

1.1.2 DIPOLE TRAP

In a typical MOT many 10^6 atoms are trapped. As for the planned experiment we want to work with only one atom, we need a technique to pick out just a single Rubidium atom. This is done by using an optical tweezer or dipole trap. The main idea of a dipole trap is to induce an oscillating electric dipole in an atom by the electro-magnetic field of a so-called trapping laser. If the laser frequency is red-detuned to the atomic transition, the introduced dipole is attracted towards the high intensity regions created by the same laser. This technique was first proposed by Ashkin in 1978 [18]. Due to the relevance of the general concepts of optical tweezers in atomic and biological physics, the Nobel Prize in Physics was awarded to Ashkin in 2018 [19]. In the following, the basic equations to understand the physical principle of a dipole trap are described by modeling the atom and its electron as a classical oscillator in a classical electromagnetic field. The explanations in this section are taken from [20].

Let's consider the electromagnetic field $\vec{E}$ of a laser at the driving frequency ω with unit polarization vector $\hat{e}$ as

$$\vec{E}(\vec{r},t) = \tilde{E}(\vec{r})e^{-i\omega t}\hat{e} + c.c.\,, \tag{1.10}$$

where c.c. stands for the complex conjugate term and $\tilde{E}(\vec{r})$ is the complex field amplitude. The field then induces an atomic dipole moment $\vec{p}$ at the same frequency ω:

$$\vec{p}(t) = \tilde{p}e^{-i\omega t}\hat{e} + c.c.\,. \tag{1.11}$$

The complex polarizability α then connects both amplitudes $\tilde{p}$ and $\tilde{E}$ as

$$\tilde{p} = \alpha\tilde{E}(\vec{r}). \tag{1.12}$$

By calculating the time average over the rapidly oscillating terms (denoted by $\langle\cdots\rangle$) of the induced dipole moment and the driving field, we get the potential energy of the atom as

$$U(\vec{r}) = -\frac{1}{2}\langle\vec{p}\vec{E}\rangle = -\frac{1}{2\epsilon_0 c}\mathrm{Re}(\alpha)I(\vec{r})\,. \tag{1.13}$$

Here I is the intensity of the electromagnetic field, ϵ_0 the vacuum permittivity and c the speed of light. From the potential $U(\vec{r})$ we can extract the dipole force by applying the gradient:

$$\vec{F}(\vec{r}) = -\nabla U(\vec{r}) = \frac{1}{2\epsilon_0 c}\mathrm{Re}(\alpha)\nabla I(\vec{r})\,. \tag{1.14}$$

From the short time average of the time derivative of the induced dipole and the field, we are able to calculate the power absorbed by the atom from the driving laser field:

$$P = \langle\dot{\vec{p}}\vec{E}\rangle = \frac{\omega}{\epsilon_0 c}\mathrm{Im}(\alpha)I(\vec{r})\,. \tag{1.15}$$

From this we obtain the photo scattering rate of an atom by dividing P by the energy $E = \hbar\omega$ of a photon

$$\Gamma_{sc} = \frac{1}{\hbar\epsilon_0 c}\mathrm{Im}(\alpha)I(\vec{r})\,. \tag{1.16}$$

The polarizability α can be calculated by applying the Lorentz oscillator model to the atom in the electromagnetic field of the laser. We consider an electron with mass m_e and elementary charge e elastically bound to the atom core. The system has a eigenfrequency ω_0 and is driven by the external electric field of the laser as given in Eq.(1.10) where we here assume that the field is polarized along the x-axis and is constant across the atom $\vec{E}(\vec{r},t) = E(t)$. The motion of such an oscillator is described by the inhomogeneous second order differential equation

$$\ddot{x} + \Gamma_\omega \dot{x} + \omega_0^2 x = -e\frac{E(t)}{m_e} \tag{1.17}$$

with Γ_ω being the damping rate caused by the dipole radiation of an oscillating electron. The polarizability α is connected with the spatial position x similar to Eq.(1.12) as

$$p(t) = -e\,\vec{r} = \alpha E(t). \tag{1.18}$$

Therefore, we can extract the polarizability from of the stationary solution of the differential equation as

$$\alpha = \frac{e^2}{m_e}\frac{1}{\omega_0^2 - \omega^2 + i\Gamma_\omega\,\omega} = 6\pi\epsilon_0 c^3 \frac{\Gamma}{w_0^2(\omega_0^2 - \omega^2 + i\Gamma\frac{\omega^3}{\omega_0^2})}\,. \tag{1.19}$$

For the second part of the equation we introduced the on-resonance damping rate as shown in [20] as

$$\Gamma = \left(\frac{w_0}{w}\right)^2 \Gamma_\omega \quad \text{and substituted} \quad \frac{e^2}{m_e} = 6\pi\epsilon_0 c^3 \frac{\Gamma_\omega}{w^2}\,. \tag{1.20}$$

We can now plug in Eq.(1.19) in the expressions Eq.(1.13) for the dipole potential as well as for the scatting rate (1.16) and obtain:

$$U(\vec{r}) = -\frac{3\pi c^2}{2\omega_0^3}\left(\frac{\Gamma}{\omega_0 - \omega} + \frac{\Gamma}{\omega_0 + \omega}\right) I(\vec{r}) \quad \text{and} \tag{1.21}$$

$$\Gamma_{sc}(\vec{r}) = -\frac{3\pi c^2}{2\hbar\omega_0^3}\frac{w^3}{w_0^3}\left(\frac{\Gamma}{\omega_0 - \omega} + \frac{\Gamma}{\omega_0 + \omega}\right)^2 I(\vec{r})\,. \tag{1.22}$$

In our experiment the detuning $\delta = \omega_0 - \omega$ is relatively close to resonance and it is therefore much smaller than the frequency of the transition, i.e. $\delta \ll \omega_0$. Thus, we can apply the rotating-wave approximation to neglect the counter-rotating terms in both equations. In this case, they simplify to:

$$U(\vec{r}) = \frac{3\pi c^2}{2w_0^3}\frac{\Gamma}{\delta}\,I(\vec{r}), \tag{1.23}$$

$$\Gamma_{sc}(\vec{r}) = \frac{3\pi c^2}{2\hbar w_0^3}\frac{\Gamma^2}{\delta^2}\,I(\vec{r})\,. \tag{1.24}$$

As we can see from Eq.(1.23) the sign of the dipole potential is directly dependent on the sign of the detuning δ. For a laser red-detuned to the resonance frequency of the atom ($\delta < 0$), the atom is attracted into the high intensity regions. Whereas for a blue detuned laser ($\delta > 0$) the atom will be repelled by the high intensity region. From both Eq.(1.23) and Eq.(1.24) we observe that the dipole potential scales as I/δ whereas the scatting rate scales as I/δ^2. Thus, in order to minimize the photon scattering rate for a particular potential depth we have to use a large detuning and a high intensity.

In our experiment we want to trap ^{85}Rb atoms. These alkali atoms offer closed optical transitions in a convenient spectral range and have a relatively large dipole moment. Because the spin-orbit coupling leads to the D-line doublet, we have to take into account contribution from the D2 line at 780.2 nm as well as from the D1-line at 795.0 nm to the dipole potential. As it is shown in [20], we can rewrite the dipole potential with the detuning δ from both lines for a linearly polarized dipole trap beam as:

$$U(\vec{r}) = -\frac{\pi c^2 \Gamma}{2\omega_0^3}\left(\frac{2}{\delta_{D2}} + \frac{1}{\delta_{D1}}\right) I(\vec{r})\,. \tag{1.25}$$

Here δ_{D1} and δ_{D2} are the detuning of the trap laser from the D1 or D2-transition of ^{85}Rb. If we assume, that the trap-laser with power P follows the fundamental mode TEM$_{00}$ of a Gaussian beam, then its intensity distribution is given by

$$I(\vec{r}) = I(r, z) = \frac{2P}{\pi w^2(z)} e^{\frac{-2\,r^2}{w(z)^2}}\,. \tag{1.26}$$

Here we changed to cylindrical coordinates where z describes to propagation direction of the laser beam and r the radial coordinate. Furthermore, $w(z)$ describes the beam radius, where the intensity has fallen to the $1/e^2$ value of its on axis intensity. It is given by

$$w^2(z) = w_0\sqrt{1 + \left(\frac{z}{z_R}\right)^2}, \tag{1.27}$$

were w_0 represents the minimal waist of the Gaussian beam at $z = 0$. The Rayleigh length z_R for the trap laser at wavelength λ is defined as

$$z_R = \frac{\pi w_0^2}{\lambda}. \tag{1.28}$$

The energy of the atom in a dipole trap is typically much smaller then the potential depth $U(r = 0, z = 0)$ in the center of the trap. Therefore, we can assume that the movement of the atom will be small compared to the beam waist and Rayleigh length. Thus, we can approximate the dipole potential as a harmonic oscillator potential:

$$U(r, z) \approx -U_0\left(1 - 2\left(\frac{r}{w_0}\right)^2 - \left(\frac{z}{z_R}\right)^2\right). \tag{1.29}$$

Here $U_0 = U(r = 0, z = 0)$ is the maximum trap depth which is given by Eq. (1.25) as

$$U_0 = \frac{c^2\Gamma}{\omega_0^3 w_0^2}\left(\frac{2}{\delta_{D2}} + \frac{1}{\delta_{D1}}\right) P. \tag{1.30}$$

In this potential the trapped atom should oscillate at the frequencies ν_r in radial and ν_z in axial direction. For our potentially desired parameters of a trap focus waist of 1 µm and a trap power P of 0.5 mW which leads to a trap depth $U_0 = k_b \cdot 1\,\text{mK}$, we can calculate the frequencies as:

$$\nu_r = \sqrt{\frac{4U_0}{mw_0^2}} \cot \frac{1}{2\pi} = 95.1\,\mathrm{kHz} \tag{1.31}$$

$$\nu_z = \sqrt{\frac{2U_0}{mz_R^2}} \cdot \frac{1}{2\pi} = 16.8\,\mathrm{kHz}. \tag{1.32}$$

For our experiment, we have to make sure that only one atom is trapped inside the dipole trap at any given time. This can be realized by using the collisional blockade mechanism. By reducing the size of the waist of the focused Gaussian beam to a few micrometer, we can minimize the trap volume. If two atoms enter the trap in such a configuration, they will kicked out of the trapping volume as collisions are the dominant loss mechanism [21] [22]. In the following section, we will describe how such dipole trap can be experimentally realized in our setup.

1.2 Optical Setup

The centerpiece of the optical setup is a confocal microscope depicted in Fig. 1.2. The key elements of the confocal microscope are two beams which are the dipole trap and the mode that is used for collecting the atomic fluorescence of the D2-transition. The mode of each beam is defined by two aspheric lenses where the first lens with focal length f_{col} collimates the divergent beam from a single mode fiber. The second lens with focal length f_{obj} offers a high numerical aperature (NA) and focuses the beam down to a focus spot size w_0 of a few micrometer which allows the collisional blockade regime to be reached. The waist size at the trap position is given approximately [23] by

$$w_0 \approx w_{0,f} \frac{f_{obj}}{f_{col}} = 2.65\mu m \, \frac{f_{obj}}{f_{col}} \, . \tag{1.33}$$

Here $w_{0,f}$ is the waist radius of a Gaussian beam in the fiber given by the manufacturer as 2.65 µm ± 0.5 µm [24]. When choosing the lenses of this setup, we have to study the interplay between diffraction and aberration introduced from the optical components on the focus spot size and on the intensity distribution at the focus. This will be done in chapter 2, where we will characterize the beam and focus quality of the confocal microscope.

The actual dipole trap is a diode laser at 784.6 nm red detuned by 4.6 nm from the 780 nm D2-line. It is generated by a volume-holographic-grating stabilized diode laser from Thorlabs. Afterwards the trap is coupled into a polarization maintaining single mode fiber and delivered to the optical setup. In order to collect the florescence light, a second beam path has to be added. A Semrock MaxLine filter (LL01-785 FWHM 3.0 nm) is used in the setup to separate both beams. At depicted in Fig. 1.2 the dipole trap gets reflected by the filter while the florescence light is able to pass. In order to align the fluorescence collection arm, we shine in a second laser in reverse direction into the collection path. It is generated by a external cavity diode laser (ECDL) from Toptica Photonics which is stabilized to the D2-transition of Rubidium. The foci of both beams at the trap position can be aligned to each other by overlapping their focal spots on a microscope after a part of the main beam is reflected by a transmissive mirror and focused down by the same objective lens as in the vacuum chamber. This alignment arm can be seen on the left of Fig. 1.2. The positions of the focus spot can be independently adjusted by using two mirrors directly after the collimation leans of each laser beam. The alignment microscope itself consists of a Mitutoyo infinity corrected objective with a magnification factor of 20. Behind the objective the beam foci are imaged onto a charge-coupled device (CCD) camera. In chapter 3, we will demonstrate the trapping of single atoms and determine the life time of the trapped atoms with a similar setup as depicted in Fig. 1.2.

The goal of the experiment is to investigate the interaction of a single atom in the strong coupling regime of cavity quantum electrodynamics. In order to reach the strong coupling regime, we have to bring the trapped atom into the evanescent field close to the surface of our WGM mircoresonator. Consequently, we will put one of such resonators into the vacuum chamber. Furthermore, we will use two tapered fibers inside the vacuum chamber to couple light into and out of the WGM microresonator. In order to fit the six MOT-beams around the resonator and the two fibers inside the vacuum chamber, the MOT is set up such that its center is about 1 mm away from the surface of the resonator. Consequently, we need a method to transport the single ^{85}Rb atoms from the MOT-position to the surface of the resonator. Our approach is to load the atom from the MOT into our dipole trap and move the dipole trap itself by shifting the focus position of the dipole trap laser from the MOT to the surface of the WGM microresonator. As depicted with dimmed elements in Fig. 1.2, we insert an electrically tunable lens (ETL) from Optotune into the beam path before the focusing objective lens. By changing the supply current to the lens we are able to change the curvature and therefore the focal length of the lens. In Chapter 4 we will investigate the feasibility of using the ETL for atom transport inside the dipole trap.

When the focus of the confocal microscope reaches the resonator's surface, a partial standing wave pattern in front of the resonator will be generated due to the interference of the incoming and retroreflected beam. Because the standing wave trapping potential offers multiple potential minima at positions $(n \cdot \lambda/2) + \lambda/4$ from the resonator's surface, the atoms can not be deterministically transported into the trapping side closest to the resonator. This is problematic, as to reach the strong coupling regime, the atom has to be transported into the trapping site closest to the resonator's surface. To overcome the standing wave problem, we plan to generate a trapping field composed of a superposition of higher-order Laguerre-Gaussian modes. As proposed by [25], an interference of such modes at the focus of the dipole trap would suppress higher trapping minima as we will describe in chapter 4. The modes themselves are generated by using a phase-only spatial light modulator (SLM), which will be put into the path of the dipole trap beam as depicted with the dimmed elements in Fig. 1.2. One major technical challenge is to make sure that the proposed superposition of higher-order Laquerre-Gaussian modes which we use in the experiment really generates the desired standing wave patter. For this we need to investigate the standing wave pattern close to the resonator's surface. Therefore, we developed a new method based on a Erbium-doped optical nanofiber to characterize the potential. A proof of concept for this method is showcased in chapter 4, where we were able to measure a standing wave pattern of a tightly focused beam close to the surface of a gold-plated mirror.

Furthermore the dimmed parts of 1.2 show also three additional beam paths that will be implemented in a future version of the experiment. The first one on the right hand side is a second dipole trap beam slightly red detuned to the $5^2S_{1/2} \rightarrow 6^2P_{3/2}$ transition

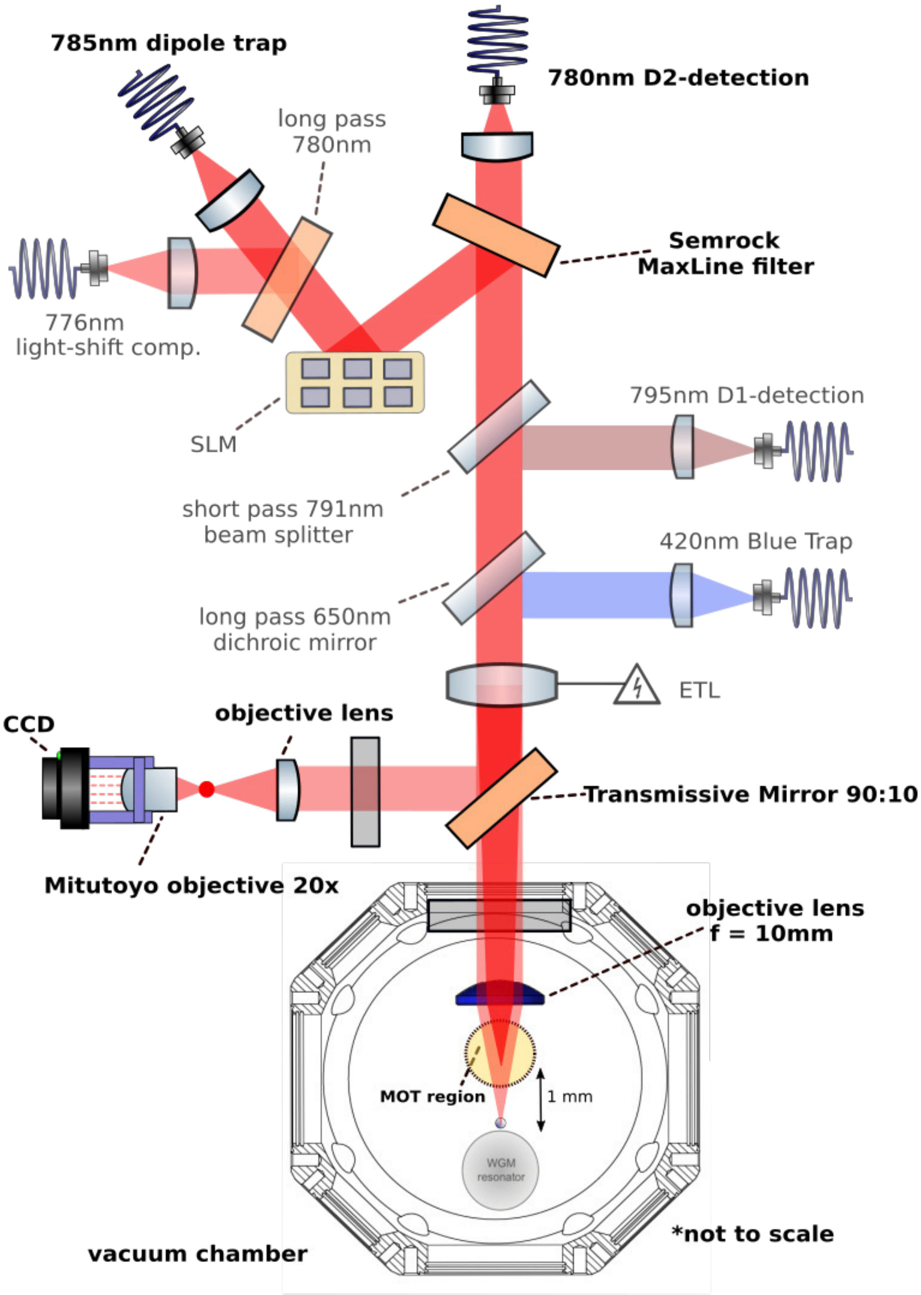
785nm dipole trap
780nm D2-detection
long pass
780nm
Semrock
MaxLine filter
776nm
light-shift comp.
SLM
795nm D1-detection
short pass 791nm
beam splitter
420nm Blue Trap
long pass 650nm
dichroic mirror
ETL
CCD
objective lens
Transmissive Mirror 90:10
Mitutoyo objective 20x
objective lens
f = 10mm
MOT region
1 mm
WGM
resonator
*not to scale
vacuum chamber

Figure 1.2: Optical setup: **(bright)** A confocal microscope generates a tight focus spot inside the MOT-region to trap single ^{85}Rb atoms. The fluorescence of the atoms at the D2-line is collected through the same objective and separated from the trap light via a Semrock MaxLine filter. The overlap of both beams can be aligned by using the microscope setup at the right side. **(dimmed)** Additional lasers and optics required to realize trapping, detection and atom transport into the resonator's WGM that will be implemented in the future: The atom transport is realized by changing the focus of an electric tunable lens (ETL). A spatial light modulator (SLM) generates higher-order Laguerre-Gaussian modes on the trapping beam.

at 420 nm. This ‘blue’ dipole trap will be ramped on, when the atom is already at the location of the desired trap site in the ‘red‘ dipole trap. Because the wavelength of this ‘blue’ dipole trap is almost half of the wavelength of the ‘red’ dipole trap, we are able to trap the atoms closer to the resonator in the potential minima at $\lambda/4 \approx 100\,\text{nm}$ away from the surface. The ‘blue’ trap is generated by a ECDL DL-Pro from Toptica Photonics and combined with the main beam path by using a long pass at 650 nm from Thorlabs (TL-DMLP650). The second additional beam path is used to collect the fluorescence at the D1-line of ^{85}Rb at 795 nm. By using a short pass at 791 nm from Semrock (FF791-SDI01) we are able to separate the fluorescence of the D1 line from the main beam path. An additional beam path is used to shine in a ‘light shift compensation laser’ at 776 nm. The need for this additional laser stems from the fact that the highly focused trapping light introduces a large position-dependent light shift to the $^5S_{1/2}$ and the $^5P_{3/2}$ energy level of ^{85}Rb which can be compensates by this beam [11]. The light shift compensation beam is combined with the trap laser before the SLM because the light shift compensation laser needs to have the same intensity distribution in the focus spot as the trapping laser. The beams are combined by using a long pass filter from Semrock (LP02-780RU) at 780 nm. The alignment of all the different laser beams can be realized via the microscope setup in the alignment arm. All beam paths offer two steering mirrors and polarization control with a $\lambda/2$ wave plate. For the sake of clarity, these optical elements are not depicted in the schematic of Fig. 1.2.

As it is shown in Fig. 1.3, all optical elements are integrated into a cage system for three reasons. First, the ETL has to mounted vertically in order to minimize the aberrations by the wave front error introduced by the liquid focus tunable lens [26]. The mounting can be realized within the cage system to be compact and stable. Second, as it is shown in Fig., 1.3 the optical setup will be placed directly in front of the vacuum system on a translation stage. In order to fit the whole setup at this position, we design a compact setup by using the cage system. Third, in order to realize the planned trapping, detecting and transporting procedure we have to precisely overlap the different focal spot on the microscope of the alignment arm. After this is done, the cage system should stabilize the whole setup in order to perform experiments more easily.

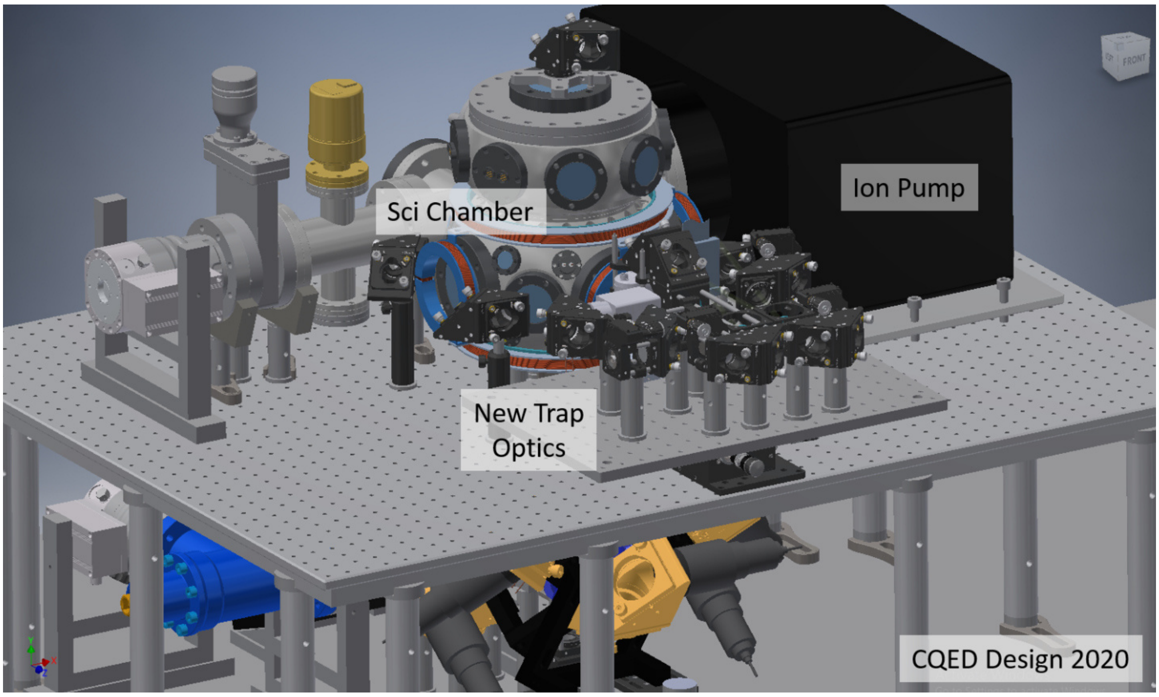
Sci Chamber
Ion Pump
New Trap Optics
CQED Design 2020
FRONT

Figure 1.3: CAD design of the optical setup placed in front of the vacuum chamber: The usage of a cage system allows for a compact and stable setup as well as for a vertical mounting of the ETL.

2

Focus Spot Characterization

As explained in the previous chapter, an in vacuum objective lens is used to focus down the dipole trap as well as to collect the fluorescence at the D2 and D1 transitions of the single trapped ^{85}Rb-Atom. For the optical systems, this means that the waist of the focus spot has to be small enough to reach the collisional blockade regime while also ensuring a maximal overlap between the mode of the fluorescence collection beam and the dipole emission pattern of the atom. In order to realize a small beam waist, we have to use a high-numerical aperture focusing objective lens. The numerical temperature (NA) of a lens is defined as the product of the refractive index of the medium and the sine of the angle θ at which light can exit the lens:

$$\mathrm{NA} = n \sin(\theta) \approx \frac{D}{2 f_{obj}}. \tag{2.1}$$

For the second part of the formula, we used the refractive index of air ($n \approx 1$) and approximated the small focusing angle as the quotient of the lens aperture diameter D and f_{obj}, the focal length of the objective lens. With the NA of the lens we can express the minimum spot size of a Gaussian beam as [27]

$$w_0 = \frac{\lambda}{\pi \mathrm{NA}} = \frac{2\lambda f_{obj}}{\pi D}, \tag{2.2}$$

where λ is the wavelength of the laser. Due to the design of our vacuum chamber and its lens holder, we have to use a focusing or objective lens with a lens aperture diameter of about 12.5 mm and a focal length of 10.0 mm. We investigated the Thorlabs AL1210 CNC-polished asphere as well as the Asphericon AHL12-10-P-U-780 asphere, because they offer the required lens diameter and focal length. Both lenses offer an effective NA for focusing of approximately 0.5 as the clear aperture diameter is around 10.0 mm. Therefore, a theoretical minimum focus waist is 0.45 µm. In reality though, this value is not reachable as for large beam radii diffraction effects and aberrations will lead to a widening of the waist and a non-Gaussian intensity distribution in the focus.

Both effects are dependent on the size of the incident collimating beam because the diffraction is caused by the truncation of the beam on the lens aperture and the aberrations are caused by a non-perfect aspheric surface profile of the lens. Also, the incident collimated beam size determines the theoretical waist, when the incident collimated beam size is smaller than the lens optical aperture diameter of 10.0 mm. The collimated beam size can be expressed similar to Eq.(2.2) as

$$d = \frac{2\lambda f_{col}}{\pi w_{0,f}}, \tag{2.3}$$

where d is the collimated beam diameter and $w_{0,f}$ the waist of the Gaussian-mode in the single-mode fiber from which an aspheric lens with focal length f_{col} is collimating the beam. When using a collimated Gaussian laser beam, the lens aperture diameter D in Eq.(2.2) is the $1/e^2$ collimated beam diameter d. Therefore we can plug Eq.(2.3) into Eq.(2.2) and get the already introduced Eq.(1.33):

$$w_0 = w_{0,f}\frac{f_{obf}}{f_{col}} \approx 2.65\mu m\,\frac{f_{obf}}{f_{col}}. \tag{2.4}$$

The waist of the Gaussian-mode in the single-mode fiber $w_{0,f}$ is given by the data sheet of our fiber as the mode field radius of 2.65 µm ± 0.5 µm [24].

At first, we planned to use lenses of the precision aspheres family from TECHSPEC and Edmund Optics. As the collimated beam was inspected with a shearing interferometer, we noticed the introduction of large wavefront errors into the beam by those lenses. This led to a non-Gaussian and asymmetric intensity distribution of the collimated beam, which was visible by putting an infrared view card into the beam path. Therefore, we are now using diffraction-limited CNC-polished aspheres with a magnetorheological finish from Thorlabs. When using these lenses for collimating, we do not observe the introduction of wavefront errors at the shearing interferometer. In the following characterizations, we used the Thorlabs AL1225H-B with a focal length of 25 mm and the Thorlabs AL2550H-B with a focal length of 50 mm.

In this chapter, we will discuss three techniques which were used to characterize the focus spot region when using the aforementioned objective and collimating lenses. First, we discuss the results of a scan through the focus spot by a knife edge while monitoring the power of the laser beam on a photo diode. Secondly we evaluate the image of the focus spot obtained by a microscope with a 20 times magnification. Finally we present a newly developed method, where a 300 nm diameter optical nanofiber (ONF) was scanned through the focus region and the photons scattered into the guided mode of the ONF are detected with single photon counting modules (SPCM). These three methods will be compared regarding the question of the quality of the focus spot and will allows us to optimize the trapping of single ^{85}Rb-Atoms as well as collection of the fluorescence.

2.1 Knife Edge Method

In the knife edge technique we use a knife edge or razor blade glued onto a large active area photo diode (Thorlabs FDS1010). We are using a Wilkinson Classic Sword double edge razor blade, whose edge we imaged in a scanning electron microscope (SEM). As shown in Fig. 2.1 (a) and Fig. 2.1 (b), this standard retail Wilkinson razor blade has a low surface roughness of 160 nm, a thin knife edge with a thickness under 100 nm and a small opening angle of approximately 40°. Therefore the chosen razor blade offers good properties for probing a tightly focused laser beam with a waist of a few micrometer.

The photo diode with the razor blade is mounted onto a translation stage, such that it's position can be controlled with sub-micron precision by stepper motors (Physik Instrumente M237.1 Stepper Motor and C-683 Mercury Controller) into two directions or axes. In the following, the axis parallel to the incident laser beam will be called z-axis and the axis perpendicular to the incident beam will be called x-axis. The general setup of a knife edge scan is shown in Fig. 2.2. In this test confocal microscope setup we employ the same collimating and objective lens and vacuum viewport as in the main atom-tapping setup. While scanning the razor blade through the focus spot, the generated photo-current is measured with an analog card from National Instruments. The whole measurement is automated by a python script that controls the data acquisition and the positioning of the stepper motors.

For each fixed z-position the razor blade moves along the x-axes vertically through the beam. Fig. 2.3 shows a typical measurement. In order to determine the beam radius $w(z)$ on each z-position, we fit the following error function to the acquired data:

$$\mathrm{Erfc}\,(x) = \int_x^\infty \frac{2P}{\pi * w(z)^2}\, e^{\frac{-2\,(x-x_o)^2}{w(z)^2}}\; dx, \tag{2.5}$$

where the Power P, the optical axis position in x-direction x_0 an the beam radius $w(z)$ are the fitting parameters.

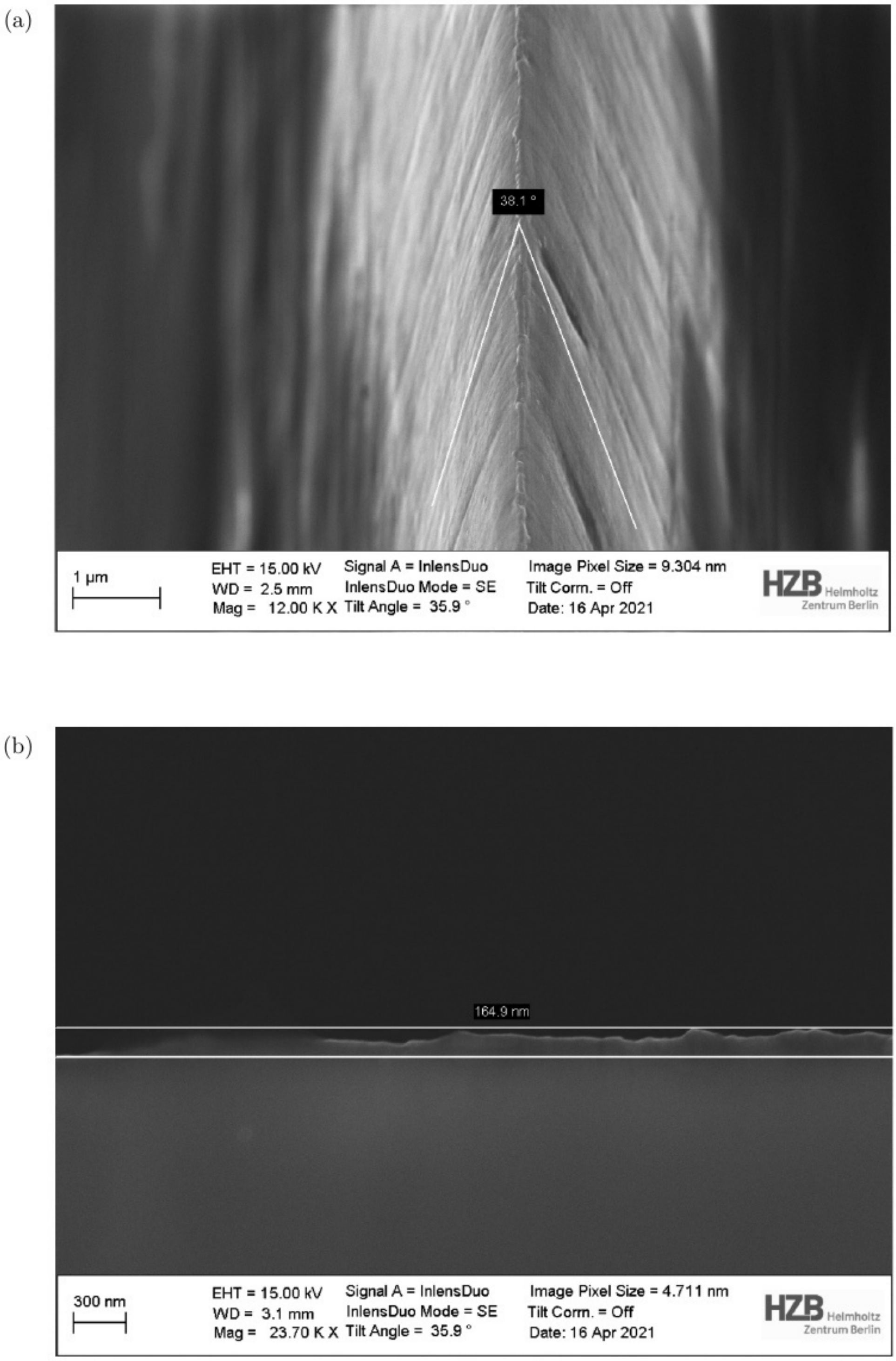
(a)
38.1 °
1 µm
EHT = 15.00 kV
WD = 2.5 mm
Mag = 12.00 K X
Signal A = InlensDuo
InlensDuo Mode = SE
Tilt Angle = 35.9 °
Image Pixel Size = 9.304 nm
Tilt Corrn. = Off
Date: 16 Apr 2021
HZB Helmholtz Zentrum Berlin
(b)
164.9 nm
300 nm
EHT = 15.00 kV
WD = 3.1 mm
Mag = 23.70 K X
Signal A = InlensDuo
InlensDuo Mode = SE
Tilt Angle = 35.9 °
Image Pixel Size = 4.711 nm
Tilt Corrn. = Off
Date: 16 Apr 2021
HZB Helmholtz Zentrum Berlin

Figure 2.1: Electron microscope image of the Wilkinson Classic Sword double edge razor blade taken from the side (a) and from the top (b). Thanks to Katja and Aleksei for these images.

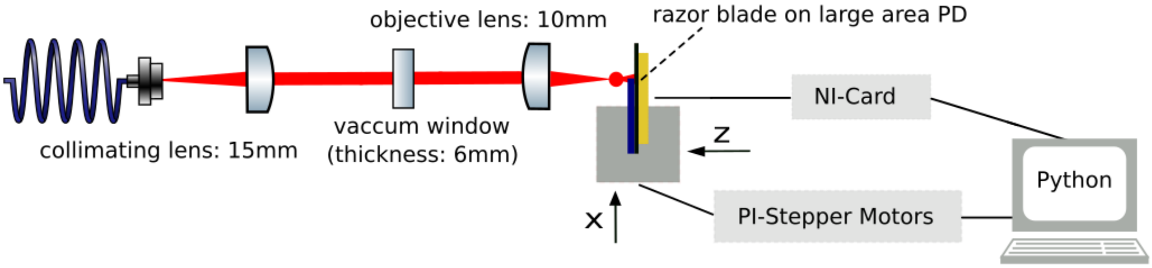
objective lens: 10mm
razor blade on large area PD
NI-Card
collimating lens: 15mm
vaccum window
(thickness: 6mm)
z
x
Python
PI-Stepper Motors

Figure 2.2: Measurement setup of the knife edge technique: A razor blade is mounted on a translation stage setup that can be moved by stepper motors in x- and z-direction. Different lenses are tested for the collimating and as the high-NA objective lens in order to evaluate the focus spot created. As the razor blade moves through the region of the focus spot, a decrease of power is detected on the large area photo diode. An error function Eq.(2.5) is fitted onto the flank in order to obtain the waist on multiple z-positions along the optical axes.

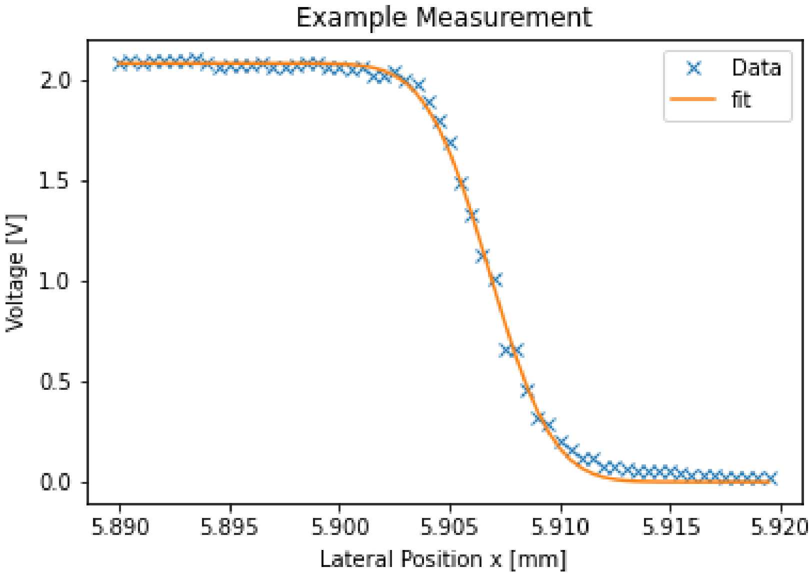

Figure 2.3: Example of a detected power vs. lateral position x as the razor blades cuts laterally through the beam near the focus spot region. The fit shown in the data is performed using Eq.(2.5).

2.1.1 Test Measurement

In order to test the measurement technique we evaluated a relatively precisely known focus spot with a comparable waist size, where we took care to minimize the aberration introduced by our optical system to not distort the known focus spot. A relatively good known quantity is the mode field radius or Gaussian mode radius of a laser beam coupled into the single mode polarization maintaining fiber (Thorlabs PM780-HP fiber). The data sheet of our fiber refers to it as 2.65 µm ± 0.5 µm [24]. Thus, we used two identical diffraction limited aspheres (Thorlabs AL2550H-B) for the collimating as well as for the focusing lens in our measurement setup depicted in Fig. 2.2, thus realizing an 1 :1 microscope. Therefore we expect a waist of around 2.65 µm from our measurement.

For the described setup, the measurement was conducted in the following manner. Around the focus within in the expected Rayleigh length of $z_0 = 28\,\mu\text{m}$, the scan was performed with a step size along the z-direction of 2.5 µm and 0.5 µm in the x-direction while in the outer region a step of 10.0 µm in the z-direction and of 2.5 µm in the x-direction was used. In Fig. 2.4, the fitted beam radius is plotted against the z-position where the data was acquired. The minimal radius fitted by Eq. 2.5 is found to be 2.4 µm ± 0.1 µm, which is well inside the error bars given by the manufacturer.

Nevertheless, in order to get a proper understanding of the ability of the optical system to focus a Gaussian laser beam to a certain spot size, we have to evaluate the whole measured Gaussian beam. Let's first recall that the beam waist at a certain longitudinal position $w(z)$ is given by:

$$w(z)^2 = w_0\sqrt{1+\left(\frac{z}{z_R}\right)^2}. \tag{2.6}$$

Here w_0 represents the minimal waist of the Gaussian beam at $z = 0$ and z_R is the Rayleigh length for a laser with wavelength λ given by

$$z_R = \frac{\pi w_0^2}{\lambda}. \tag{2.7}$$

Furthermore, we have to introduce the beam propagation factor M^2. In optical engineering this factor compares the product of the beam divergence angle Θ and the waist W_0 at the focus of a the measured beam with the same factors θ and w_0 of a theoretical Gaussian reference beam [28] as

$$M^2 = \frac{\Theta W_0}{\theta w_0}. \tag{2.8}$$

In our case, the measured divergence angle and the reference divergence angle are the same, because the divergence angle is determined by the collimated beam radius r and the focal length of the objective lens f_{obj}.

$$tan(\theta) = \frac{r}{f_{obj}}. \tag{2.9}$$

Therefore, the M^2-factor of Eq. 2.8 is reduced to

$$M^2 = \frac{W_0}{w_0} \quad \text{with} \quad \Theta = \theta. \tag{2.10}$$

In order to determine the M^2 value, we use the Gaussian beam propagation equation as described by ISO standard 11146-1 [29] and [28] in the form of:

$$W(z)^2 = W_0^2 + \Theta^2(z - z_0)^2. \tag{2.11}$$

Next, we plug into this formula the earlier defined relationships between the M^2-factor and the beam waist, as well as the divergence angle:

$$\Theta = \theta = \frac{\lambda}{\pi w_0} \quad \text{and} \quad M^2 = \frac{W_0}{w_0}. \tag{2.12}$$

For determining the M^2-beam propagation factor from measured waist radii at the $1/e^2$-level of intensity, we get the following fit formula:

$$W(z)^2 = W_0^2 \left[1 + (M^2)^2 \left(\frac{\lambda}{\pi W_0^2} \right)^2 (z - z_0)^2 \right]. \tag{2.13}$$

When performing the fit with the measured data over three Rayleigh lengths on both sides of the minimal waist we get the following values of M^2 and W_0:

$$W_0 = 2.75\mu m \pm 0.1\mu m \quad \text{and} \quad M^2 = 1.06 \pm 0.01 \tag{2.14}$$

Please note, that the given errors are just representing the fitting error of the used optimizing algorithm and not the measurement error of the whole system used for the characterization measurements. Both the raw data as well as the fitted function are depicted in Fig. 2.4. The estimated value of W_0 is 1.06 times bigger than the theoretical waist value w_0 of 2.6 µm for a Gaussian beam with the same divergence angle in the far field. Both the minimal beam waist as well as the fitted beam waist are close to the value given by manufacturer of our fiber. Also, the M^2 of 1.06 is very close to the best possible value of M_0^2 of 1.0. Furthermore, the smallest fitted waist in the curve of Fig. 2.4 is 2.47 µm ± 0.09 µm. Also, this value lies close to the value given by manufacturer within the provided errors. Therefore we can state that, our knife edge method is a reliable technique to measure the beam waist inside of the dipole trap's focus region.

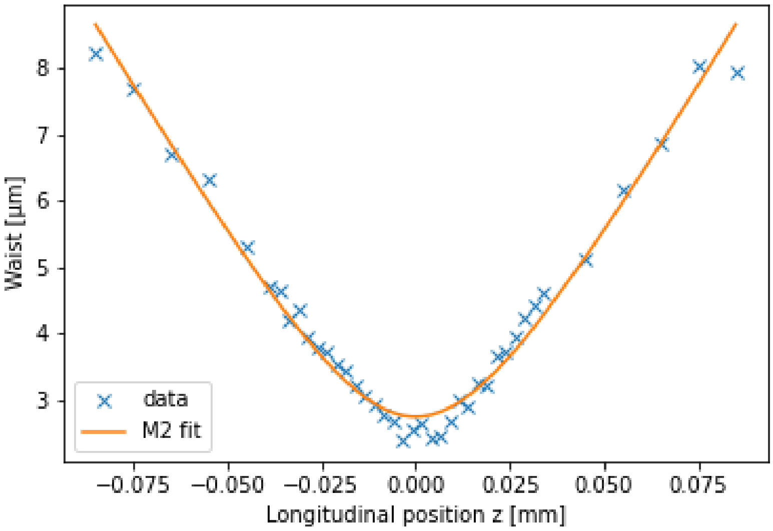

Figure 2.4: Measured waist plotted as a function of the longitudinal z-position on the optical axes for the calibration measurement with the 1 :1 microscope. The minimal measured beam waist is 2.4 µm. The fit with Eq. 2.13 gives an M^2 value of 1.06 with a beam waist radius of 2.75 µm

2.1.2 Lens Characterization Measurements

After testing our knife edge technique, we can now start to investigate the focus region for different collimation and objective lenses. All measurements were conducted with the setup described in Fig. 2.2. The evaluation of those measurements are summarized in Fig. 2.5 and in Tab. 2.1. The theoretical beam waist at the focus spot w_0 is calculated using Eq.(2.4).

Let's first compare the influence of the objective lens onto the waist size. The measurements with the Thorlabs TL-AL1210 objective lens are depicted in the plots in the upper row of Fig. 2.5 whereas the measurements with Asphericon AS-AHL12-10 as the objective lens can be seen in lower row of Fig. 2.5. Although both objective lenses offer the same focal length, the resulting waist size when using the Asphericon AS-AHL12-10 objective lens is significantly smaller as compared to the Thorlabs TL-AL1210 objective lens. The main quality difference between both lenses is the root mean square (RMS) wavefront error, which is introduced into the beam by the lens. For the Thorlabs lens the wavefront error is 0.5 µm RMS and for Asphericon lens it is 0.39 µm RMS. Even though the difference of the RMS wavefront error is just around 0.1 µm, the resulting waist is then 3 to 5 times smaller with the Asphericon lens of smaller wavefront error, due to the induced aberrations.

As we compare the collimating lenses, it is clear that also the collimated beam size (6 mm ($f = 50.0$ mm) in the left column and 3 mm ($f = 25.0$ mm)in the right column in Fig. 2.5) has of course an influence on the waist size. Theoretically, according to Eq.(2.4), the waist is inversely proportional to the beam size. As we see in Tab. 2.1.2, the measurements show an opposite result.

One explanation is that the diffraction caused by the truncation of the beam on the objective lens with an aperture diameter of 12.5 mm leads to significant broadening of the focus waist. As a larger amount of the intensity is truncated by the aperture, a more pronounced Airy-rings like intensity distribution is created. This effect is strong directly at and behind the focus spot region, as the diffraction of the beam at the round aperture leads to Airy-rings in the far field from the aperture. Measuring such intensity distribution with the knife edge technique and fitting Eq.(2.5) to the observed flank, the fitted waist becomes larger. An example of such a fit measured 50 µm behind the focus is depicted in Fig. 2.6. Furthermore, we can observe in Fig. 2.5 (a) and (b) that for the Thorlabs TL-AL1210 objective lens the M^2-fit is not correctly evaluating the waist position on the longitudinal z-axes. The lens induced aberration and diffraction is resulting in a non-Gaussian intensity distribution, which is changing the fitted waist.

A second possible explanation for the increase of the fitted M^2 waists, when using a beam with a larger collimated beam size incident to the objective lens, would be a slight misalignment of the knife edge in respect to the beam axis or a potentially non-sharp section of the razor blade edge itself. A candidate for such a reasoning is the measurement depicted in 2.5 (c), because we observe a plateau of measured beam waists close to the focus. This could indicate a insufficient resolution of the knife edge setup for this measurement due to increased surface roughness or potential misalignment of the knife edge while it is scanning non-orthogonal through the beam.

In order to develop a better understanding of the observed results, we built up a microscope to image the focus spot region in the next section.

Results of the Knife Edge Measurements				
Collimating lens	TL-AL2550H	TL-AL1225H	TL-AL2550H	TL-AL1225H
	$f = 50.0$ mm	$f = 25.0$ mm	$f = 50.0$ mm	$f = 25.0$ mm
Objective lens	Thorlabs	Thorlabs	Asphericon	Asphericon
See Fig. 2.5	(a)	(b)	(c)	(d)
Minimal Waist	(7.53 ± 0.16)μm	(7.09 ± 0.24)μm	(3.28 ± 0.15)μm	(1.62 ± 0.09)μm
M^2-Fitted Waist	(7.41 ± 0.01)μm	(7.37 ± 0.06)μm	(2.72 ± 0.22)μm	(1.80 ± 0.05)μm
M^2-factor	13.91 ± 1.49	7.13 ± 0.05	4.75 ± 0.22	1.70 ± 0.05
Theoretical Waist	0.53 μm	1.06 μm	0.53 μm	1.06 μm
Beam Radius	6 mm	3 mm	6 mm	3 mm
Objective Lens Wavefront Error	$<$ 0.5 μm RMS	$<$ 0.5 μm RMS	$<$ 0.39 μm RMS	$<$ 0.39 μm RMS

Table 2.1: Results of the Characterization of the Focused Beam using the Knife Edge Technique as depicted in figure 2.2

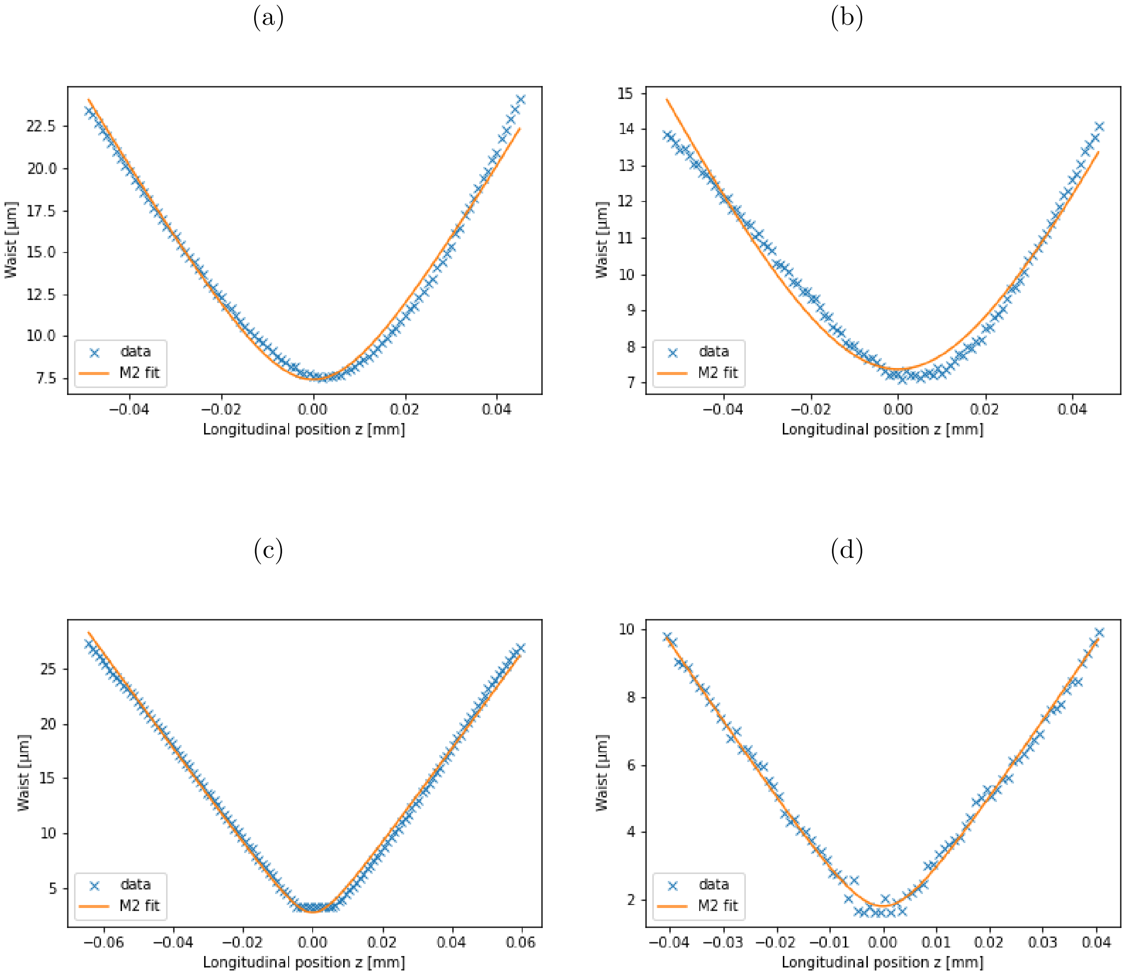

Figure 2.5: Results of knife edge measurements for different lens sets: The M^2-value was calculated according to Eq.(2.13). (a) Collimating with the $f = 50.0$ mm TL-AL1250H lens results in a 6 mm beam radius, focusing with Thorlabs TL-AL1210 objective lens leads to a fitted waist of 7.5 µm and a M^2 value of 13.7. (b) Collimating with the $f = 25.0$ mm TL-AL1225H lens results in a 3 mm beam radius, focusing with Thorlabs TL-AL1210 objective lens leads to a fitted waist of 7.4 µm and a M^2 value of 7.1. (c) Collimating with the $f = 50.0$ mm TL-AL1250H lens results in a 6 mm beam radius, focusing with Asphericon AS-AHL12 objective lens leads to a fitted waist of 3.3 µm and a M^2 value of 4.8 (d) Collimating with the $f = 25.0$ mm TL-AL1225H lens results in a 3 mm beam radius, focusing with Asphericon AS-AHL12 objective lens leads to a fitted waist of 1.7 µm and a M^2 value of 1.7.

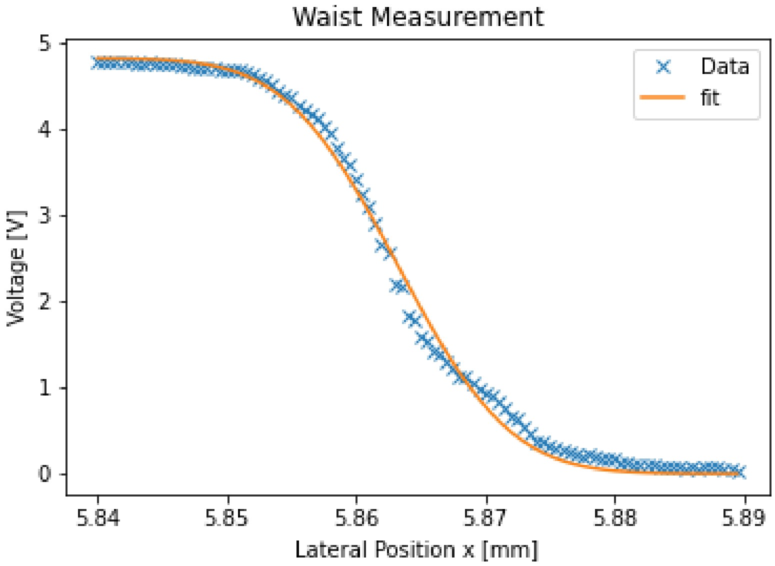

Figure 2.6: Example of the influence of diffraction on the fitted waist size measured 50 µm behind the focus using the collimating lens with a focal length of 50 mm and the Thorlabs AL1210 objective lens: The Airy-ring structure leads to a flatter detected power vs. lateral position flank and wider fitted waist.

2.2 Imaging Method

The knife edge method is not (very) sensitive to fast changes of the intensity distribution of the dipole trap, because we detect the whole transmitted power of the laser at a certain lateral x-position. In order to get an better idea of the intensity distribution at the focus, we built up a high-quality optical microscope to image the focus spot region. The microscope consists of a infinity corrected objective (20X Mitutoyo Plan Apo NIR B) with a magnification factor of 20, an NA of 0.4 and focal length of 10 mm. The same objective will also be used for the alignment of the planned dipole trap setup as described in chapter 3. The microscope setup depicted in Fig. 2.7 is designed in such a way that the objective images the focal spot region of the trap laser on a CCD-camera (mvBlueFox3-1013GE). Both are connected by a cage system, which is fixed to a translation stage driven by stepper motors (Physik Instrumente M237.1 Stepper Motor and C-683 Mercury Controller) to ensure precise movement in the z-direction (longitudinal on the optical axis) and x-direction (transversally to optical axis). We use a distance of 180 mm between the objective exit pupil and the CCD sensor. A larger distance between CCD and exit pupil would result in a mechanical more unstable setup, as the whole objective-CCD-cage system has to be moveable on the stepper motors.

2.2.1 Testing the Microscope Setup

As the laser beam is incident onto the CCD-chip, it is illuminating an array of photoactive cells. The incoming laser intensity is then translated into a gray value from 0 to 256. Each element of that array, or pixel, has a height and width of 5.3 µm. Because the magnifica-

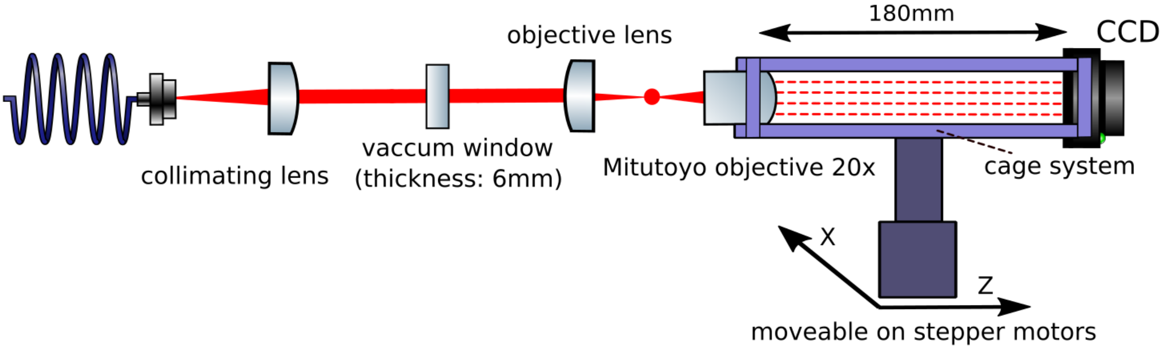

Figure 2.7: Measurement setup for the microscope imaging setup: Different lenses are used as the collimating and objective lens in order to evaluate the created focus spot. The microscope consisting of a Mitutoyo infinity corrected objective and a CCD at a distance of 180 mm is mounted onto a translation stage driven by stepper motors. The setup offers a magnification factor of 19 , when looking at the focus spot region.

tion factor of our microscope configuration can only be estimated, we first calibrate the microscope by putting a test target into the focus. The image of that test target on the CCD can be viewed in Fig. 2.8. By measuring the width of the lines of the pattern 6 / 2 in pixel, we can determine the magnification m of the optical system with the known line separation given in millimeter by the target to

$$m = 19.07. \tag{2.15}$$

In order to test the imaging capabilities of the microscope with our dipole trap and fluorescence collection optics , we investigate the focus spot waist of an already known focused beam. Similar as with the knife edge technique, we build up a 1 :1 microscope consisting of two identical diffraction limited aspheres (Thorlabs AL2550H-B) for the collimating as well as for the objective lens in Fig. 2.7. For this measurement the microscope is moved with a step size of 1 µm longitudinally through the focus spot region. On every fixed longitudinal or z-position, a picture is taken. Afterwards, we measure the local spot size by summing up all pixels in the vertical columns. The waist of the measured intensity distribution of every fixed longitudinal or z-position is determined by fitting a Gaussian to the data:

$$f(x) = \frac{2A}{\pi * w(z)^2}\, e^{\frac{-2\,(x-x_o)^2}{w(z)^2}} + B. \tag{2.16}$$

Here A, B, x_0 and $w(z)$ are the fit parameters. Afterwards, we choose the minimal fitted waist as the position of the focus spot. The fitting results are shown in Fig. 2.9.[*] From the fit and the measured magnification factor determine the minimal waist with a size of

---

[*] We also fitted a Gaussian intensity distribution to the data when all rows are summed up. Although the exact minimal waist position differs in a range of a few micrometer, the overall result of the following discussion stays the same because the intensity distribution is still rotationally symmetric. For the sake of clarity, we show just the fitting results in one lateral direction.

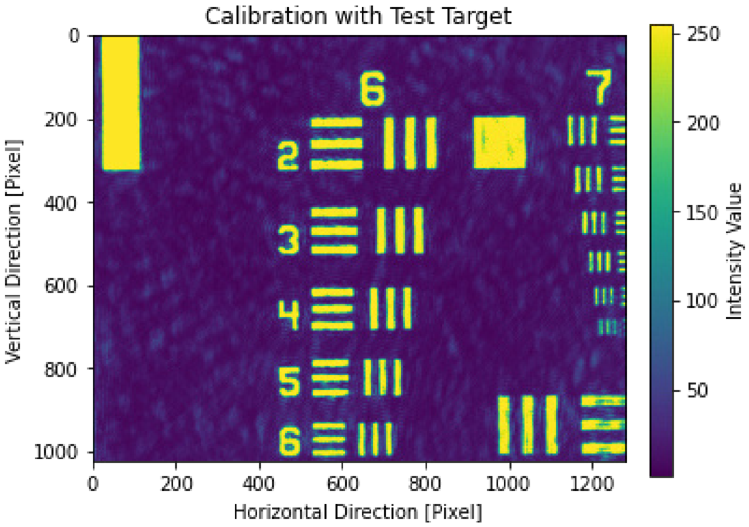

Figure 2.8: Microscope picture of the test target in order to determine the magnification factor of the setup described in figure 2.7.

$$W_0 = 10.61\,\text{pixel} \pm 0.1\,\text{pixel} \quad \text{or} \quad W_0 = 2.95\mu m \pm 0.03\mu m. \tag{2.17}$$

Comparing that value with the minimal fitted waist of 2.47 µm ± 0.09 µm from the knife edge technique when the same lenses are used, we notice a slightly higher waist value. Although the fitted minimal waist values of both characterization techniques are not within the fitting error, we see that both methods yield relatively similar values within the waist error of 0.5 µm for the 2.65 µm waist given by the manufacturer.

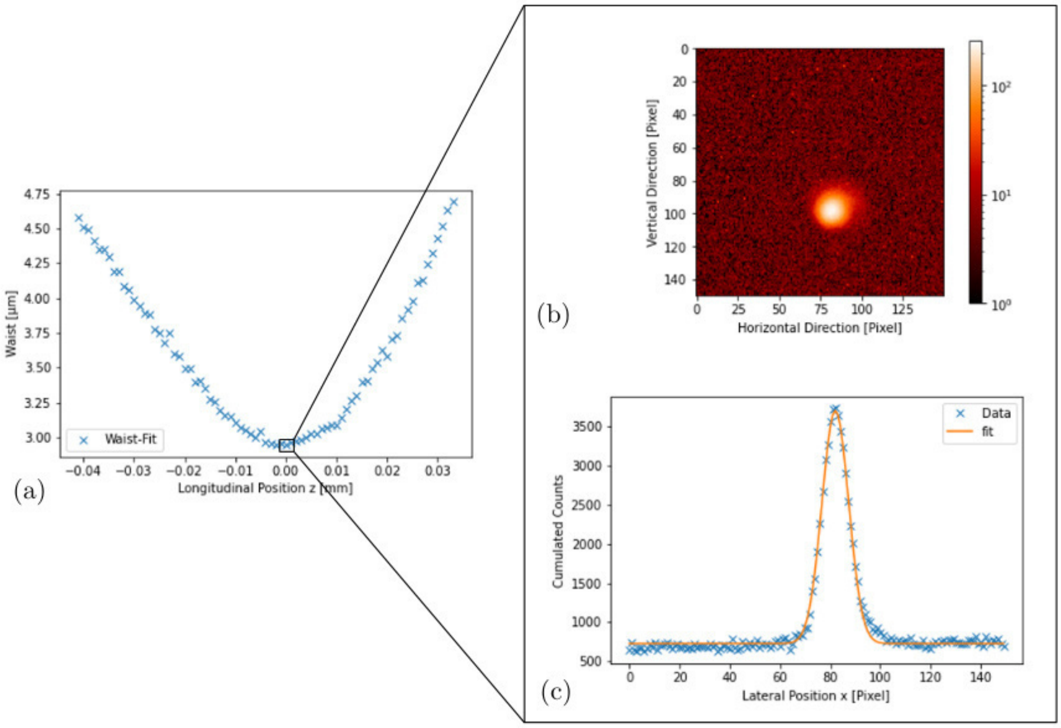

Figure 2.9: Testing the imaging method for the 1 : 1 microscope in order examine the intensity distribution at the focus spot and determine the minimum waist size: Subfigure (a) shows the fitted waist as a function of the longitudinal z-position. In (b) we depicted the the measured intensity distribution on the CCD at the position of the minimal waist on a logarithmic intensity scale. Subfigure (c) shows the corresponding Gaussian fit to the central intensity maximum with a fitted waist of (2.95 ± 0.03)µm.

2.2.2 Lens Characterization Measurements

After testing the imaging method, we now examine the intensity distribution in the focus of the dipole trap. We measure the intensity distrubution for the lens configurations which were already introduced at the beginning of the chapter. For each configuration, we take a series of pictures by moving the microscope with the stepper motors on the longitudinal z-axis through the focus spot region with a step size of 1.0 µm. Afterwards the intensity values of all columns are summed up and a Gaussian intensity distribution as described by Eq.(2.16) is fitted to the data. At the position of the minimal fitted beam radius we further examine the intensity distribution.[*] For all lens pairs the calculated minimal waist is depicted in the Tab. 2.2 for comparison. A picture of the different focus spots is showcased in Fig. 2.10 to 2.13. For all measurements. we depict in subfigure (a) the fitted waist as a function of the longitudinal z-position in order to find the minimal focus spot. Subfigure (b) always shows the measured intensity distribution on the CCD on a logarithmic intensity scale. In subfigure (c) we showcase the ingratiated intensity on one lateral axes and display the corresponding Gaussian fit for every lens set.

First let us look in more detail at the influence of the objective lens onto the intensity distribution on the focus spot. For this we compare the results of the measurement with the Thorlabs TL-AL1210 objective lens depicted in Fig. 2.10 and 2.11 with the measurement results using the Asphericon AS-AHL12-10 objective lens depicted in Fig. 2.12 and 2.13. As already discussed in the knife edge measurement, the resulting minimal waist with the Thorlabs objective lens is bigger than wth the Aspericon objective lens, due to the introduction of bigger wave front errors by the Thorlabs lens. Nevertheless, the difference of the minimal waist observed from both lenses is much smaller measured with the microscope method than for the knife-edge method. As it can be seen in Fig. 2.10 and 2.11, the intensity distribution in the focus spot obtained by the Thorlabs focusing lens is much more complex than just a simple Gaussian peak. We observe more pronounced Airy-rings as well as a kind of cloud-like structure of intensity around the focus spot. When fitting Eq. (2.16) onto the data of the microscope measurement, the fit does not

---

[*] We also fitted a Gaussian intensity distribution to the data when all rows are summed up. Although the exact minimal waist position differs in a range of a few micrometer, the overall result of the following discussion stays the same. For the sake of clarity, we show just the fitting results in one lateral direction.

Results of the Microscope Measurements				
Collimating lens	TL-AL2550H $f = 50.0\,\mathrm{mm}$	TL-AL1225H $f = 25.0\,\mathrm{mm}$	TL-AL2550H $f = 50.0\,\mathrm{mm}$	TL-AL1225H $f = 25.0\,\mathrm{mm}$
Objective lens	Thorlabs	Thorlabs	Asphericon	Asphericon
depicted in Fig.	2.11	2.10	2.13	2.12
Minimal Waist	(2.31 ± 0.09)µm	(2.47 ± 0.08)µm	(1.93 ± 0.05)µm	(1.84 ± 0.01)µm
Theoretical Waist	0.53 µm	1.06 µm	0.53 µm	1.06 µm
Beam Radius	6 mm	3 mm	6 mm	3 mm
Objective Lens Wavefront Error	$<$ 0.5 µm RMS	$<$ 0.5 µm RMS	$<$ 0.39 µm RMS	$<$ 0.39 µm RMS

Table 2.2: Results of the Characterization using the Microscope Setup

take into account the whole intensity distribution and just fits a Gaussian peak on the top of it. Therefore the fitted waist is smaller then the actual $1/e^2$ intensity level. This explains the discrepancy between both methods.

When comparing the influence of the collimating lens onto the focus spot quality, we observe that for the measurements conducted with Thorlabs TL-AL1210 the collimating lens with a focal length of 50.0 mm in Fig. 2.11 is indeed producing a slightly smaller minimal waist with (2.31 ± 0.09)µm as compared when measuring with the collimating lens with a focal length of 25.0 mm in Fig. 2.10 with a minimal waist of (2.47 ± 0.08)µm. Due to the large amount of diffraction and aberrations introduced by the objective lens, these values are far away from the theoretical minimum of 0.53 µm and 1.06 µm respectively. Furthermore, we observe in subfigure (a) in 2.10 and 2.11 of both measurements a rapid increase of the beam radius behind the focus spot as the the Gaussian is fitted to the broader Airy-ring structure. This effect is stronger when using the collimating lens with a focal length of 50.0 mm in Fig. 2.11 as the larger collimated beam radius incident on the objective lens is causing a higher amount of diffraction due to the truncation of the by beam the objective lens aperture. Comparing the results of the measurements using the Asphericon AS-AHL12-10 objective lens, we see that collimating lens with a focal length of 50.0 mm used in Fig. 2.13 is giving slightly larger minimal waist with (1.93 ± 0.05)µm as compared to the collimating lens with a focal length 25.0 mm used in Fig. 2.12 which is giving a minimal waist of (1.84 ± 0.01)µm. Nevertheless, the measured minimal waist are almost the same when considering that we also have hard to quantify measurement uncertainties for the magnification of the microscope system as well as for the precise position of the minimal spot size on the longitudinal z-position. Furthermore, we have to take into account that the numerical aperture of the objective lens with NA = 0.5 is larger than the numerical aperture of the Mitutoyo objective with NA = 0.4. Using the well known Rayleigh criterion to calculate the spatial resolution of the microscope as

$$\Delta L = \approx 1.22 \frac{f\lambda}{d} = 1.22 \frac{\lambda}{2NA} \tag{2.18}$$

resulting in $\Delta L = 1.20$ µm. Therefore, we are operating the microscope close above its spatial resolution. Consequently, we cannot exclude that the observed airy rings for the 50.0 mm collimating lens are caused by the imaging system itself. In the next section, we develop a method based on a small 300.0 nm diameter nanofiber probe in order to be able to better resolve the focus spot region.

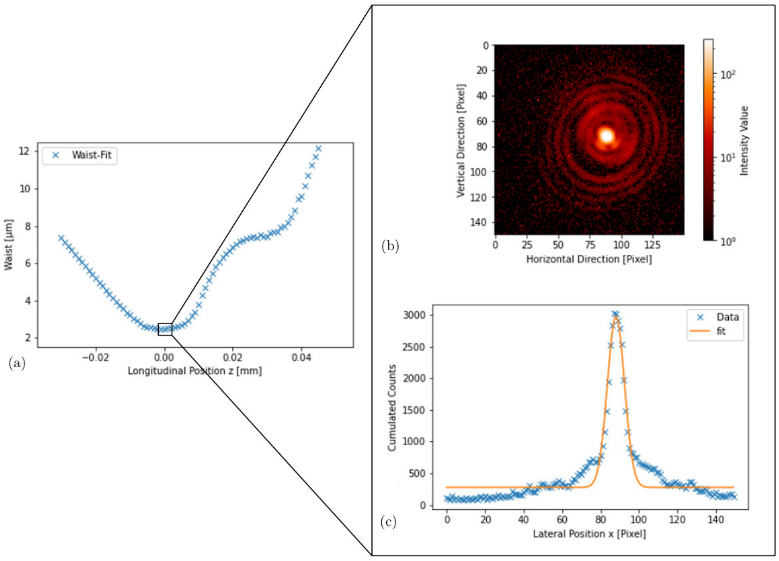

Figure 2.10: Microscope measurement for the Thorlabs TL-AL1210 objective lens with the $f = 25.0\,\mathrm{mm}$ TL-AL1225H collimation lens resulting in a collimated beam diameter of 3 mm: Subfigure (a) shows the fitted waist as a function of the longitudinal z-position. In (b) we depicted the the measured intensity distribution on the CCD at the position of the minimal waist on a logarithmic intensity scale. Subfigure (c) shows the corresponding Gaussian fit to the central intensity maximum with a fitted waist of $(2.47 \pm 0.08)\,\mu\mathrm{m}$.

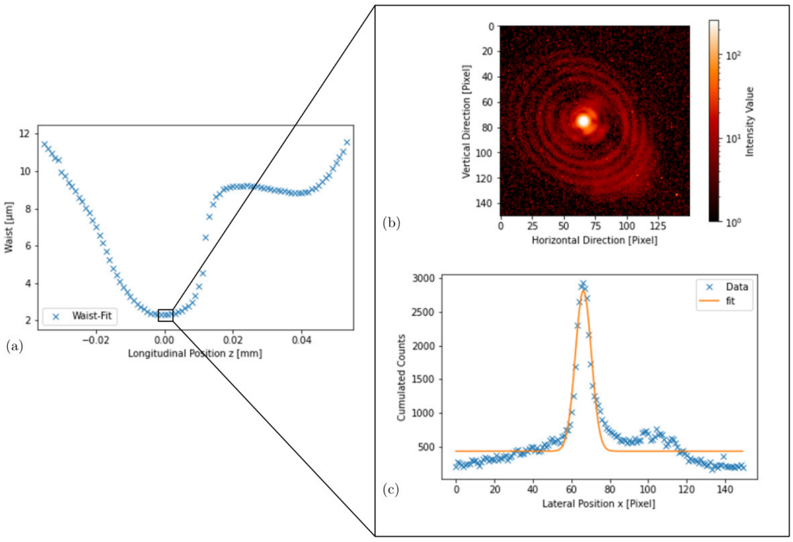

Figure 2.11: Microscope measurement for the Thorlabs TL-AL1210 objective lens with the $f = 50.0\,\mathrm{mm}$ TL-AL1250H collimation lens resulting in a collimated beam diameter of 6 mm: Subfigure (a) shows the fitted waist as a function of the longitudinal z-position. In (b) we depicted the the measured intensity distribution on the CCD at the position of the minimal waist on a logarithmic intensity scale. Subfigure (c) shows the corresponding Gaussian fit to the central intensity maximum with a fitted waist of $(2.31 \pm 0.09)\,\mu\mathrm{m}$.

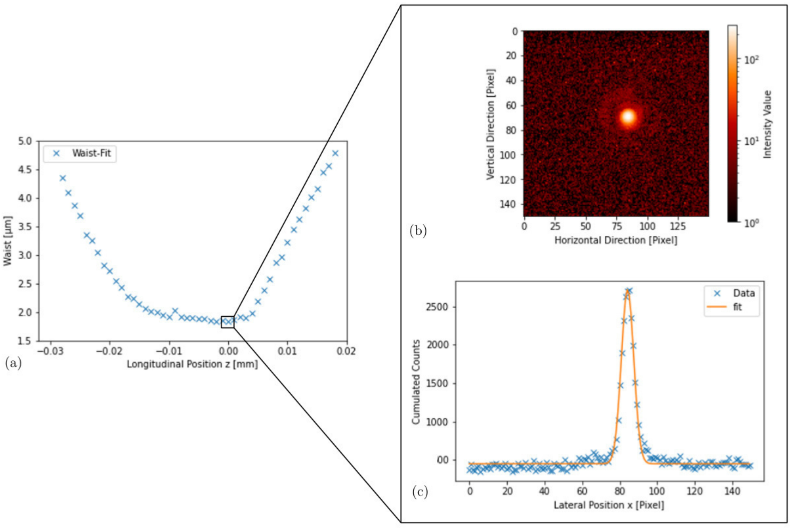

Figure 2.12: Microscope measurement for the Asphericon AS-AHL12-10 objective lens with the $f = 25.0\,\mathrm{mm}$ TL-AL1225H collimation lens resulting in a collimated beam diameter of 3 mm: Subfigure (a) shows the fitted waist as a function of the longitudinal z-position. In (b) we depicted the the measured intensity distribution on the CCD at the position of the minimal waist on a logarithmic intensity scale. Subfigure (c) shows the corresponding Gaussian fit to the central intensity maximum with a fitted waist of $(1.93 \pm 0.05)\,\mu\mathrm{m}$.

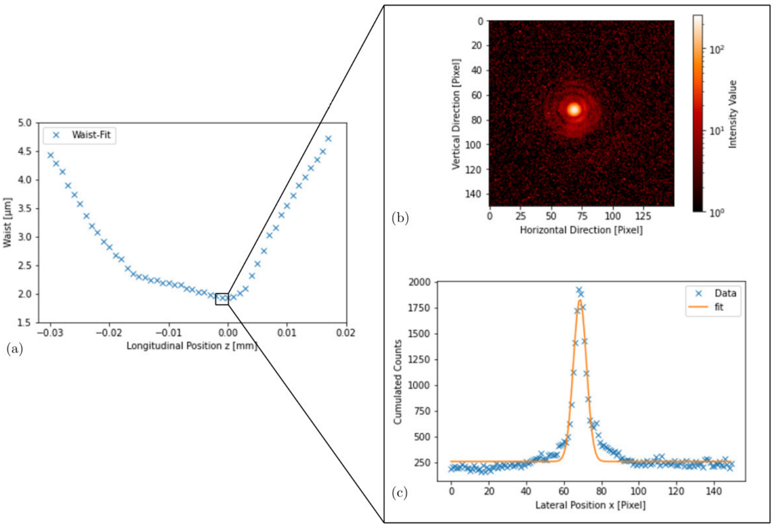

Figure 2.13: Microscope measurement for the Asphericon AS-AHL12-10 objective lens with the $f = 50.0\,\mathrm{mm}$ TL-AL1250H collimation lens resulting in a collimated beam diameter of 6 mm: Subfigure (a) shows the fitted waist as a function of the longitudinal z-position. In (b) we depicted the the measured intensity distribution on the CCD at the position of the minimal waist on a logarithmic intensity scale. Subfigure (c) shows the corresponding Gaussian fit to the central intensity maximum with a fitted waist of $(1.84 \pm 0.01)\,\mu\mathrm{m}$.

2.3 Scanning Nanofiber Method

In order to back up the results obtained by the knife edge technique and the imaging method with the microscope for the Aspericon lens, we developed a novel characterization method based (naturally in our group) on a thin optical nanofiber. Furthermore, as we will explain in chapter 4, this method can also be used to characterize the standing wave trapping potential in front of the WGM microresonator. The idea is to scan a very thin optical nanofiber (ONF) through the region of the focused beam. During the scan we collect the photons scattered into to guided mode of the ONF and detect them with single photon counter modules (SPCM). This technique should allow for an increased spatial resolution as compared to the microscope and knife edge method because the light is collected using a very thin $d = 300\,\mathrm{nm}$ diameter nanofiber probe. For this, the fiber is mounted onto a two axes translation stage moved by the same stepper motors as used in the knife edge technique. The electronic pules generated by the photons incident on the SPCM are counted with a counter module from National Instruments. Again the scan is automated and controlled with a python script. The whole setup is placed into a laminar flow box to prevent the ONF from degrading from dust in the room.[*] In Fig. 2.14 an overview of the setup is depicted. The ONF itself is produced in-house using a heat and pull process on a single mode fiber for 780 nm as the nanofiber with a diameter of 400 nm has to be much smaller than the expected beam waist of 1 µm to 2 µm. The detected photon counts in the SPCMs are then proportional to the integrated intensity along the nanofibers axes.

2.3.1 Bare Nanofiber

The first experimental realization of the method is using a ONF with a diameter of 400 nm. As shown on the left hand side in Fig. 2.16 for a fixed z-position, a signal of the scattered photons can be obtained when scanning the ONF through the focused beam. However, most of the scans give a signal comparable to the one depicted on the left hand side in Fig. 2.15, such that not even a clear peak in photon counts can be identified. Furthermore, a signal with such high spatial frequencies was not observed with the other two measurement methods. The fundamental reason for that result is, that the light scattered into the fiber is coherent. Therefore any surface imperfection like scratches are scattering light into the fiber. The scattered light can then interfere with each other resulting in a very complicated detected signal. Also possible dust particles act as strong scatterers and can contribute to the interference of coherent light.

As an alternative way to find out the position of the maximum intensity, an absorption measurement was added to the setup as shown by the dimmed components of Fig. 2.14. The idea is to detect a decrease in the photon count rate, when the fiber is directly in the intensity maximum of the focused laser beam. The detected photon rate decrease is not just a ‘shadow’, but the photons are either scattered into the fiber, reflected from the fibers surface or refracted out of of the beam such that they do not couple anymore to the multimode fiber. The results of this measurement can be seen on the right hand side of Fig. 2.16 and Fig. 2.15. Although a clear peak of the intensity maximum can now be determined at 16.025 mm in Fig. 2.16 and Fig. 2.15, it is difficult to obtain a correct waist

---

[*] Note that during the actual measurement the flow box is switched off to prevent oscillations of the ONF.

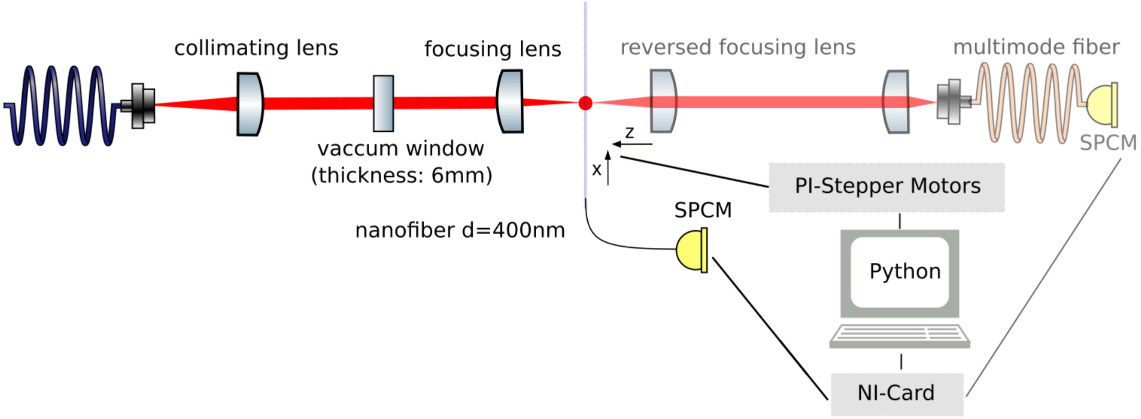
collimating lens
focusing lens
reversed focusing lens
multimode fiber
SPCM
vaccum window
(thickness: 6mm)
z
x
PI-Stepper Motors
SPCM
nanofiber d=400nm
Python
NI-Card

Figure 2.14: Setup for scanning optical nanofibers through the focus spot region: Confocal microscope using the Asphericon objective lens. **(bright)** The nanofibers are mounted onto stepper motors to enable micrometer precision movement. Into the guiding mode of the ONF scattered photons are detected by SPCMs as the fiber is scanned across the focus spot region. **(dimmed)** The focused beam is recolimated by using the same objective lens behind the focus. The beam is coupled into a multi-mode fiber in order to detect a decrease of signal at the SPCM as the fiber is moving through the focus.

W_0 of the focused laser beam. Because the dip reflects the result of multiple processes like light scattering into the fiber, reflection as well as refraction of light out of the coupled beam, we do not have a theoretical model to fit a curve to the measured data. Furthermore, the signal to noise ratio close to the focus is already relatively low as the detected decrease at the central peak is just about 10% of the overall detected counts. Therefore, seeing possible features of the intensity distribution as Airy-rings would be difficult.

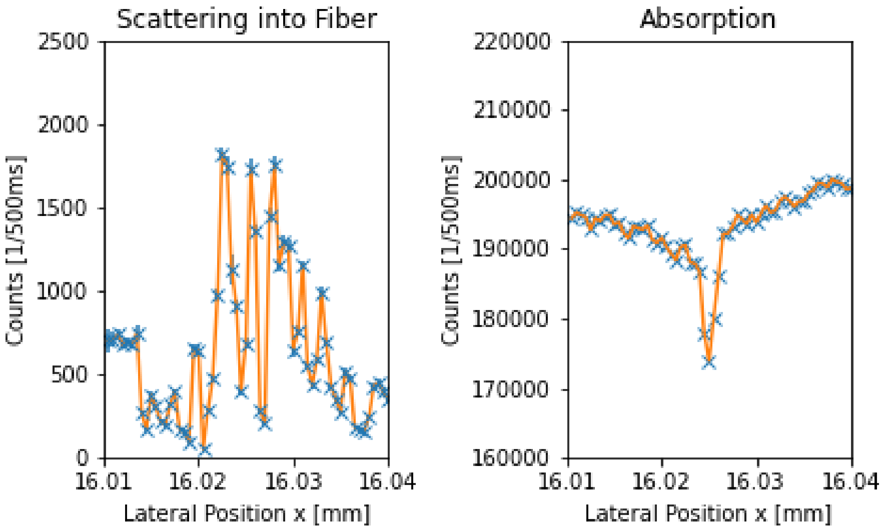

Figure 2.15: Example result for most of the scanning nanofiber measurement at one fixed z-position (left) Most of the measurements show a huge noise on the signal with a high spatial frequency of the photon scattered into the ONF. (right) Measurement of the signal passing to the multi mode fiber (dimmed in Fig. 2.14). A decrease of photon count rate can be recorded such that the position of the peak intensity can be identified.

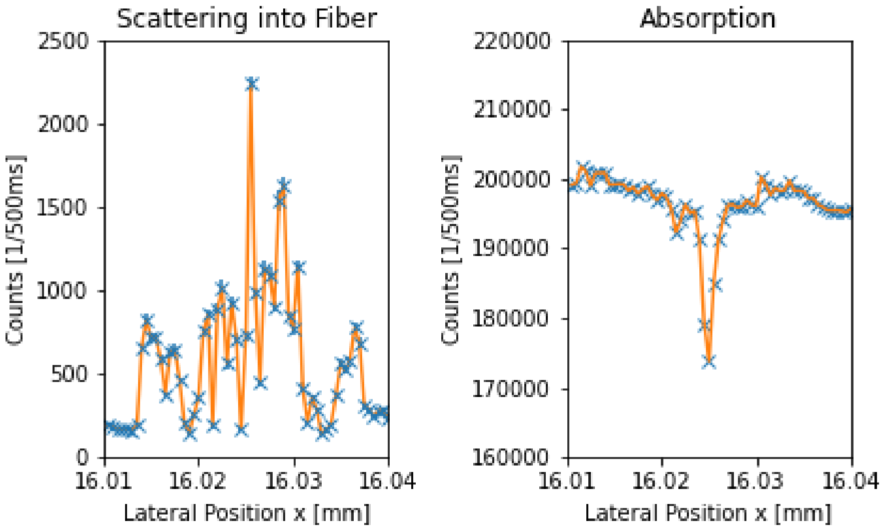

Figure 2.16: Example result of a more clear measured signal while scanning through the focus at one fixed z-position: (left) Here, the signal from the detected photons scattered into the ONF allows for the identification of a clear peak. (right) Measurement of the signal passing to the multi mode fiber (dimmed in Fig. 2.14). A decrease of photon count rate can be recorded such that the position of the peak intensity can be identified.

2.3.2 Erbium-Doped Nanofiber

In order to circumvent the interference process of coherent scattered light into nanofiber, we use incoherent scattered light from an Erbium-doped optical fiber as the signal. In such a core-Erbium-doped optical fiber, a two-photon upconversion process can be used to generate photons at a wavelength of around 540 nm when pumped with the laser at 785 nm.[30] This mechanism allows us to generate a signal with much greater signal-to-noise ratio because only the photons which interact with the erbium inside the core of the fiber contribute to the signal generated by the two-photon upconversion process. The generated light at a wavelength of around 540 nm is incoherent. Therefore no interference effects occur. Using a short pass filter at 700 nm (Thorlabs FESH0700) removes photons at the pump wavelength and therefore also filters out the coherent scattered light by surface imperfections like scratches and dust particles on the fiber's surface.

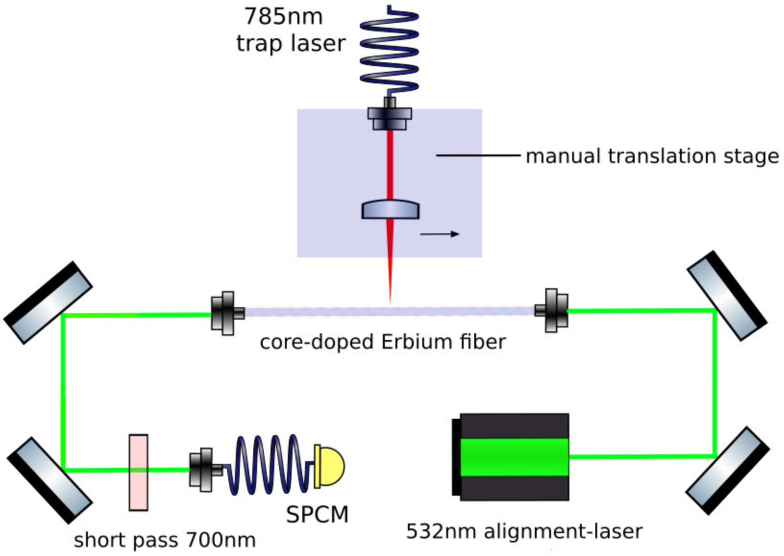

Figure 2.17: Setup for measuring the re-absorption of incoherent scattered light at 540 nm by the Erbium-doped fiber core: The pump laser is focused onto the Erbium-doped fiber and moved manually perpendicular to the fiber axes. A short pass filter is used to filter residual pumping light. The setup can be aligned by coupling a 532 nm laser via the Erbium-doped fiber into the detection system.

2.3.3 Experimental Challenges

Nevertheless, this new method for characterizing the focus spot offers two main experimental challenges. At first, the generated signal at at around 540 nm is reabsorbed by the Erbium when guided through the core of the fiber to the detector, because the generated light is resonant to the same transition out of which it was created before. As depicted in Fig. 2.17, the reabsorption is measured by counting the upconverted photons while hitting the fiber perpendicular to its surface on different positions with a pump laser at 785 nm.* As visualized in Fig. 2.18, the measured signal decreases over 5 cm by approximately 15%. Hence it is important to keep the distance between signal generation and outcoupling of the Erbium-doped fiber as short as possible to be able to observe a strong enough signal.

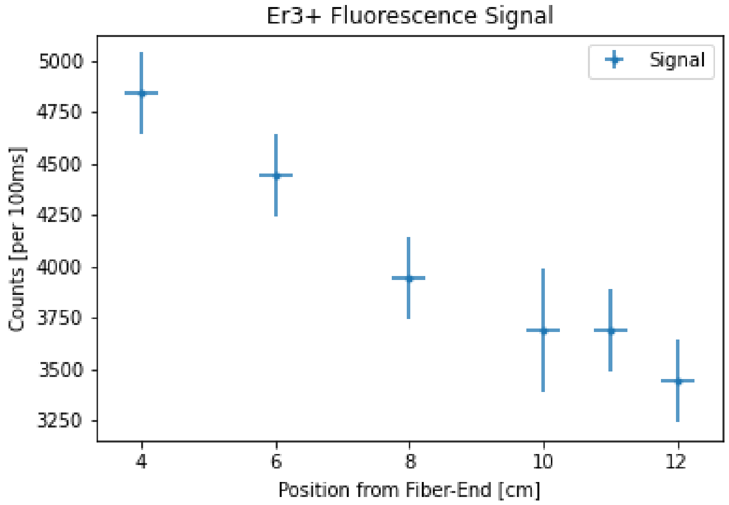

Figure 2.18: Detected upconverted Light at 540 nm from the Erbium doped Fiber at different positions from the fiber end

The second challenge lies in the dependence of the efficiency of the upconversion process on the intensity of the pump light. According to [30] and [31] the upconverted power is proportional to intensity of the pump light I to the power of an intensity dependent conversion efficiency factor c which is roughly between 1 and 2. Therefore, we assume the generated upconverted signal n is given by a proportionality factor β and the Gaussian intensity distribution of the pump laser beam $I(y)$ to the power of an intensity dependent upconversion efficiency factor c as

$$n(I) = n(P_0, w(z)) = \int_{-\infty}^{\infty} \beta I(y)^{c(I(y))}\, dy = \beta \left(\frac{2P_0}{\pi w^2(z)} \right)^2 \int_{-\infty}^{\infty} e^{\frac{-2\, c(P_0/w^2, y)\ (y-y_0)^2}{w(z)^2}}\, dx. \tag{2.19}$$

Here we inserted for $I(y)$ the intensity distribution of a Gaussian beam as described by Eq.(1.26) while $w(z)$ is the beam radius. Assuming c as constant for the used intensity ranges, we can calculate the Gaussian integral. This leads to the following count rate:

$$n(P_0, w(z)) = \beta \left(\frac{2P_0}{\pi w^2(z)} \right)^c \cdot w(z) \sqrt{\frac{\pi}{2c}} = \beta \sqrt{\frac{\pi}{2c}} \left(\frac{2P_0}{\pi} \right)^c w(z)^{1-2c}. \tag{2.20}$$

In order to check if the assumption $c \approx const$ applies, we set up a calibration measurement which produces a well known Gaussian intensity distribution and propagation of the beam radius. Therefore, we use the 1 :1 microscope consisting of two identical diffraction limited aspheres (Thorlabs AL2550H-B) for the collimating as well as for the objective lens which we also used to test the other two characterization methods. For this measurement we produced an Erbium-doped optical nanofiber with a diameter of 300 nm from a Erbium-doped fiber with a core and cladding of 150 µm and 250 µm respectively. The setup is depicted in figure 2.19. For the verification measurement, we scan the Erbium-doped nanofiber through the beam at 10 different longitudinal z-positions symmetrically around the beam focus. Afterwards we fit a Gaussian to the obtained data. As shown in for example in Fig. 2.20 (c), the measured scans can be well described by a Gaussian distribution, which illustrates that the assumption $c \approx const$ is justified for an individual scan. This procedure is repeated for eight different pump power between 2.5 mW and 35 mW. We obtain $n(P_0, w(z))$ as the count rate on the peak of the Gaussian distribution on the optical axes of every scan with a certain pump power P at a fixed longitudinal z-position with the calculated beam waist radius $w(z)$. We conduct a two-dimensional fit with the values of $n(P_0, w(z))$, P and $w(z)$ to Eq.(2.20), where β and c are the fitting parameter. Out of the fitting we determine a constant conversion efficiency as

---

*Note that in this measurement we use a standard, i.e. not tapered fiber.

$$c = 1.69 \pm 0.07. \tag{2.21}$$

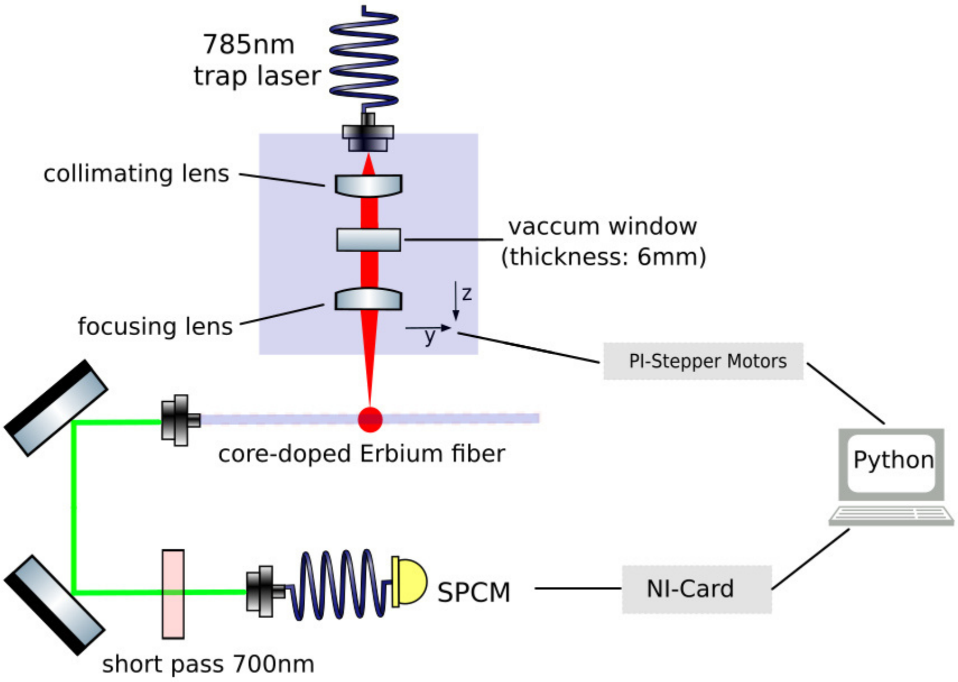

Figure 2.19: Setup to characterize the focused laser beam using an Erbium-doped optical nanofiber: A confocal microscope consisting of the collimation and objective lens is built. The nanofibers are mounted onto stepper motors to enable micrometer precision movement. The generated incoherent light is coupled out to filter out the leftover photons of the pump power.

In order to test the measurement method with the calculated conversion efficiency factor c, we want to determine the focus spot size of an already known beam. As demonstrated for the calibration of the knife edge technique and the microscope, we use the already introduced 1 :1 microscope. For this we scan the Erbium-doped nanofiber on the stepper motors through the focus spot of a laser beam with a power of 20 mW. The longitudinal step size on the z-axes is 1.0 µm while the lateral step size perpendicular to the optical axes is 0.5 µm. After every step we record the photons detected by the SPCM in a 100 ms time interval. Before starting the photon counting we wait for 0.5 s after every step in order to let possible vibrations of the nanofiber time to settle down. A correction of the count rate by the dead time of the SPCM's as well as the by the factor c is applied for every recorded position. For every scan lateral to the longitudinal z-axes, we fit a Gaussian distribution. The fitted beam radius dependent on the longitudinal z-position is depicted in 2.20 (a). The fitted Gaussian intensity distribution on the position with the smallest beam radius can be seen in Fig. 2.20 (c).

Comparing the obtained result with the data from the bare nanofiber measurment of Fig. 2.16 and Fig. 2.15, it seems that we successfully filtered out the coherent pump light as we do not observe a noisy signal caused by the interference of light scattered from surface imperfections. As the minimal beam waist radius we determine 2.67 µm ± 0.01 µm which is in good agreement with the minimal waist from the knife edge measurement of 2.47 µm ± 0.09 µm and from the imaging method with 2.95 µm ± 0.03 µm. Furthermore, the result is close to the value given by the manufacturer of 2.65 µm ± 0.5 µm and therefore is well inside the error range. Additionally, we observe a slight asymmetric distribution of the fitted waist before and after the focus in in Fig. 2.20 (a). As we can see in Fig. 2.20 (b), the high resolution of the Erbium-doped nanofiber method allows to see a minor aberration in the form of coma before the focus region which is slightly changing the fitted waist radius. The reason might be a small non-parallel alignment of the collimated beam with respect to the the optical axes of the lens system.

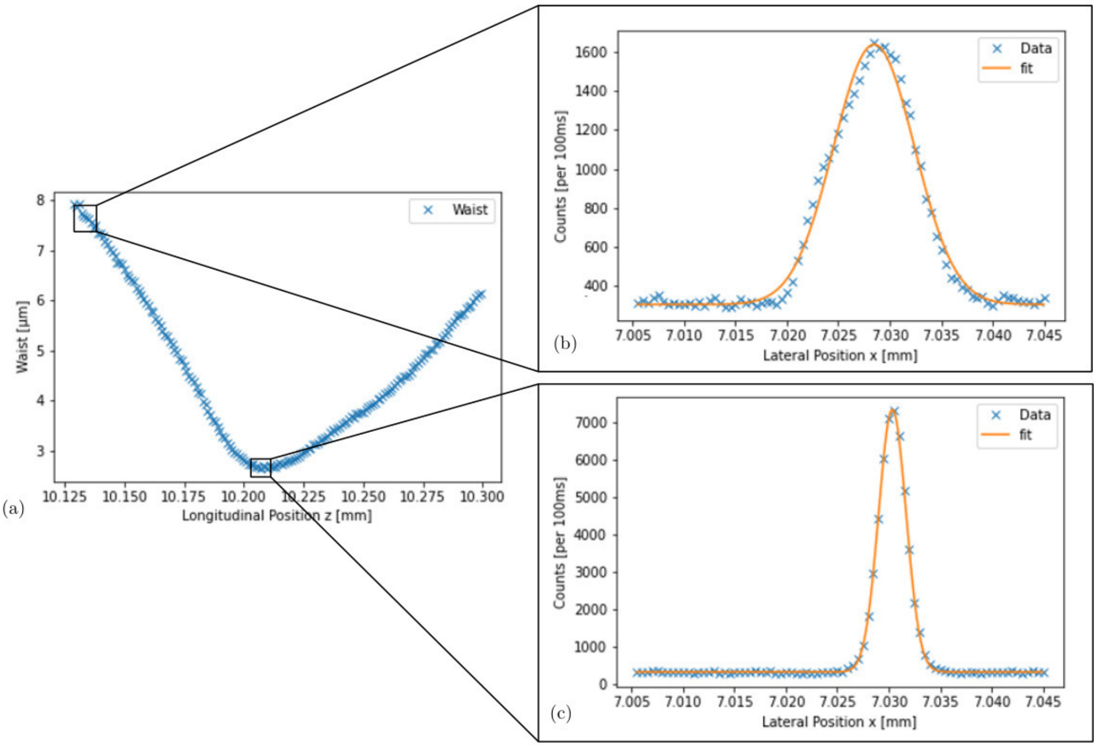

Figure 2.20: Test measurement with the Erbium-doped nanofiber using the 1 :1 microscope: (a) Fitting a Gaussian intensity distribution on every fixed longitudinal z-position leads to a minimum fitted waist of 2.67 µm ± 0.01 µm. (c) We observe a slight coma, which changes the fitted waist and therefore leads to an asymmetrical waist measurement before and behind the focus. b) Furthermore, we observe a central Gaussian peak at the position of the minimal waist, which leads to the conclusion that we are successfully detecting the incoherent light from the two photon-upconversion process at around 540 nm.

2.3.4 Lens Characterization Measurements

As we have tested our new developed method for beam characterization, we start now to characterize the focused beam. As shown in the previous measurement with the knife edge technique and the microscope, the Thorlabs objective lens introduced a large amount of aberrations into the beam. Therefore, we will just analyze the performance for the Aspericon focusing lens when using the collimation lenses with a focal length of 50 mm (TL-AL2550H)and 25 mm (TL-AL1225H).

As it is depicted in figure 2.21 (a) and (d), the minimal measured waist is 0.94 µm ± 0.02 µm when using the collimation lens with a focal length of $f = 50$ mm. For the $f = 25$ mm collimating lens, we measure a minimal waist radius of 1.51 µm ± 0.01 µm depicted in Fig. 2.22 (a) and (c). This behavior is expected from Eq.(2.4), although the measured waist for the $f = 50$ mm collimating lens is higher by a factor of 2 and the measured waist for the $f = 25$ mm collimating lens is a by a factor of 1.5 from the theoretical minimum, as it can be seen in Tab. 2.3. Nevertheless, the result is indicating that our spatial resolution was indeed limited when imaging the focus spot with microscope.

Furthermore, we are able to observe coma before the focus spot region which can be seen in Fig. 2.21 (a), (b) and 2.22 (a), (b). This kind of aberration is especially pronounced when using the $f = 50$ mm collimation lens. In fig. 2.21 (b) we see that the fitting algorithm optimizes the Gaussian function just on one peak of the intensity distribution distorted by the coma which is leading to small waist values before the focus as depicted in Fig. 2.21 (a). The coma is much less pronounced for the $f = 25$ mm collimating lens, because the smaller collimated beam size makes a slight non-parallel beam alignment less sensitive to coma.

In accordance with the knife edge and microscope measurements, we observe an Airy-ring pattern behind the focus spot region. This effect is more pronounced for the $f = 50$ mm collimating lens depicted in Fig. 2.21 (c) as for the collimation lens with $f = 25$ mm depicted in Fig. 2.22 (c). The large collimated beam size for the $f = 50$ mm collimating lens leads to a larger amount of diffraction caused by the truncation of the beam by the objective lens aperture.

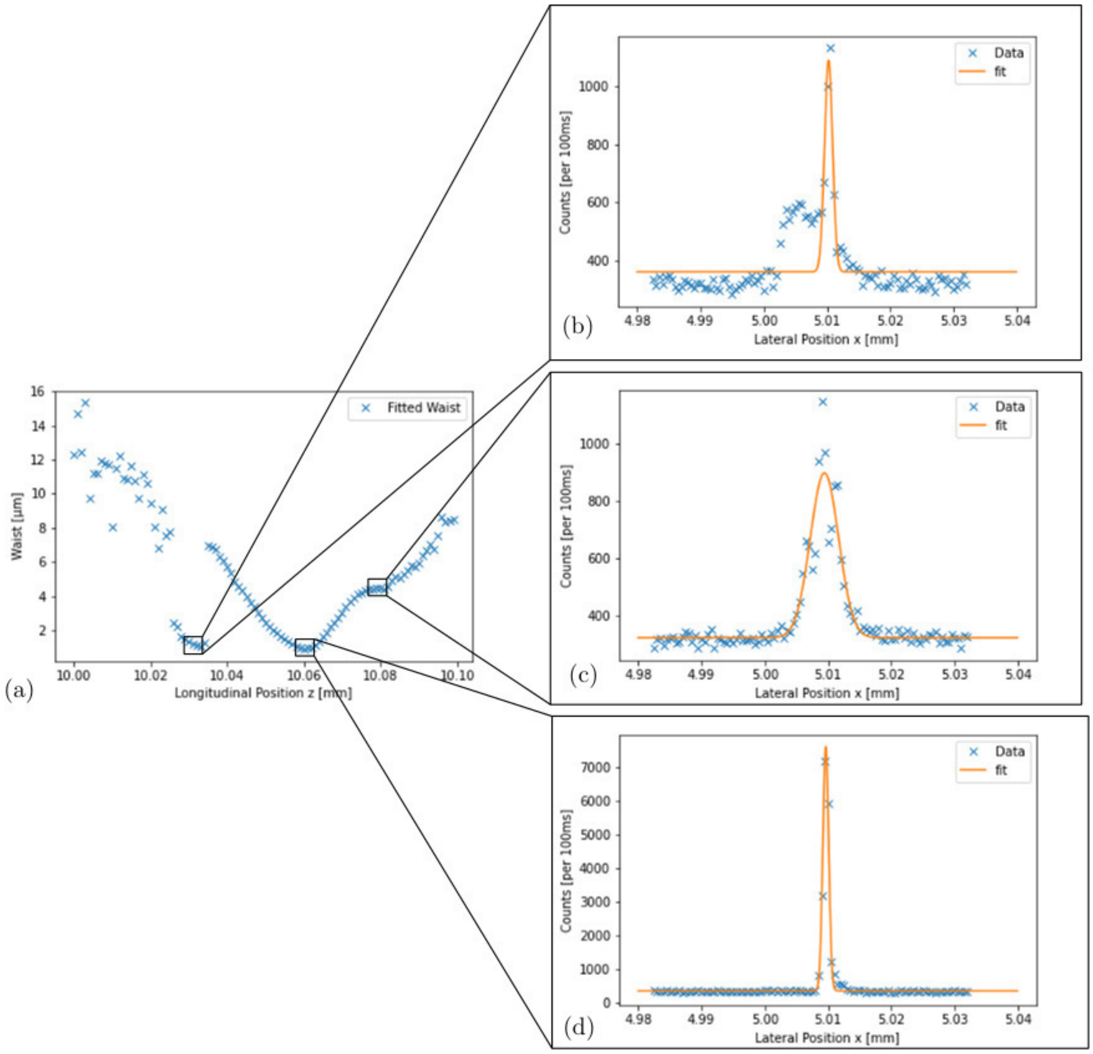

Figure 2.21: Characterization measurement with the Erbium-doped nanofiber using the Asphericon AS-AHL12-10 objective lens and the Thorlabs $f = 50\,\mathrm{mm}$ collimating lens: (a) Fitting a Gaussian intensity distribution on every fixed longitudinal z-position leads to a minimum fitted waist of $0.92\,\mu\mathrm{m} \pm 0.02\,\mu\mathrm{m}$ with (d) a central Gaussian peak at the position of the minimal waist. Furthermore, we observe coma before the focus (b) and an Airy-ring like intensity distribution behind the focus (c).

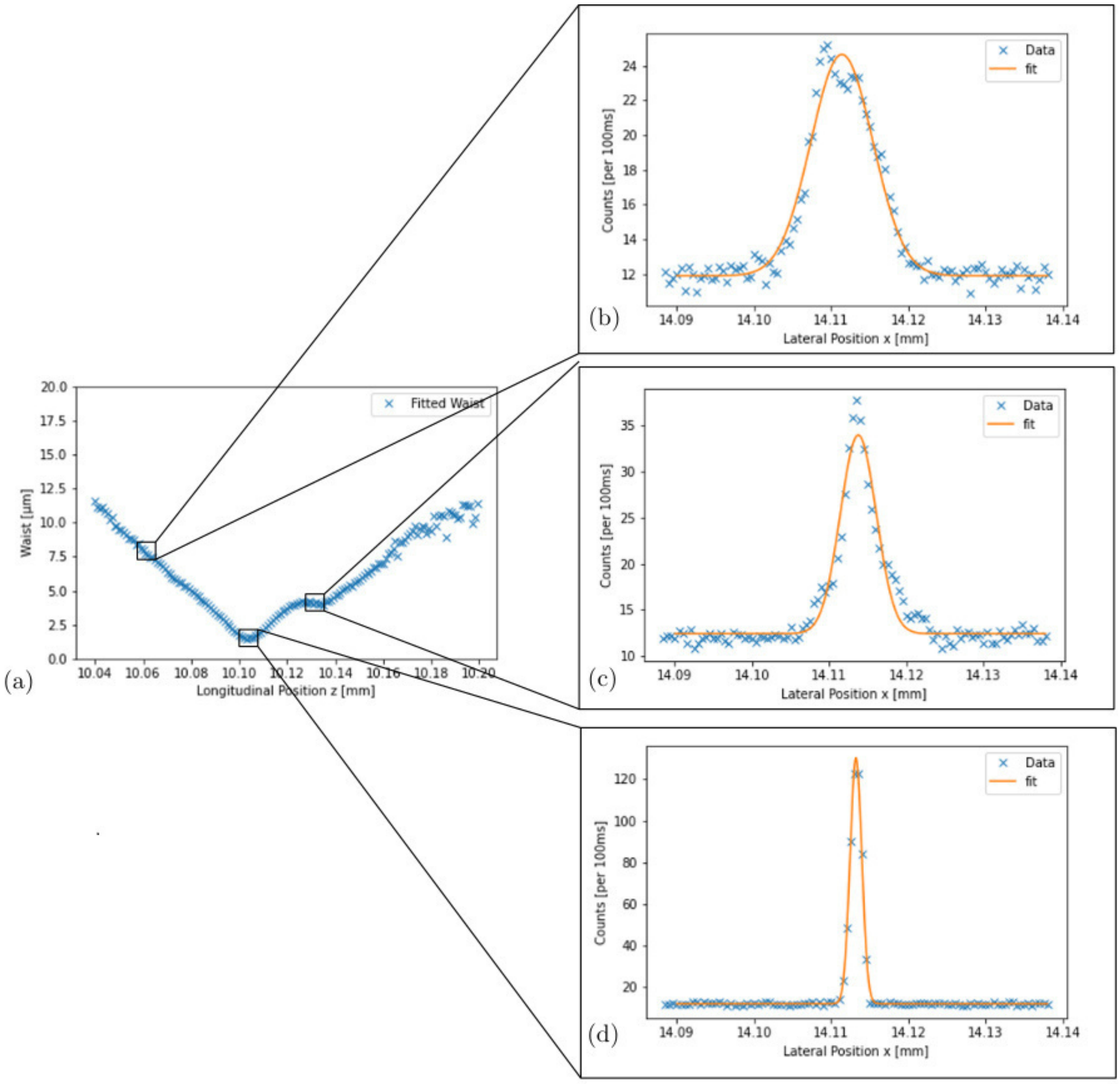

Figure 2.22: Characterization measurement with the Erbium-doped nanofiber using the Asphericon AS-AHL12-10 objective lens and the Thorlabs $f = 25\,\mathrm{mm}$ collimating lens: (a) Fitting a Gaussian intensity distribution on every fixed longitudinal z-position leads to a minimum fitted waist of $1.51\,\mu\mathrm{m} \pm 0.01\,\mu\mathrm{m}$ with (d) a central Gaussian peak at the position of the minimal waist. Furthermore, we observe slight indications of coma before the focus (b) and an Airy-ring like intensity distribution behind the focus (c).

2.4 Summarizing the Characterization Methods

In oder to characterize the focus spot of the confocal microscope of the dipole trap and fluorescence collection optics, we employed three different measurement techniques: the scanning knife edge method, the magnification of the focal spot with a microscope on a CCD-camera and the scanning Erbium-doped nanofiber method. The results of the measurements are summarized in Tab. 2.3.

The knife edge technique allows to determine the minimal focus waist as well as the beam propagation factor M^2 and a corresponding focus waist as it is able to measure the beam radius in the near field and in the far field further than two Rayleigh lengths away of the focus spot. Nevertheless, this technique is relatively insensitive to small changes in intensity distribution, because it only measured a relative decrease of the total transmitted power on the photodiode as the razor blade is moving through the beam. Furthermore, this method might be sensitive to small misalignments of the knife edge in respect to the beam axis. Also, it is not easy to verify that the sharpness of the area of the razor blade used for the measurements is not degraded by handling or uncertainties in the production process. Therefore, the results of this measurement can be used as an upper boundary for the focus spot size.

Imaging the focus spot with the microscope setup gives a better insight into the intensity distribution of the beam around the focus spot. Also, it allows to determine the minimal waist radius of the focused beam. Because it is more sensitive to faster oscillations of the intensity distribution, the determination of the beam propagation factor M^2 would be challenging, as an approximated Gaussian fit to a complex intensity distribution has to give a waist value where the $1/e^2$ decrease of total intensity is correctly determined. Furthermore, the minimal detectable spot site is limited by the NA of the Mitutoyo objective. This seems to be the case for the measured minimal waists using the Asphericon objective lens.

The Erbium-doped scanning nanofiber method is well suited to study the properties of the tightly focused beams. Due to its small diameter $d = 300\,\text{nm}$ nanofiber probe, this method is very sensitive to fast changes of the intensity distribution at the measured plane. It not only detects Airy-ring like intensity distributions but also slight coma aberrations. Of course, one has to carefully interpret the measured data as the signal represents an integrated intensity distribution along the fiber axis. Therefore, a determination of the beam propagation factor would by very challenging with this method. Nevertheless, it seems like this method is well suited to measure the tight focused spots when using the Asphericon objective lens.

As it became clear from the knife edge and microscope characterization measurements the Thorlabs TL-AL1210 objective lens introduces significantly more wavefront errors into the focused beam as compared to the Asphericon AS-AHL12-10 lens. Although the difference between both RMS wavefront errors is rather small with $0.1\,\mu\text{m}$, the focusing quality of the Thorlabs lens suffers heavily. The aberrations are leading to a non-Gaussian intensity distribution, which has an uncontrollable influence on the trapping frequencies as well as on the efficiency of fluorescence collection. We observe a broadening of the focus spot waist, which could lead to a failure to reach the collisional blockade regime for trapping single ^{85}Rb-Atoms. Consequently, we choose the Asphericon AS-AHL12-10 as the objective lens in all following measurements, which was also put inside the vacuum chamber to act as the final objective lens for our experimental setup.

Lens Specifications				
Collimating lens	TL-AL2550H	TL-AL1225H	TL-AL2550H	TL-AL1225H
	$f = 50.0$ mm	$f = 25.0$ mm	$f = 50.0$ mm	$f = 25.0$ mm
Objective lens	Thorlabs	Thorlabs	Asphericon	Asphericon
Theoretical Waist	0.53 µm	1.06 µm	0.53 µm	1.06 µm
Beam Radius	6 mm	3 mm	6 mm	3 mm
Objective Lens Wavefront Error	< 0.5 µm RMS	< 0.5 µm RMS	< 0.39 µm RMS	< 0.39 µm RMS
Knife Edge Measurement				
Minimal Waist	(7.53 ± 0.16)µm	(7.09 ± 0.24)µm	(3.28 ± 0.15)µm	(1.62 ± 0.09)µm
M^2-Fitted Waist	(7.41 ± 0.01)µm	(7.37 ± 0.06)µm	(2.72 ± 0.22)µm	(1.80 ± 0.05)µm
M^2-factor	13.91 ± 1.49	7.13 ± 0.05	4.75 ± 0.22	1.70 ± 0.05
Microscope Measurement				
Minimal Waist	(2.31 ± 0.09)µm	(2.47 ± 0.08)µm	(1.93 ± 0.05)µm	(1.84 ± 0.01)µm
Scanning Erbium-doped Nanofiber Measurement				
Minimal Waist			(0.92 ± 0.02)µm	(1.51 ± 0.01)µm

Table 2.3: Results of the focus spot characterization measurements

When using the Asphericon objective lens, we observed a decrease of focus spot waist as we increase the collimated beam diameter corresponding to a collimation lens with greater focal length. This seems to verify the predication based of formula 1.33. In order to get a maximum detection efficiency for the fluorescence collection as well as a very tight dipole trap, the collimation lens with a focal length of $f = 50$ mm can be used. Nevertheless, the $f = 50$ mm collimation lens gives a collimated beam diameter of 12 mm. Therefore, aligning the planned setup depicted in Fig. 1.2 can be extraordinarily challenging, especially when using MaxLine Filters with a diameter of $f = 25$ mm in an angle of 10° to 20° in order to combine different beam paths of the setup. As all different characterization methods show, using the $f = 25$ mm collimation lens together with the Asphericon objective lens results in focus waist of around 1.6 µm. This should still be tight enough to reach the collisional blockade regime with the dipole trap easily. Therefore, it would be safe to use collimation lenses with $f = 25$ mm or even smaller focal length as a first try to trap single atoms.

3

Trapping of Single Atoms

In the last chapter we characterized the focus spot region of the confocal microscope. Based on this, we set up our trapping and fluorescence collection optics and perform first tests on atom trapping described in this chapter.

In front of the vacuum chamber we built up the setup depicted in Fig. 3.1. The fluorescence of the D2-transition at 780 nm is separated from the dipole trap laser at 785 nm by using a Semrock MaxLine filter (LL01-785 FWHM 3.0 nm). The dipole trap laser is reflected from that filter at an angle of 14° to the surface normal. Before the fluorescence beam is coupled into a single mode fiber and detected by an SPCM, we employ two bandpass filters at 780 nm (Semrock MaxLine LLD1-780 FWHM 3.0 nm) in order to filter out residual scattered light from the dipole trap. As it provides a tight focus with a Gaussian intensity distribution, we use the Asphericon AHL12-10 as the objective lens inside the vacuum chamber (see previous chapter). As a first test and to further decrease diffraction effects in the focus spot region, we are using a collimating lens with 15 mm focal length for both beams. This enables us to reach the collisional blockade regime with a dipole trap focus waist of $w_0 = 2.4\,\mu\text{m}$. The alignment of this setup can be conducted by putting in a flip mirror (by now not a transmissive mirror) and using the beam path on the left hand side of Fig. 3.1. It consists of the same 6 mm thick vacuum window out of fused silica and the Asphericon objective lens. In order to spatially overlap the trap and fluorescence beams, we shine in a laser at 780 nm from the fluorescence detection fiber, the focus spot of which, is overlapped with the dipole trap focus on the microscope. Furthermore, we check the alignment by measuring and subsequently maximizing the coupling of both lasers into a single mode fiber.

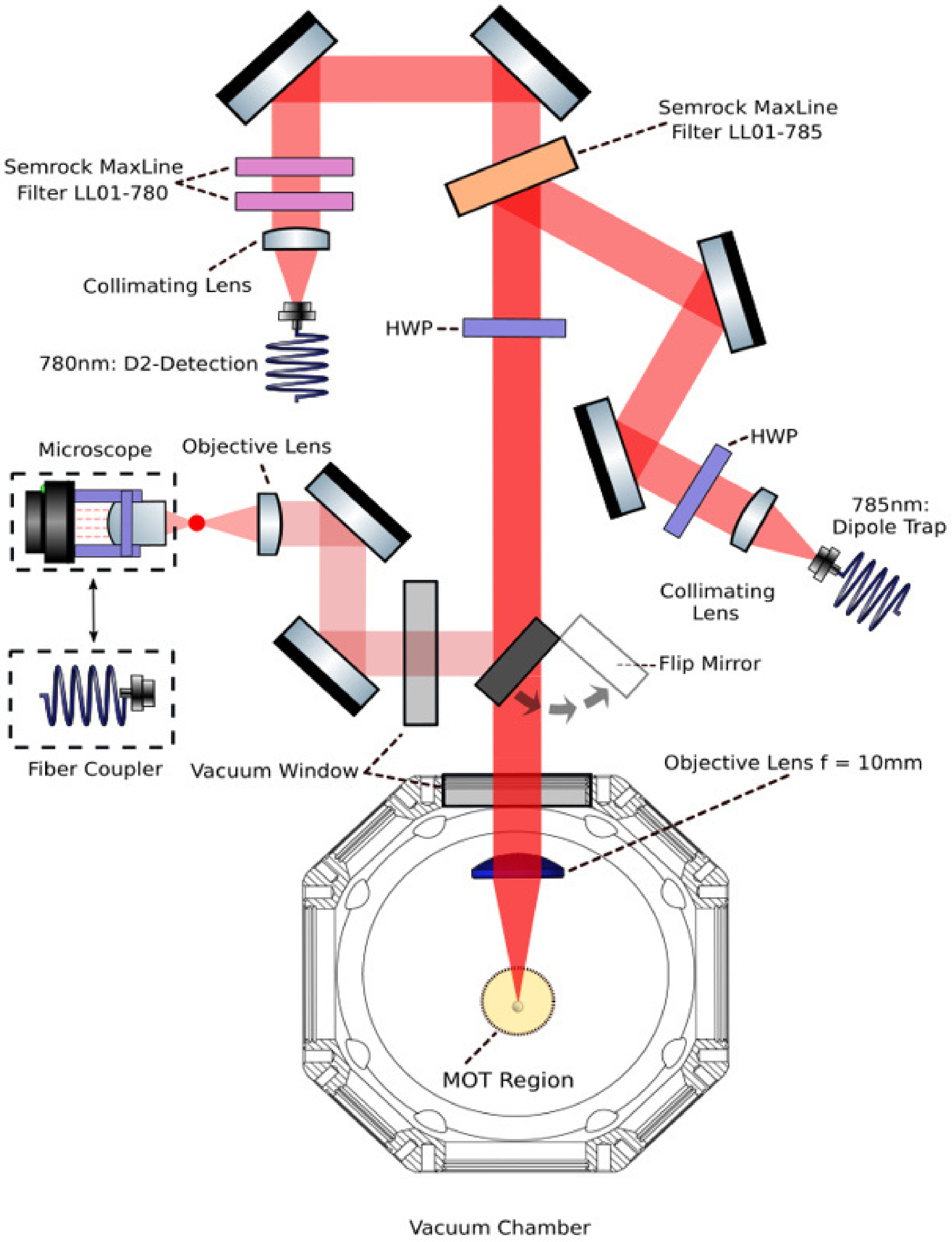
Semrock MaxLine
Filter LL01-785
Semrock MaxLine
Filter LL01-780
Collimating Lens
HWP
780nm: D2-Detection
Microscope
Objective Lens
HWP
785nm:
Dipole Trap
Collimating
Lens
Flip Mirror
Fiber Coupler
Vacuum Window
Objective Lens f = 10mm
MOT Region
Vacuum Chamber

Figure 3.1: Optical setup used to trap single atoms: On the basis of the focus spot characterization of chapter 2, we use the Asphericon AHL12-10 as the objective lens and a 15 mm focal length lens for collimating the trapping laser as well as the fluorescence beam path. The spatial overlap of the beams inside the vacuum chamber is realized by viewing both focal spots on a microscope as well as maximizing the coupling of the both beams into a single mode fiber in the alignment arm.

3.1 Observation of Single Atoms and Atom Lifetime

After the alignment of our setup, we can start trapping single ^{85}Rb-atoms. The rubidium atoms are created by dispensers at the side of the science chamber. The low pressure environment at approximately 1×10^{-9} mbar inside the vacuum chamber is maintained by an ion getter pump. As described in chapter 1, the atoms are cooled and trapped inside the MOT. As the focus spot region of the dipole trap is aligned with the center of the MOT, atoms are cooled by the MOT and can be loaded into the dipole trap.

In order to observe the atoms in real-time, we continuously monitor the photons detected in the fluorescence collection optics. Fig. 3.2 shows a typical a telegraph-like signal where the detected photon rate changes back and forth between two distinct levels. We observe an increase from the background count rate of around 5 counts/20ms to around 60 counts/20ms, when a single atom enters the dipole trap volume. We only observe two distinct levels of the fluorescence count rate, meaning that we are only trapping single atoms inside the dipole trap. Figure 3.3 shows a histogram of the detected count rates over a long time measurement. We can clearly observe two distinct peaks which follow a Poissonian counting statistics. The first peak is explained by a background count rate due to the dark counts of the SPCM and residual stray light. The second peak is caused by the fluorescence scattering of the single Rubidium atom. At twice the count rate of the the single atom peak we do not observe a third peak. This shows that our dipole trap operates in the collisional blockade regime where only single atoms can be trapped.

A crucial parameter of the planned experiment is the lifetime of the atom inside the dipole trap. It can be determined from the fluorescence traces by measuring the duration which each atom spends in the trap across a long time measurement. Fig. 3.4 shows the histogram of the measured trap lifetimes to which we fit an exponential decaying function. From this, we extract a 1/e decay time of $\tau \approx 300\,\mathrm{ms}$. This lifetime is measured with the MOT on. Therefore the lifetime is not only limited by the parametric heating from instabilities of the dipole trap and collisions of the trapped atom with the background gas, but also by the collisions of two cold atoms as they are attracted to the center of the dipole trap. Consequently the measured life time is a lower bound for the achievable lifetime once the MOT is completely switched off.

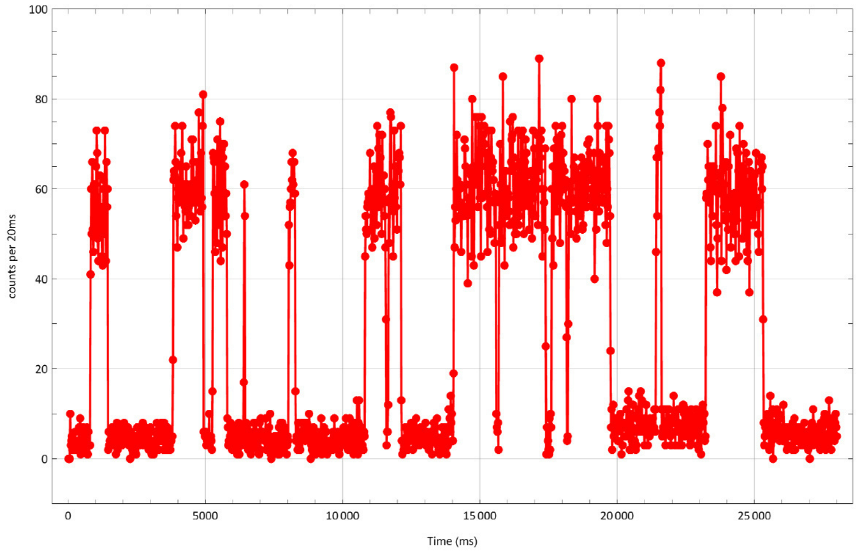

Figure 3.2: Telegraph Signal of the florescence collection: Entering of a ^{85}Rb-atom into the dipole trap leads to an increase of the the signal from the background level of 5 counts/20ms to 60 counts/20ms.

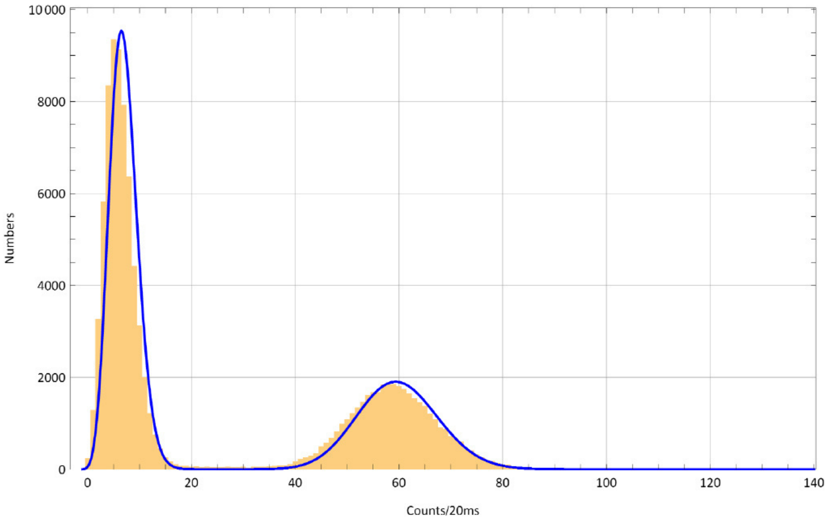

Figure 3.3: Histogram of the detected photon counts: The first peak at 7 counts/20ms corresponds to the background count rate. The second peak at around 60 counts/20ms signalizes the trapping of one atom. The absence of additional peaks at 120 counts/20ms and 180 counts/20ms confirms that only single atoms are trapped and shows that our dipole trap operates inside the collisional blockade regime.

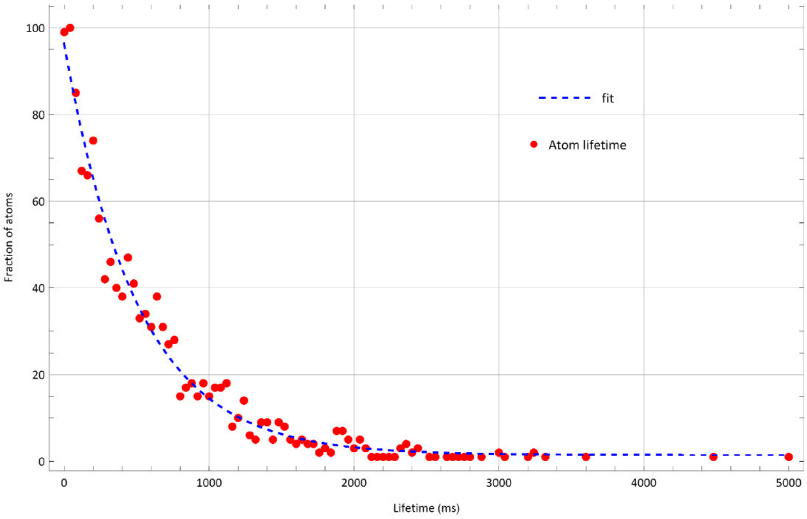

Figure 3.4: Exponential fit to the lifetime of each trapped single atom leads to a lifetime τ of 300 ms.

3.2 HANBURY-BROWN TWISS MEASURMENT

Another way to verify that we are only trapping single atoms is to analyze the temporal statistics of the fluorescence photons. In order to quantify the temporal intensity fluctuation, we introduce the second order correlation function $g^{(2)}(\tau)$. The function describes the probability of detecting a photon at the time $t+\tau$ conditioned on a photon detection event at time t where τ is the time difference between both detection events. This term is then normalized by the long time averaged intensity. We can describe the second order correlation function $g^{(2)}(\tau)$ for a stationary, plan-parallel beam of light with a single polarization while detecting the correlation events at a common observation point as described in [32] by

$$g^{(2)}(\tau) = \frac{\langle \hat{E}^-(t) E^-(t+\tau) E^+(t+\tau) E^+(t) \rangle}{\langle \hat{E}^-(t) \hat{E}^+(t) \rangle^2}. \tag{3.1}$$

Here $\hat{E}^+$ and $\hat{E}^-$ are the quantum mechanical electric field operators and the angle brackets $\langle \cdots \rangle$ denote the long-time average. A single atom can only emit one photon at a time because the exited state has a finite lifetime so the atom has to be reexited by the driving laser field in order to emit the next photon. Therefore we should observe photon antibunching for a single atom with $g^{(2)}(0) < 0.5$. For a classical light field we can derive by using Cauchy's inequality that $g^{(2)}(\tau) \geq 1$. When observing coherent light from a laser, we observe $g^{(2)}(\tau) = 1$ including $\tau = 0$ because the photon stream exhibits random Poissonian photon statistics. For a thermal light source consisting of many independently emitting atoms, for example a discharge lamp, we expect photon bunching with $g^{(2)}(0) > 1$.

In order to measure the second order correlation function for the light emitted from a single atom, we conduct a so-called Hanbury-Brown Twiss measurment [33]. As shown in Fig. 3.5. The incoming fluorescence light is coupled into a single mode fiber and sent onto a 50 :50 fiber-beamsplitter. An SPCM is attached to both output ports to detect the single photons. A time tagger measures the arrival time of each photon detection event

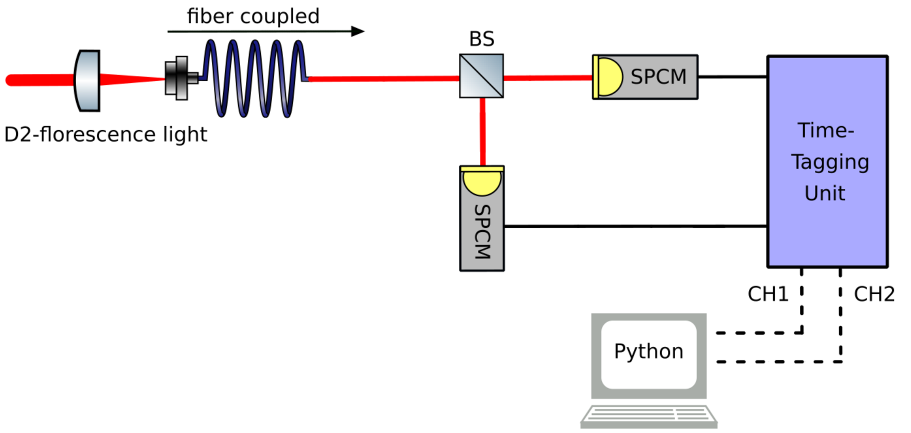

Figure 3.5: Hanbury-Brown Twiss setup: The fluorescence light from the dipole-trapped atom is coupled into a single mode fiber. Afterwards, the light is split by using a 50 : 50 fiber-beamsplitter. At each output of the beamsplitter we detect the photons with SPCMs and register the photon arrival time with a time-tagging unit, in order to measure the second order correlation function $g^{(2)}(\tau)$.

and sends it to the computer. Therefore, we measure the time difference $\tau = t_1 - t_2$ between the detection event in the detectors. Histogramming up these time differences and normalizing as well as correcting the results for the background counting rate of the SPCM, we obtain the second order correlation function $g^{(2)}(\tau)$ as shown in Fig. 3.6. We can clearly observe a dip to 0.02 ± 0.05 normalized corrected coincidences, which indicates anti-bunching and therefore the trapping of a single atom. Because the atom has to be reexited by the driving laser field in order to emit the next photon, we can see Rabi-oscillations with a frequency of around 45 MHz. As the time τ increases we observe a damping of this Rabi oscillations, due spontaneous emission of the atom.

In this chapter we successfully used the characterized dipole trap and collection optics to trap single ^{85}Rb-atoms. By analyzing the photon statistics of the collected fluorescence light we confirmed the presence of the collisional blockade effect. Furthermore we determined a lower boundary of the single atom lifetime to 300 ms. By performing a Hanbury-Brown Twiss measurement we observed anti-bunching of the photons from the fluorescence light and we were able to observe Rabi-oscillations.

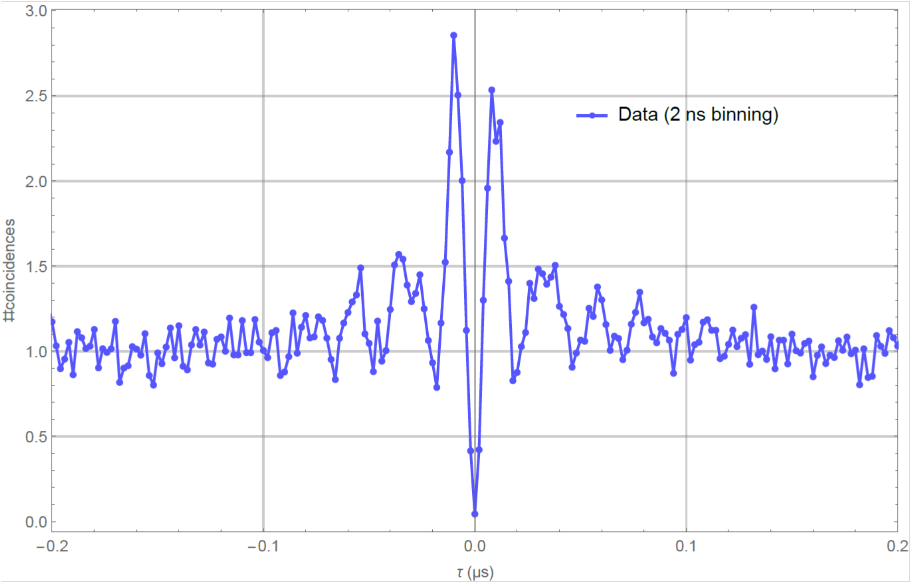

Figure 3.6: Measured and background corrected second order correlation function $g^{(2)}(\tau)$: We observe a clear indication of anti-bunching as the normalized coincidences counts drop to 0.02 ± 0.05 at $\tau = 0$. Also Rabi-oscillations with a frequency of around 45 MHz are visible.

4

TOWARDS ATOM TRANSPORT INTO THE RESONATOR'S WGM

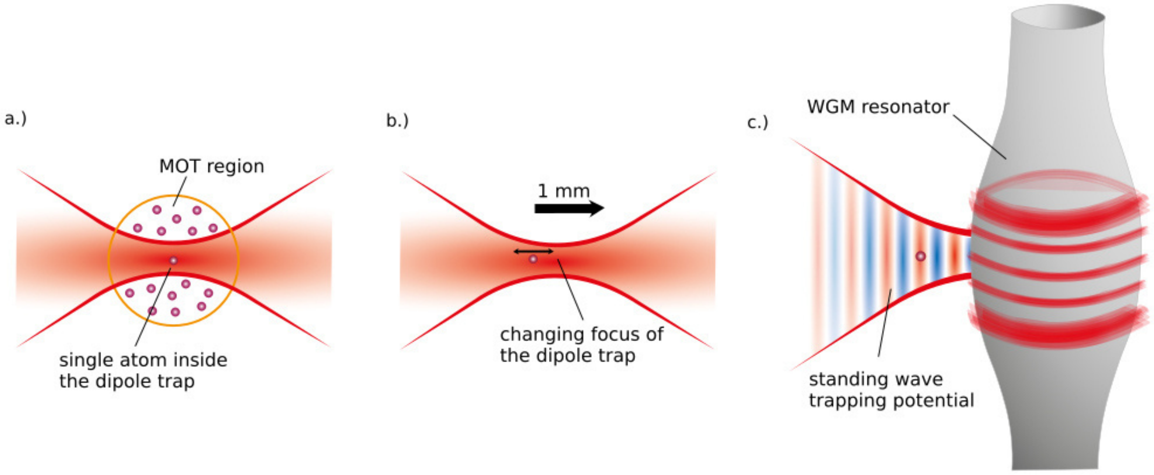

Figure 4.1: Sketch of the atom transport procedure: (a) A single ^{85}Rb-Atom is trapped inside the dipole trap after its preparation in the MOT. (b) The atom transport over a distance of 1 mm is realized by moving the dipole traps focus with an electric tunable lens. (c) Formation of a standing wave trapping potential in front of the surface leads to the trapping of atoms multiple potential minima away from the WGM resonator's surface.

After the preparation of ^{85}Rb-Atoms inside the MOT, we trap single atoms in the dipole trap approximately 1 mm away from the resonator's surface as sketched Fig. 4.1 (a). In order to trap the atoms in the WGM of the resonator, we plan to realize an atom transport mechanism from the MOT to the resonator's position based on an electric tunable lens as seen Fig. 4.1 (b). Therefore, we study the feasibility of realizing the atom transport with the electric tunable lens in the first part of this chapter. When the focus of the dipole trap is positioned on the resonator's surface as sketched in Fig. 4.1 (c) a standing wave potential is formed due to the inference of the incident and retroreflected beams from the surface preventing the atom to reach the evanescent field of the resonator's WGM with a high probability. Therefore, in the second part of this chapter, we examine a method to modulate the standing wave trapping such that the probability of trapping single atoms

$\lambda/4$ from the resonator's surface is increased.

4.1 Atom Transport with an Electric Tunable Lens

In the experiment the cold ^{85}Rb-Atoms are prepared in the MOT and subsequently trapped in the dipole trap approximately 1 mm away from the WGM resonator. In order to do perform CQED, the atom has to be transported to a distance of about 100 nm to 200 nm from the resonator's surface such that it can couple to the resonator's evanescent field of the whispering-gallery mode. In the previous experimental setup, the dipole trap, with its focus position on the resonator's surface, was loaded via an atomic fountain [11]. This procedure only allowed for probabilistic trap loading with an efficiency of 0.7%. Also the trap lifetime was limited to 2 ms as the atoms were relatively hot, after delivery into the trap using the atomic fountain. In the current setup we aim to realize a more deterministic method of atom transport. An optical conveyor belt as shown in [34] would be difficult to implement in our setup. First, it is not suitable since we would need a second trapping beam focused through the resonator which would lead to the distortion of the intensity distribution of the Gaussian beam. Second, it would be a huge experimental challenge to stabilize the experimental setup such that the laser beam reaches interferometric stability. Placing the MOT beside the resonator to move the trap from the side into the resonator mode as shown in [12] is not possible as there is no stable trajectory from the free space trap towards the first potential minima close to the resonator's surface. This would prevent controlled loading of a single atom, as the beam focus is moved transversally to the beam axis.

After careful consideration of the aforementioned methods, we decided to use a method based on a movable optical dipole trap. We employ an electric tunable lens (Optotune EL-16-40-TC-VIS-20D) whose focal length can be adjusted to move the focus position from the MOT region to the the position of the resonator's surface. In the following chapter we explore the feasibility of such an atom transport mechanism.

4.1.1 Working Principle of Liquid Lenses

The key ingredient to realize atom transport in our experiment is the electric tunable lens (ETL) as it is responsible for changing the dipole traps focus position. In order to get an insight into the technical limitation when performing atom transport with the ETL, we first have to understand the basic working principle of *Optotunes* liquid focus tunable lenses. When changing the applied current, our ETL (Optotune EL-16-40-TC-VIS-20D) is able to change its focus over a range of −10 dpt to 10 dpt or from a focal length of $f = -100$ mm to $f = 100$ mm from the lens's principal plane.
As shown in Fig. 4.2, it consists of a liquid silicone oil inside a silicone-based polymer membrane. The curvature of the lens can be regulated by changing the pressure of the ring which is encompassing the container. Like in a loudspeaker, the ring is mechanically connected to a voice coil. If a current is applied, the coil will be moved further in or out of the magnetic field of a permanent magnet by the Lorentz force. Because the voice coil is connected to the pressure regulating ring via an electromagnetic actuator, an applied current on the voice coil changes the pressure onto the liquid and therefore the curvature

of the elastic membrane encompassing the liquid [35] [26].

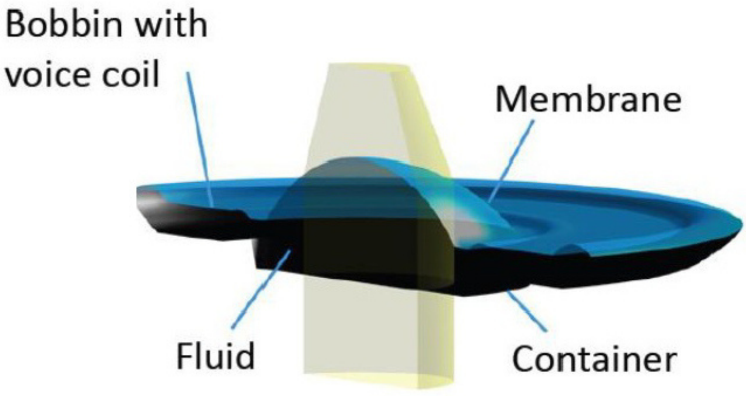

Figure 4.2: Design of the electric tunable lens (ETL) (picture from [26])

4.1.2 Characterizing the Electric Tunable Lens

The goal of this chapter is to evaluate whether the ETL is suitable for transporting of ^{85}Rb-Atoms inside the optical dipole trap from the MOT-position to a position close to the resonator's surface. The overall distance of the transport is approximately 1 mm. Because the wavefront error of all liquid lenses from *Optotune* increases with curvature or focal power [26], we design the optical system such that the dipole trap is located at the resonator's surface for a focal length $f \approx \infty$, given by 0 dpt on the ETL. Therefore the lens acts as a mere window and should introduce minimal aberration when the experiments will be performed with the atoms close to the resonator's surface. The ETL itself is vertically mounted inside a cage system at the anticipated distance from the objective lens in the final setup of 250 mm. The vertical mounting is recommended by the manufacturer to prevent asymmetric distortions to the liquid, and therefore the lens curvature due to gravity [26]. The whole setup is depicted in Fig. 4.3. By simulating the beam propagation with ray transfer matrices, it was calculated that the position of the MOT, 1 mm before the resonator's surface, will be reached with a focal power of 2.8 dpt or a focal length $f = 360$ mm of the ETL. Therefore the required tuning range of the ETL is approximately between 0 dpt and 3.0 dpt. The *EL-16-40-TC-VIS-20D* offers a tuning range between -10 dpt and 10 dpt. Therefore, the lens is able to change the focus spot position as required by the experimental setup.

4.1.3 Transient Behavior

Understanding the transient, or time-dependent, behavior of the ETL when switching the focus of the dipole trap from the MOT position to the resonators' surface position is of great importance for the atom transport. As the focus of the dipole trap is moving, the atom is accelerated inside the trap. Therefore, we have to first make sure that the atom is not kicked out of the trapping potential due to this acceleration. In the following, we want to compare the acceleration forces with the trapping forces of the dipole trap.

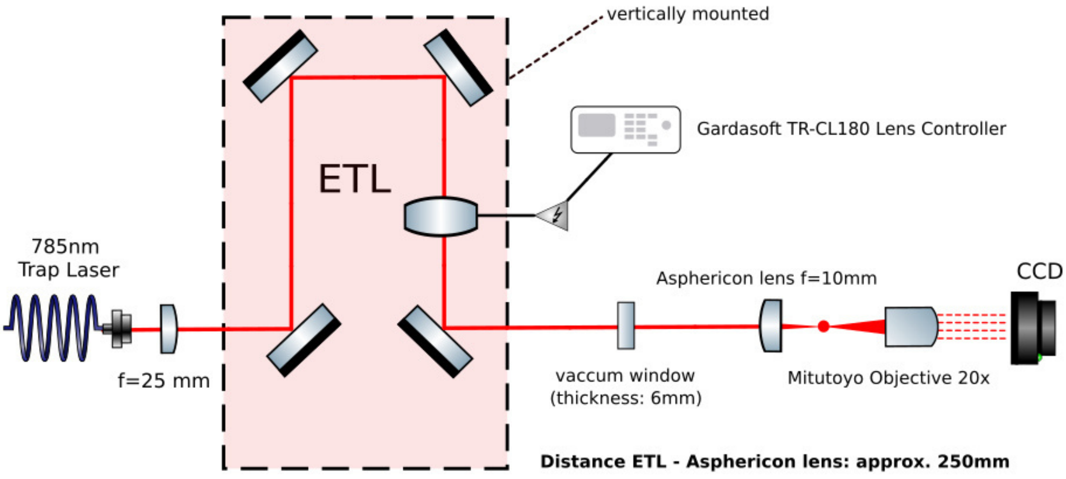
vertically mounted
Gardasoft TR-CL180 Lens Controller
ETL
785nm
Trap Laser
f=25 mm
Asphericon lens f=10mm
CCD
vaccum window
(thickness: 6mm)
Mitutoyo Objective 20x
Distance ETL - Asphericon lens: approx. 250mm

Figure 4.3: Setup used to characterize the ETL: The dipole trap laser is sent through the vertically mounted ETL. Afterwards, the beam passes a 6 mm thick vacuum window which simulates the viewport of our vacuum chamber. The objective lens is at the same position as expected in the final experimental setup. The microscope, which was calibrated in chapter 2.2, is used to view at the focal spot while changing the focal length or optical power (dpt) of the ETL.

Let's recall Eq.(1.21) to obtain a rough estimation of the maximum allowed acceleration acting on the atom during the transport process inside the dipole trap:

$$U(\vec{r}) = -\frac{3\pi c^2}{2\omega_0^3}\left(\frac{\Gamma}{\omega_0 - \omega} + \frac{\Gamma}{\omega_0 + \omega}\right) I(\vec{r}). \tag{4.1}$$

On the optical axes in the fundamental mode of the Gaussian beam, the trapping potential is given by

$$U(r=0,z) = -\frac{3Pc^2}{\omega_0^3}\frac{1}{w^2(z)}\left(\frac{\Gamma}{\omega_0 - \omega} + \frac{\Gamma}{\omega_0 + \omega}\right). \tag{4.2}$$

The maximum acceleration that an atom can experience while staying in the trap can be determined by calculating the force imparted onto the cold ^{85}Rb-Atoms which is necessary to elevate the atom to an untrapped position. As we want to transport the atom along the optical axes into the z-direction, the maximum force that the trapping potential can provide is reached at the turning point of the dipole potential in axial z-direction with

$$\frac{\partial^2 U(r=0,z_t)}{\partial z^2} = 0 \tag{4.3}$$

from which we obtain $z_t = \pm 7.5\,\mu\text{m}$. The acceleration is simply given by the gradient of the potential at the position of the turning point z_t

$$a_{max} = -\frac{1}{m_{Rb}}\nabla U(r=0,z_t). \tag{4.4}$$

For a trap depth of $T = 1\,\mathrm{mK}$, a focus waist of $1.8\,\mu\mathrm{m}$ which is easy reachable with the $f = 25\,\mathrm{mm}$ collimating lens as explained in chapter 2 and a trap power of $P = 1.8\,\mathrm{mW}$, we calculated a maximum acceleration of around $5\,000\,\mathrm{m\,s^{-2}}$. This is an upper boundary as it does not take into account the movement of the atom inside the trap at the beginning and during the transport process.

Measurement Setup: In order to measure the acceleration forces the atom experiences while being transported in the dipole trap, we use the setup depicted in Fig. 4.3. After the beam is collimated behind the fiber, it is sent through the vertically mounted ETL which changes its focal length by applying a control current with the lens controller (Gardasoft TR-CL180). Afterwards, the beam propagates through a 6 mm pure silica glass plate, which simulates the viewport of our vacuum chamber, to the Asphericon objective lens. Both the glass plate as well as the lens are placed at the same distance from the ETL as they will be in the final setup. After the beam is focused down, we use a self-built microscope to view the focus position. For that, we use the same setup with the Mitutoyo 20x objective, that was tested and used in chapter 2.2 for the characterization of the beam foci. Then the beam is viewed on the MvBlueFox3-1013GE CCD-camera.

For the atom transport process, we are interested in the optical response of the ETL when changing its supply current as fast as possible with the lens controller. This is what we will call a switch in the following. In order to measure the acceleration, we have to measure velocity of longitudinal z-position focus change on the optical axes. For this, we want to measure how the waist of the focused beam is changing as the focal length or optical power of the ETL is switched. For this, we image a fixed spot of the beam on the optical axis with the microscope setup.
This procedure leads to two problems when determining the z-position via a waist measurement. First, the dependence of the waist size from the z-position of the focus is not clear because the ray transfer beam propagation script does not take aberration and diffraction effects induced by the optical components of the system into account which have an influence on the waist size as seen in chapter 2. Secondly, the focused beam has a large divergence angle to create a tightly focused trap. Therefore the intensity on the CCD-camera is reduced drastically when not viewing directly at the focus spot of the dipole trap. Because we want to measure the transient behavior in a regime of a few milliseconds, we are furthermore not able to increase the exposure time of the CCD to increase the observable beam range. This would lead to a smoothing out of a potentially unstable trajectory.

In order to get around this problem, we slightly overexpose the camera while looking at the changing z-position of the focus. Consequently, we are able to see a picture of the beam in a range from 0.0 dpt to 1.0 dpt applied to the ETL even though the focus is away by a few hundreds of micrometer. Because the overexposing changes the waist of the imaged beam, we have to calibrate the measurements. For this, we calculate the z-position of the focus spot in the optical system for a given focal length or optical power at the ETL with a Python beam propagation program. Afterwards, we align the microscope to the focus on the starting position of the potential transport step. Next, we change the focus of the lens from 1.0 dpt to −0.5 dpt with a step size of 0.05 dpt. On every step we take a picture and calculate the waist by fitting a Gaussian curve onto the data. Now, we can calibrate the measured waist sizes to the corresponding calculated z-position of the focus as we know the applied optical power on the ETL. Afterwards, we can interpolate between every measured waists in order to get a calibration curve. The results of this procedure are depicted in 4.4. Because we integrate over all pixel columns to get the x-waist and over all pixel rows to get the y-waist, we get two calibration curves. Nevertheless, the difference of both curves is minor as one can see in Fig. 4.4 (a) and Fig. 4.4 (b) due to the radially symmetric intensity distribution of the beam on the CCD-camera.

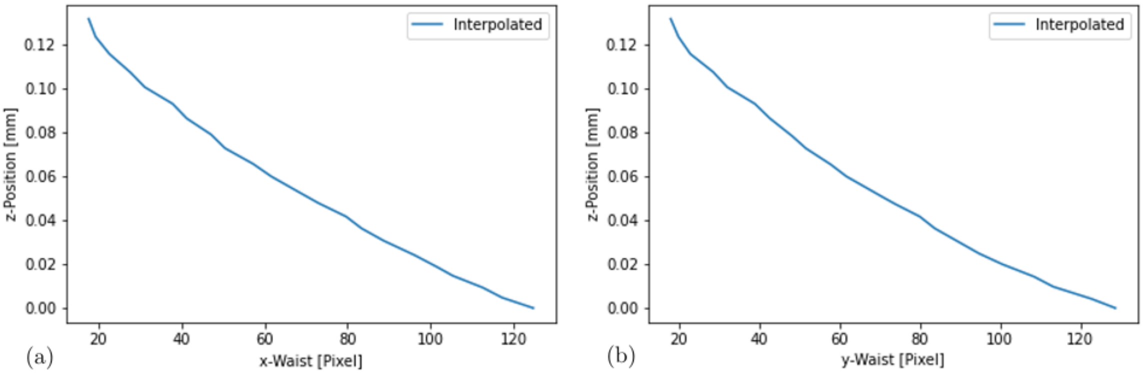

Figure 4.4: Calibration curve in order to determine z-position of the focus on the optical axes: We observe, that the calibration curve using the x-waist calculated from all pixel columns (a) and y-waist calculated from all pixel rows (b) are almost the same.

To observe the transient behavior of the ETL during the switching process, we take a picture every 2 ms after the focus change has started. Because the data acquisition on the CCD and its subsequent transfer via USB takes time on the order of 100 ms, photographing the beam in just one transport switch seems to not possible. Therefore we take one picture per transport and wait till the next transport switch to take the subsequent one. The switching of the focus spot takes place with a repetition rate of 1 Hz. In order to photograph at different times during the transport, we delay the internal trigger of the camera by using the on-board camera clock. We developed a C++ program based on the mvImpact API from Matrix Vision to control all properties of the camera like trigger delay, exposure time or camera gain. In order to check the trigger delay, we also monitor the thread time of the C++ program during the acquisition process.

Atom Transport Characterization Measurement: In order to simulate a part of the atom transport mechanism, we perform a series of measurements where to focal power of the ETL is switched from 1.0 dpt, 0.5 dpt, 0.25 dpt and 0.1 dpt to the resonator's position at 0.0 dpt. For every simulation switch, we measure the trajectory of the dipole traps focus position with the setup and procedure explained above. The results of this measurement are depicted in Fig. 4.5. The actual switching process starts at around 50 ms. The settling time of the ETL's focal power is dependent on the size of a switch. For the switch with a focal change of 1.0 dpt the optical power of the ETL, which translates into the z-position of the focus, has settled after around 50 ms. For a focal power switch of 1.0 dpt applied to the ETL, the system needs more than 100 ms to settle. Between the start and the settling we observe oscillations of the the z-position and therefore of the focal power of the ETL. These oscillations are probably explained by the formation of sound waves inside the liquid as the pressure regulating ring is pushed into the liquid container at the beginning of the switch. The amplitude of the waves increases with the size of the focal power switch applied on the ETL, because more liquid has to be displaced to change the curvature.

In order to understand how the measured trajectories of the focal position of the trap beam affect the atom transport process, we exemplary calculate the acceleration of the trap during the switching process for the biggest measured switch from 1.0 dpt to 0.0 dpt. We fit a polynomial of fifth degree between every set of subsequent data points onto the interesting oscillating area of the measured trajectory. The result of this fit is depicted in Fig. 4.5. The second derivation of the obtained spatial-temporal curve gives the acceleration during the transport process. As we can see in Fig. 4.6, we calculate a maximum acceleration of around $25\,\mathrm{m\,s^{-2}}$. This is more than two orders of magnitude smaller than the maximum acceleration that the dipole trap can exert on the trapped atoms of $5\,000\,\mathrm{m\,s^{-2}}$. Nevertheless, the measured trajectory will potentially result in strong heating of the atoms during the transport process, mostly due to the oscillations of the focal power. Furthermore, the measured trajectory accounts only for one third of the required focal power change of the ETL translating in 15% of the required focal spot position change on the optical z-axes. As the magnitude of the oscillations is scaling with the step size (Fig. 4.5), we should also assume a greater acceleration of at least an order of magnitude. Due to the strong confinement of the atom inside the trap, such a switch should still be feasible to transport the atoms, although with potentially strong heating of the atom.

Another problem with the characterized lens is its low switching speed. As we can deduce from the trajectory depicted in Fig. 4.5, an atom transport process when applying three subsequent 1.0 dpt shots from 0.0 dpt to 3.0 dpt on the ETL would take at least 150 ms to 200 ms. Such a transport time is not short when compared to the measured atom lifetime in the trap of 300 ms and would largely decrease the transport efficiency as well as the experimental repetition rate. In order to tackle both, the transport time and the observed oscillation of the focus position during the transport, we aim to use another new model from *Optotunes* liquid lenses. For future characterization, we will use the *EL-10-30-C-NIR-LD-MV* with a tuning range between −1.5 dpt and 3.5 dpt. Due to the smaller optical diameter and therefore less volume of the liquid inside lens, we expect the lens to provide a better stability of the transport trajectory as well as to decrease the transport time to around 50 ms [36].

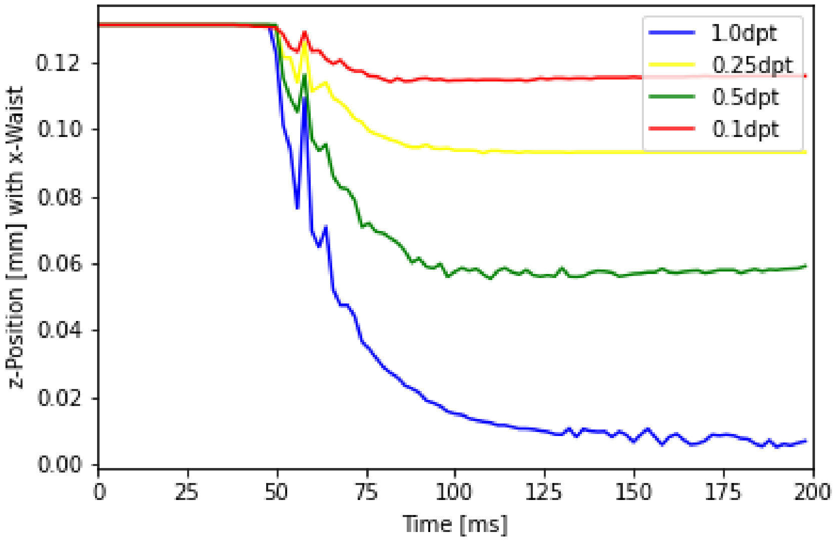

Figure 4.5: Calculated z-position change of the dipole traps focus during a switch of the ETL of 1.0 dpt, 0.5 dpt, 0.25 dpt and 0.1 dpt: We observe oscillations of the focal power and it's corresponding z-position during the switch. The settling time after a sudden switch of the focal power from 1.0 dpt to 0.0 dpt is at least 150 ms. We are just showing the trajectory calibrated by the x-waist as the calibration with the y-waist leads the to almost the same z-position values and therefore same trajectory.

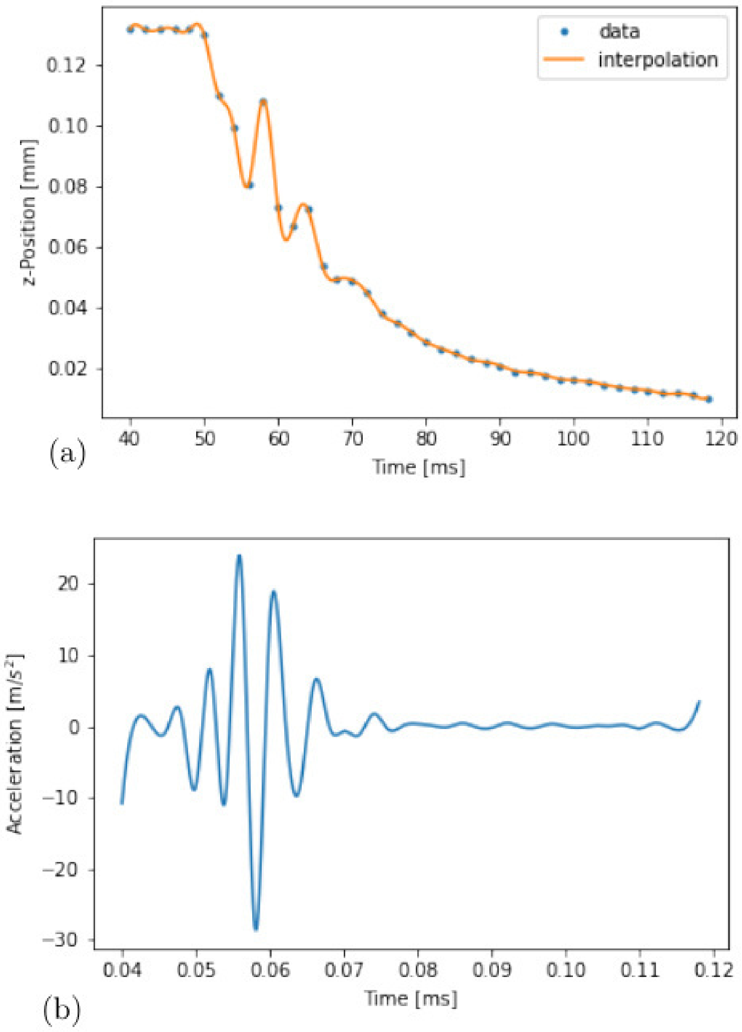

Figure 4.6: Determining the acceleration on the atom trapped inside the moving dipole trap: (a) We fit a polynomial of fifth degree between every set of subsequent data points onto the interesting oscillating area of the measured trajectory in Fig. 4.5. (b) Afterwards we take the second derivative of the interpolated trajectory to determine the acceleration of the atom.

4.1.4 Pointing Stability

As we want to transport atoms to the surface of a WGM microresonator, we have to make sure that atom is always at the same position at the end of the transport process. Therefore we investigate the beam pointing stability in the lateral as well as in longitudinal position. In order to smooth out the focal power change during the switching process, we apply a test ramp consisting of multiple diopter steps as depicted in Tab 4.1. The ramp is repeated each second (1 Hz) to simulate a possible atom transport.

Ramp applied to the ETL		
Step Number	Voltage Level [V]	Diopter Value [dpt]
1	0	3.0
2	0.2	2.8
3	0.6	2.6
4	0.8	2.2
5	1.0	1.5
6	1.2	0.8
7	1.4	0.4
8	1.8	0.2
9	2.0	0.0
10	2.5	3.0

Table 4.1: Voltage to diopter ramp applied on the ETL for measuring the pointing stability.

At the end of the ramp, we magnify the focus with the microscope setup depicted in 4.3. We take a picture with an exposure time of 50 ms of the focus spot approximately 100 ms after triggering the last diopter step to the resonator's position at 0.0 dpt. Before we can begin the measurement we have to evaluate the passive stability of the optical system. For this we performed a long time measurement of 12 hours during the night. Every 10 seconds (or 10 switches), we photographed the focus spot. The result can be seen in Fig. 4.7 (a). We observe a transverse drift of the peak position of about 1 µm over one night. Most of the drift happened in the evening hours between 6.30pm and 8.30pm. Therefore we conclude that the drift is mostly due to slight temperature changes in the labs which leads to changes in the form of the components of the cage systems used. Furthermore, we see in Fig. 4.7 (b) that the drift in the measured waist is negligible indicating that the longitudinal z-position of the focus is stable. By doing a calibration measurement for the z-position as described in the previous chapter, we can conclude that the drift in the waist is smaller than 0.05 dpt which is the smallest focal power change we can apply to the lens. This would correspondent to a z-position focus change smaller than approximately 2 µm. After the passive stability of the measurement setup was characterized, we can measure the beam pointing stability using the setup explained above. We apply the ramp as depicted in Tab. 4.1 to simulate a smooth atom trajectory with a repetition rate of 1 Hz. Again, we magnify the focus with the microscope setup depicted in 4.3 at the end of the ramp. Here we take a picture with an exposure time of 50 ms of the focus spot approximately 100 ms after triggering the last diopter step to the resonator's position at 0.0 dpt. For this measurement, we take a picture of the focus spot after every switch or every second for

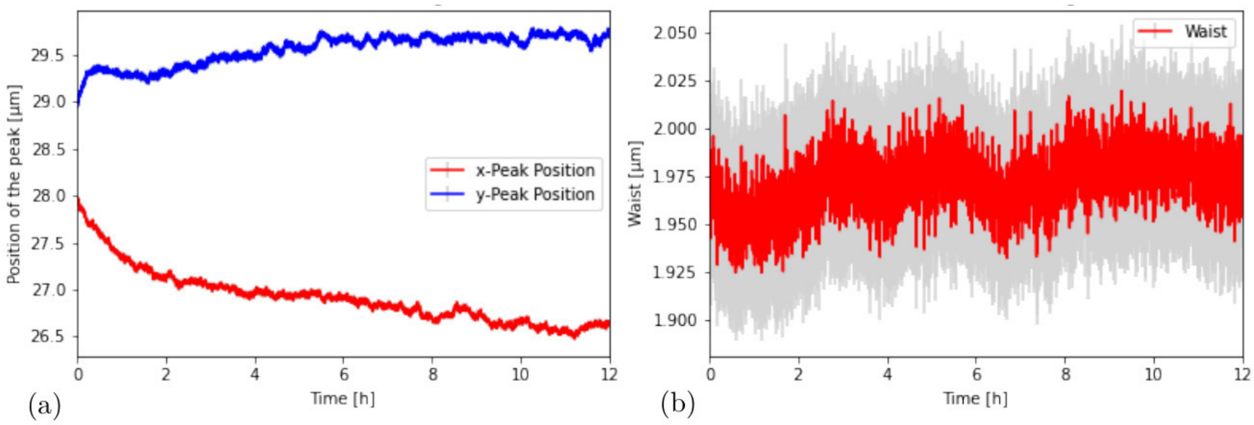

Figure 4.7: Long time measurement for determining the internal stability of the measurement setup described in figure 4.3: Subfigure (a) shows the transversal peak-position of the beam focus in x-direction (red) and y-direction(blue). Subfigure (b) shows the fitted waist. We fitted the x-waist and y-waist onto to rotationally symmetric intensity distribution observed with the CCD-camera (red). The (gray) background shows the averaged error from the x-waist and y-waist measurement calculated with Gaussian propagation of uncertainty.

about 15min.
The results are depicted Fig. 4.8. As we can see from figure Fig. 4.8 (a) the peak position is not changing by more than 400 nm over 1000 repetitions of the trajectory applied for atom transport. This drift is in the same order of magnitude as the thermal drift from the long term measurement. The same is true for the waist change as it is depicted Fig. 4.8 (b). As in the measurement for the determination of the passive stability of our system, the waist change is smaller than 0.05 dpt, which translates to longitudinal position change of much less than 2 µm. For the used lens set, the scanning Erbium-doped nanofiber measurement showed a focus waist size of 1.5 µm. Using Eq.(1.28), we calculate a Rayleigh length of 9 µm. Therefore, we can argue that change of the focus z-position is less than 20% of the Rayleigh range.

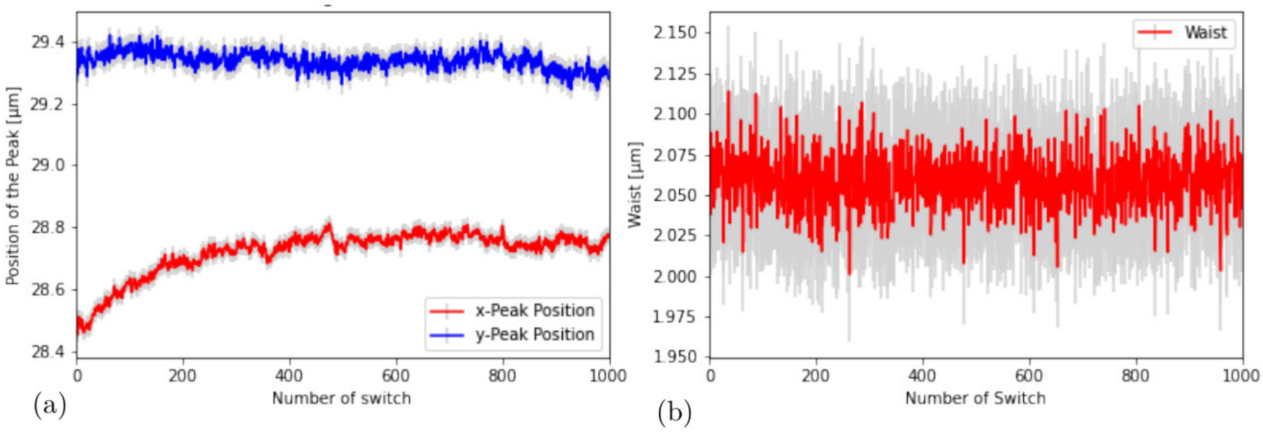

Figure 4.8: Measurement of the pointing stability with the setup depicted in Fig. 4.3 for 1000 simulated atom transport processes with 1 Hz repetition rate: Subfigure (a) shows the transversal peak-position of the beam focus in x-direction (red) and y-direction(blue). Subfigure (b) shows the fitted waist. We fitted the x-waist and y-waist onto to rotationally symmetric intensity distribution observed with the CCD-camera (red). The (gray) background shows the averaged error from the x-waist and y-waist measurement calculated with Gaussian propagation of uncertainty.

4.2 DISCUSSION OF THE STANDING WAVE TRAPPING POTENTIAL

At the end of the atom transport process the dipole traps focus is positioned on the resonator's surface. Due to the interference of the incoming and retroreflected beam from the surface of the resonator a standing wave potential is formed which is largely preventing the trapping of the atom in the evanescent field of the resonator's WGM. First, we introduce a method which partially prevents the formation of the standing wave potential by using a superposition of higher-order Laguerre-Gaussian modes created by a spatial light modulator (SLM). In order to experimentally analyze whether this method is generating the desired trapping potential in the focus spot region of the dipole trap, we developed a measurement technique which can directly measure the standing wave pattern. Therefore, we will also show a proof of concepts measurement using this technique.

4.2.1 TRAPPING NEAR THE RESONATOR'S SURFACE

The goal of the experiment is to study the light-matter interaction of the atom in the evanescent electric field of the WGM bottle-resonator in the strong coupling regime of cavity quantum electro-dynamics. In order to reach that regime, the coherent energy exchange between the light field and the atom, described by the coupling strength g, has to be much larger than the field decay rates of the atom γ and the resonator losses κ. In general CQED this can be expressed as:

$$\frac{g^2}{\kappa\gamma} \gg 1. \tag{4.5}$$

When studying the quantized light-matter interaction by using the Jaynes-Cummings model [1] [15], the coupling strength g is proportional to electric field generated by a single photon that is distributed over the mode volume V and the electric dipole matrix element d by

$$g = \sqrt{\frac{\omega}{2\hbar\epsilon_0 V}} d \cdot \eta(\vec{r}), \tag{4.6}$$

where $\eta(\vec{r})$ includes the spatial dependence of the electric field of the resonator mode. As we want to trap in the exponentially decaying field of the whispering-gallery mode outside of the resonator, the coupling strength depends strongly on the distance to the resonator surface d

$$g(r) = g_0 e^{r/r_a}. \tag{4.7}$$

Here r_a is the attenuation length. For a 36 µm diameter WGM resonator and for the TM polarized fundamental resonator mode, the attenuation length was calculated to be 131 nm with a coupling strength at the surface of $g_0 = 2\pi \cdot 56\,\mathrm{MHz}$ [37]. According to this, we have to trap the single atoms as close as possible to the resonator's surface in order to set our experiment well in regime of strong coupling.

As the atom is placed in front of the resonator, it is also interacting radiatively with the the surface of the resonator. A Van der Waals potential is created by the induced dipole-dipole interaction of the Rubidium atom and the surface. The surface potential is generally attractive, such that we have to prevent the atom from falling onto the resonator surface.

In order to tackle both challenges, we have to create a trapping potential which has a trapping minimum at a distance of a few hundred nanometers from the surface and is strong enough to counteract the Van der Waals potential. To realize this, we position the focus of the dipole trap on the surface of the resonator at the end of the atom transport process with the ETL. The dipole trap is reflected from the resonator's surface, such that the incoming and retro-reflected beams interfere and generate a standing wave pattern in front of the surface. Thus, we are creating $n+1$ multiple trapping potential minima which are located at the positions $[n \cdot \lambda/2] + \lambda/4$ from the surface. With the formed standing wave potential, we can counter the Van der Waals forces. However as depicted in purple of Fig. 4.9, this would also lead to a higher probability of trapping the atoms in a local trap minima greater than the attenuation length of the coupling strength. Consequently, reaching the strong coupling regime gets more unlikely in such a setup. This consideration is valid for the fundamental Gaussian mode of a laser beam which exhibits a high-contrast standing wave over many 10's of microns. As it is shown in [25], we can use higher-order Laguerre-Gaussian modes to maximize the probability of trapping atoms in the first potential minima at distance $\lambda/4$ from the surface. The general solutions of the paraxial Helmholtz equation in cylindrical coordinates are given by the Laguerre-Gaussian modes [23] as

$$U_p(r,z) \propto \frac{1}{w(z)} \exp\left(-\frac{r^2}{w(z)^2}\right) \exp\left(-ik\frac{r^2}{2R(z)}\right) \cdot L_p^l\left(\frac{2r^2}{w(z)^2}\right) \exp(ikz\Psi(z)). \tag{4.8}$$

Here L_p^l stands for the generalized Laguerre polynomials, $w(z)$ for the beam radius at the position z, $k = 2\pi/\lambda$ for the wave vector and $R(z)$ for the radius of curvature. The last term in equation 4.8 refers to the Gouy phase shift and is the only term besides L_p^l which is dependent on the radial mode number p given by

$$\Psi(z) = (2p+1)\arctan\left(\frac{z}{z_R}\right). \tag{4.9}$$

Therefore the frequency of the phase evolution around the beam focus is different for radial Laguerre-Gaussian modes with different radial mode number p. One can exploit this effect to change the standing wave pattern close to the resonator's surface by generating a superposition of higher order Laguerre-Gaussian beams with, for example, the SLM. In more detail, we want to apply a superposition of the three $p = 0, 2, 4$ radial Laguerre-Gaussian modes. Due to the resulting rapid spatial variation of the Gouy phase, the interference pattern between the incident and retroreflected trap beam at the resonator will only be constructive for a distance of around $\lambda/2$ from the resonator's surface. At larger distances the phases of the different Laguerre-Gaussian modes are no longer in phase such that no high contrast interference is visible. The suppressed standing wave trapping potential is depicted in the upper half of Fig. 4.9 with the red curve calculated from the Kimble group [25]. This will allow for an atom transport into the first trapping minimum of a distance of $\lambda/4$ to the surface with high probability. In the lower half of Fig. 4.9, we see the results of a Monte Carlo simulation by [25] for the probability of trapping an atom in the different potential minima after the focus of the dipole trap is moved to the surface of a planar dielectric surface. The purple bar diagram shows the probabilities of trapping the atom in the standing wave potential minimal when using a fundamental Gaussian TEM_{00} mode. By applying the superposition of the three $p = 0, 2, 4$ radial Laguerre-Gaussian modes we can see from the orange bars, that the probability of trapping the atoms in the first and second potential minima close to the resonator surface is greatly increased. This would yield a loading probability of 70% for the trap minimum closest to the resonator's surface.

4.2.2 Measuring a Standing Wave Potential

A crucial building block to implement such a complex experimental procedure is to develop a method to measure the standing wave potential in front of the resonator surface in order to verify that the desired interference pattern is really generated. For this we need a very thin probe on a scale of a few 100 nm which can detect the intensity modulation in front of the resonator. Two possible options to realize such a probe are feasible to setup in our laboratories.

The first option is to use a bare single mode nanofiber and put a gold nanoparticle with a diameter of 100 nm on it. As we scan the nanofiber with the particle through the standing wave potential, the gold particle would efficiently scatter the dipole trap light into the the guiding mode of the nanofiber [38]. Nevertheless, putting a small particle of a size of around 100 nm on top of a nanofiber with a diameter of 300 nm is an experimentally delicate task and was not attempted during the scope of this thesis.

In order to characterize the standing wave potential we plan to employ a technique based on an Erbium-doped optical nanofiber as already introduced in chapter 2. As it is depicted in Fig. 4.10, for testing purposes, we put a nanofiber with a diameter of 300 nm onto a translation stage and use the internal 3-axis piezos of the stage (Thorlabs NanoMax381)

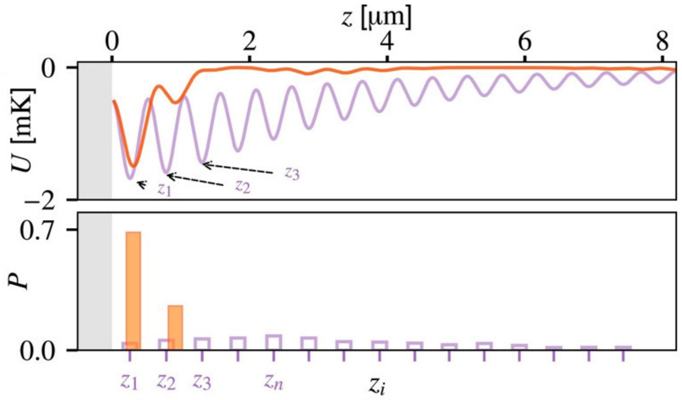

Figure 4.9: Simulation of the atom delivery with a changing focus dipole trap: At the end of the transport process, the focus is placed at the surface of a planar dielectric mirror. (Upper Part) Calculation of the standing wave trapping potential when using a fundamental Gaussian TEM_{00} mode [purple] and when applying a superposition of the three $p = 0, 2, 4$ radial Laquerre-Gaussian modes [red]. (Lower Part) Monte Carlo simulation for the probabilities to deliver the atoms in the different potential minima of the standing wave trap using a fundamental Gaussian TEM_{00} mode [purple] and when applying a superposition of the three $p = 0, 2, 4$ radial Laguerre-Gaussian modes [orange]. Data and plot from [25].

to precisely position the Erbium-doped nanofiber. These closed loop piezos are used for fine alignment of the nanofiber around the beam focus because they have a traveling range of 20 µm. For coarse alignment we use 3-axis stepper motors (Thorlabs DRV2008) with a traveling range of 8 mm. For testing this method, we built up a simple 1 :1 microscope consisting of two diffraction limited lenses with a focal length of 50 mm yielding a focus waist of approximately 2.6 µm as measured in chapter 2. For this proof of concept measurement the beam gets reflected from the surface of a small gold plated mirror at the left hand side of Fig. 4.10 to create a fully modulated standing wave potential. For alignment purposes the mirror is placed onto two stepper motors (Physik Instrumente M237.1) which can move in the longitudinal z-direction and vertical x-direction with a traveling range of 20 mm. We collect the generated upconverted photons at around 540 nm with an SPCM on one side of the fiber, as the Erbium-doped nanofiber is moving longitudinally through the standing wave potential. We filter out residual trap light by using two short pass filters at 700 nm (Thorlabs FESH0700) with an optical density of 5 per filter.

First results of the proof of concept measurement are depicted in Fig. 4.11. The measurement is performed roughly two Rayleigh lengths before the focus, which is on the left side of the figure. We observe a clear sinusoidal modulation of the detected photons. As introduced in chapter 2.3, we corrected the count rate before plotting by the conversion efficiency c as well as by the dead time of the SPCM. Furthermore, we see a clear increase of background counts and of the amplitude of the modulation as we move in longitudinal z-direction closer to the focus at the mirror. In order to verify that the observed potential is indeed generated by the interference of the incident and reflected trapping beam, we fit

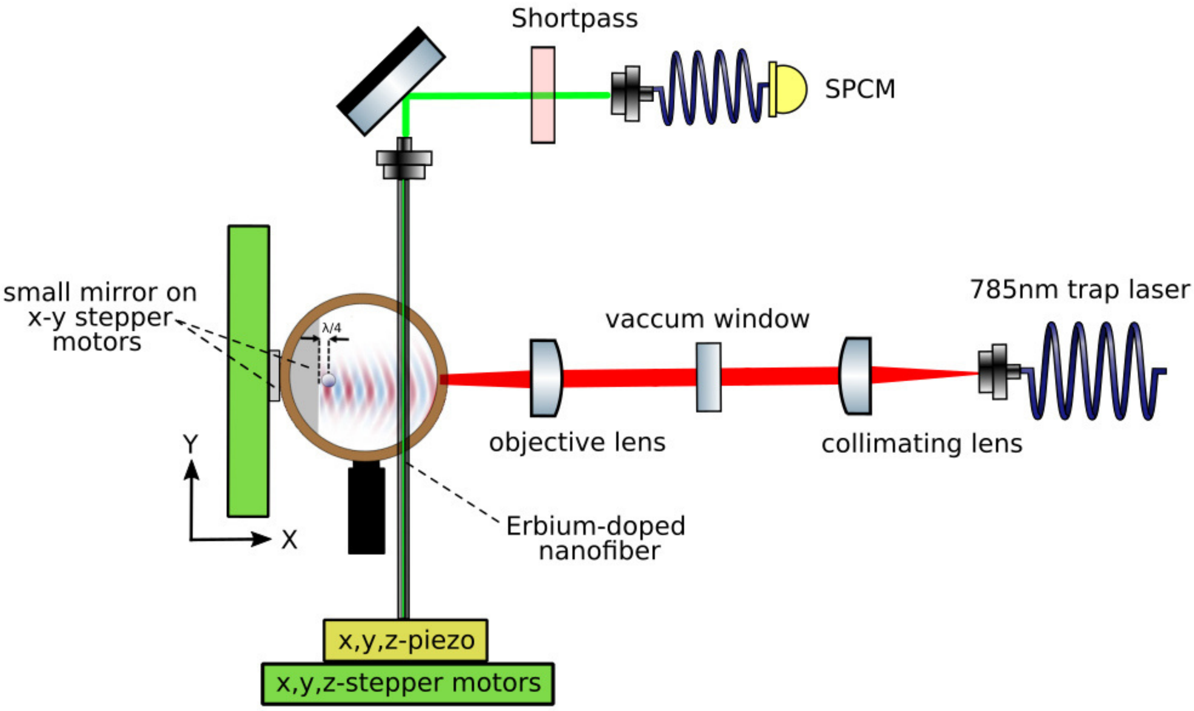

Figure 4.10: Setup used to characterize the standing wave potential: A core Erbium-doped optical nanofiber with a diameter of 300 nm moves longitudinally on the z-axis through the standing wave potential. The standing wave potential is created by the interference of the incident and retro-reflected dipole trap beam at the mirror. On one side of the fiber, we detect the upconverted photons at around 540 nm, after the signal passed two shortpass filter with a optical density of 5.

the following function to the data

$$f(z) = a + zb \left[(c + zd) \cdot \sin \left(\frac{2\pi z}{\lambda/2} + e \right) \right]. \tag{4.10}$$

This leads to a fitted wavelength λ of 774 nm which is close to the wavelength of the used dipole trap at 784.6 nm. The small discrepancy can be explained by a slight decrease in the trapping potential period due to the Gouy phase as we use a Gaussian beam to generate the standing wave pattern. Nevertheless this effect should be minor as we are two Rayleigh ranges away from the surface. Furthermore, we observe a relatively low visibility of the standing wave pattern. One reason for that result is, that the nanofiber probe with a diameter of 300 nm itself is not small compared to the distance $\lambda/4$ between a maximum and minimum intensity. Therefore, the nanofiber is collecting light from a relative large region of the sinusoidal modulated pattern. Additionally, we can not make sure that the nanofiber is placed parallel to the standing wave pattern. That also leads to a decrease of the visibility as the fiber is scanned with the fiber axis non-perpendicular to the beam axis through the beam, and is collecting light from a certain region of longitudinal z-positions. Using a nanoparticle placed on a thin optical nanofiber offers a smaller diameter 100 nm probe which would lead to an increased visibility. Furthermore, the visibility of the standing wave pattern should be increased, as we would not have issues with paralleling the 1-dimensional probe with respect to the standing wave patter. Nevertheless, the visibility when using the Erbium-doped nanofiber would be increased as well when we approach the resonator's surface where the diameter of the focused dipole trap is much smaller.

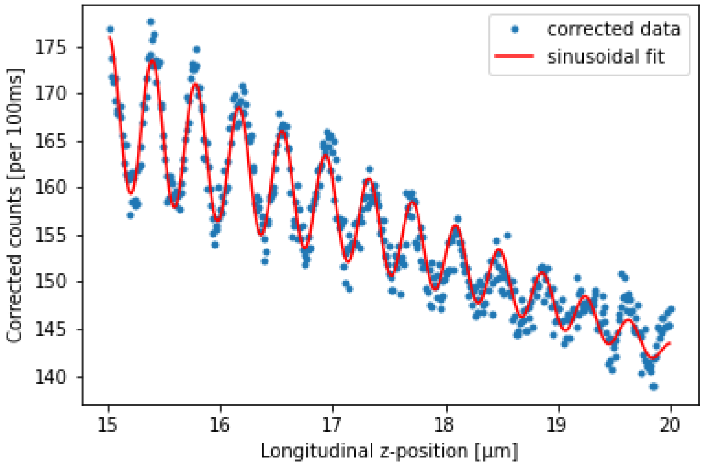

Figure 4.11: Measurement of the dipole traps standing wave potential in front of a small gold mirror. We observe a sinusoidal modulation of the standing wave trapping potential at approximately two Rayleigh lengths before the focus. Fitting the data to Eq.(4.10) gives a wavelength λ of 774 nm which is close to the wavelength of the used dipole trap at 784.6 nm.

In the last chapter of this thesis, we examined the first steps towards the realization of atom transport into the resonator's WGM in our experiment. First, we explored the feasibility to use a moveable focus optical dipole trap generated by *Optotunes* liquid lens *EL-16-40-TC-VIS-20D* for atom transport. The measurement of the pointing stability shows that the end position of the atom transport process is stable within the passive stability of our setup and measurement errors. The examination of the transient optical response of the ETL indicates, that we can possibly transport the atom in the dipole trap from the MOT to the resonator position when applying a fast cascade of three 1.0 dpt switches. Due to the long transport time and oscillations of the focus spot position during the transport, we would strongly heat the atom in the dipole trap and also have to work with a reduced transport efficiency and experimental repetition rate. Afterwards, we discussed the experimental challenges connected with trapping single ^{85}Rb-Atoms in the whispering-gallery mode of the resonator. In order to reach the strong coupling regime of CQED, we introduced a method to suppress the standing wave pattern. As shown above, this can be done by superimposing radial higher-order Laguerre-Gaussian modes such that the resulting rapid spatial variation of the Gouy phase only leads to constructive interference of the incoming and reflected beam for a distance of around $\lambda/2$ from the resonator's surface. To characterize the modulated standing wave pattern, we demonstrated a technique based on an Erbium-doped optical nanofiber. A proof of concept was successfully shown as we were able to measure the modulation of the trapping potential two Rayleigh lengths away from the surface of a small gold mirror.

Summary and Outlook

The goal of this thesis was to design, set up and characterize a new optical system to trap single ^{85}Rb-atoms inside a dipole trap and to collect their fluorescence. Furthermore, we wanted to study ways to transport the trapped atoms to the surface of a WGM microresonator to reach the strong coupling regime.

In order to realize single atom trapping and fluorescence collection, we developed and built a confocal microscope system which is creating a tightly focused dipole trap that reaches the collisional blockade regime where only single atoms can be cooled in the trap. We characterized the focus spot region of the confocal microscope for different collimation and objective lenses by using three different measurements techniques: a knife edge method, imaging via a high-quality optical microscope and a newly developed technique based on the Erbium-doped nanofiber probe. As discussed during the characterization measurements, the novel method seems to be well suited to measure tight focus spots (around 1.0 µm waist radius) as well as more complex intensity distributions of the focused beam.

Using the characterized setup, we successfully realized the trapping of the single ^{85}Rb-atoms with a lifetime of $\tau = 300\,\mathrm{ms}$ inside the dipole trap. Furthermore, we verified that only single atoms can be trapped by measuring the second order correlation function $g^{(2)}(\tau)$ in a Hanbury-Brown Twiss setup. From this we observed photon anti-bunching and calculated $g^{(2)}(0)$ to be approximately 0.02 ± 0.05. In the near future, we will also determine the trapping frequencies, the trapped atom temperature, as well as an improved atom lifetime when the MOT-lasers are turned off after successfully loading the trap.

We plan to realize the atom transport from the MOT to the resonator's position by changing the position of the dipole traps focus using an ETL. For this, we studied the feasibility of atom transport using Optotunes EL-16-40-TC liquid lens. From imaging the trap beams focus, we concluded that the focus spot position at the end of the transport process fluctuates less than the passive stability of our setup and is within our measurement errors, compatible with a perfect reproducibility of the focus spot's position at the end of the transport process. Furthermore, we also measured the time dynamics of the focal length change of the ETL. Our results show that this system should be able to transport the atoms from the MOT to the WGM resonator's position. Since the transport with the measured lens is however quite slow and we can not precisely control the overall trajectory, we will use a potentially faster electric tunable lens from Optotune which should allow for a more stable transport trajectory.

One challenge of the transport mechanism is that after the moving of the dipole trap's focus to the surface of the resonator, a standing wave potential is formed due to the inference of the incident and retroreflected beam from resonator's surface. This standing wave potential would prevent the atom from reaching the evanescent field of the resonator's WGM. We plan to use an optical dipole trap composed of a superposition of higher order Laguerre-Gaussian modes generated by a spatial light modulator to suppress the standing wave structure. To experimentally analyze if this suppression works, we developed a method based on the already used Erbium-doped nanofiber probe for the in-situ measurement of the standing wave pattern close to the resonator. In the framework of this thesis, we performed a proof of concept measurement of this method with the dipole trap focused onto a small gold mirror where we could resolve the standing wave structure. As a next step, we want to test our method using a more cylindrical surface such as a gold-coated microfiber with a diameter matching that of the WGM resonator's. Furthermore, is is still necessary to study and optimize the temporal response of our method to be able to resolve the standing wave pattern directly in front of the surface when the nanofiber probe will be accelerated towards the resonator's surface by Van der Waals forces.

In summary, we realized a setup for trapping and observing single atoms and we performed crucial characterization measurements for the future atom transport process. These are major steps towards the realization of a deterministic delivery of single atoms into the evanescent field of the resonator's WGM.

BIBLIOGRAPHY

[1] E. Jaynes and F. Cummings, "Comparison of Quantum and Semiclassical Radiation Theories with Application to the Beam Maser", Proceedings of the IEEE **51**, 89 (1963).

[2] The Royal Swedish Academy of Sciences, *The Nobel Prize in Physics 2012*, Retrieved 7. January 2021, Available at `https://www.nobelprize.org/prizes/physics/2012/summary`, 2021.

[3] J. Ye et al., "Trapping of Single Atoms in Cavity QED", Physical Review Letters **83**, 4987 (1999).

[4] P. W. H. Pinkse et al., "Trapping an Atom with Single Photons", Nature **404**, 365 (2000).

[5] A. Reiserer and G. Rempe, "Cavity-based Quantum Networks with Single Atoms and Optical Photons", Reviews of Modern Physics **87**, 1379 (2015).

[6] M. Brune et al., "Quantum Rabi Oscillation: A Direct Test of Field Quantization in a Cavity", Physical Review Letters **76**, 1800–1803 (1995).

[7] K. J. Vahala, "Optical Microcavities", Nature **424**, 839 (2003).

[8] M. Pöllinger et al., "Ultrahigh-Q Tunable Whispering-Gallery-Mode Microresonator", Physical Review Letters **103**, 053901 (2009).

[9] A. B. Matsko and V. S. Ilchenko, "Optical Resonators with Whispering-Gallery Modes Part I and II", IEEE Journal of Selected Topics in Quantum Electronics **12**, 3 (2006).

[10] P. Lodahl et al., "Chiral Quantum Optics", Nature **541**, 473 (2017).

[11] E. Will et al., "Coupling a Single Trapped Atom to a Whispering-Gallery-Mode Microresonator", Physical Review Letters **126**, 233602 (2021).

[12] J. D. Thompson et al., "Coupling a Single Trapped Atom to a Nanoscale Optical Cavitys", Science **340**, 1202 (2013).

[13] T. Hänsch and A. Schawlow, "Cooling of Gases by Laser Radiation", Optics Communications **13**, 68 (1975).

[14] E. L. Raab et al., "Trapping of Neutral Sodium Atoms with Radiation Pressure", Physical Review Letters **59**, 2631 (1987).

[15] M. Fox, *Quantum Optics*, 1st ed. (Oxford Unversity Press, Oxford, New York, 2006), pp. 216–238.

[16] C. J. Foot, *Atomic Physics*, 1st ed. (Oxford Unversity Press, Oxford, New York, 2005), pp. 179–213.

[17] W. Alt, “Optical Control of Single Neutral Atoms”, PhD thesis (Rheinischen Friedrich-Wilhelms-Universität Bonn, 2004).

[18] A. Ashkin, “Trapping of Atoms by Resonance Radiation Pressure”, Physical Review Letters **40**, 729 (1978).

[19] The Royal Swedish Academy of Sciences, *The Nobel Prize in Physics 2018*, Retrieved 7. January 2021, Available at `https://www.nobelprize.org/prizes/physics/2018/summary`, 2021.

[20] R. Grimm and M. Weidemüller., “Optical Dipole Traps for Neutral Atoms”, Advances In Atomic, Molecular, and Optical Physics **42**, 95 (2000).

[21] N. Schlosser et al., “Collisional Blockade in Microscopic Optical Dipole Traps”, Physical Review Letters **89**, 023005 (2002).

[22] S. J. M. Kuppens et al., “Loading an Optical Dipole Trap”, Physical Review A **62**, 013406 (2000).

[23] A. E. Siegman, *Lasers*, 1st ed. (University Science Books, Sausalito, 1986), pp. 625–653.

[24] Thorlabs, *Datasheet: PM780-HP Fiber*, Retrieved 7. January 2022, Available at `https://www.thorlabs.com/_SD-Popup.cfm?partnumber=PM780-HP&pageId=1596`, 2017.

[25] J. B. Beguin et al., “Reduced Volume and Reflection for Bright Optical Tweezers with Radial Laguerre–Gauss Beams”, PNAS **117**, 26109 (2020).

[26] Optotune AG, *Datasheet: EL-10-30-Series*, Retrieved 14. January 2022, Available at `https://www.optotune.com/el-10-30-c-lens`, 2021.

[27] B. E. Saleh and M. C. Teich, *Fundamentals of Photonics*, 2nd ed. (John Wiley and Sons, Hoboken, 2007), pp. 86–90.

[28] T. S. Ross, *Laser Beam Quality Metrices*, 1st ed. (SPIE Press, Bellingham, 2013), pp. 171–174.

[29] International Organization for Standardization, *ISO 11146-1 Lasers and Laser-related Equipment — Test Methods for Laser Beam Widths, Divergence Angles and Beam Propagation Ratios. Part 1 Stigmatic and Aimple Astigmatic Beams*, First edition from 15. January 2005, Available at `https://www.iso.org/standard/33625.html`.

[30] D. Wang et al., “Synthesis and NIR-to-violet, Blue, Green, Red Upconversion Fluoresence of Er^{3+} : LaOBr”, Journal of Alloys and Compounds **397**, 1 (2005).

[31] M. Pollnau et al., “Power Dependence of Upconversion Luminescence in Lanthanide and Transition-metal-ion Systems”, Physical Review Letters B **61**, 3337 (2000).

[32] R. Loudon, *The Quantum Theory of Light*, 3rd ed. (Oxford Unversity Press, Oxford, New York, 2000), pp. 107–124.

[33] R. H. Brown and R. Q. Twiss, “Correlation between Photons in two Coherent Beams of Light”, Nature **177**, 27 (1956).

[34] D. Schrader et al., “An Optical Conveyor Belt for Single Neutral Atoms”, Applied Physics B **73**, 819 (2001).

[35] Opotune AG, *Tunable Lens. European Patent Application EP 2860555A1*, Retrieved 10. January 2021, Available at `https://patentimages.storage.googleapis.com/41/2b/58/abb93ff717a246/EP2860555A1.pdf`, 2015.

[36] C. Dorronsoro et al., “Tunable lenses: Dynamic Characterization and Fine-tuned Control for High-speed Applications”, Optics Express **27**, 2085 (2019).

[37] M. Scheucher, “Single-atom Cavity Quantum Electrodynamics with Whispering-gallery-modes: Single-photon Nonlinearity and Nonreciprocity”, PhD thesis (Technische Universität Wien, 2017).

[38] M. Joos, “Dispositifs Hybrides: Nanoparticules Couplées à une Nanofibre Optique”, PhD thesis (Sorbonne University, 2018).

DANKSAGUNG

Zuerst möchte ich Prof. Arno Rauschenbeutel dafür danken, mir die Möglichkeit gegeben zu haben, in seiner inspirierenden Arbeitsgruppe meine Masterarbeit durchführen zu können. Er hatte immer ein gutes Gespür dafür, wann es an der Zeit war, ein Labormeeting mit ihm abzuhalten, um das Experiment in kritischen Momenten voranzubringen.

Des Weiteren danke ich Dr. Tim Schröder dafür als Zweitgutachter meiner Masterarbeit zur Verfügung zu stehen.

Ein besonderer Dank gebührt meinen beiden direkten Betreuern Dr. Jürgen Volz und Luke Masters, mit denen ich zu jeder Zeit meine Fragen diskutieren konnte und ohne die ich diese Arbeit nicht hätte schreiben können. In diesem Zusammenhang müssen auch Dr. Xinxin Hu und Gabriele Maron erwähnt werden, die ich mich tagtäglich im Labor ausgehalten haben und an die ich mich immer bei Problemen wenden konnte. Ohne ihre ausdauernde Arbeit hätten besonders die erfolgreichen Experimente zum Fangen und Detektieren der einzelnen Atome und zur Messung des Standing Wave Patterns nicht so in dieser Arbeit beschrieben werden können.

Des Weiteren möchte ich besonders Dr. Sofia Pazzagli danken, die während meiner Zeit an der Masterarbeit immer für ein gutes Gespräch zu haben war.

Besonders hervorzuheben ist auch die offene, freundschaftliche, kuchenlastige und koffeinhaltige Arbeitsatmosphäre der gesamten Forschungsgruppe, die einen immer wieder motiviert ins Labor zu gehen.

Außerordentlich dankbar bin ich meiner Familie, die mir während der mittlerweile langen Zeitdauer des Studiums immer den Rücken freigehalten haben. Besonders dankbar bin ich dafür, dass ich kurz vor Beginn meiner Masterarbeit Rissy kennenlernen durfte. Mit dir bin ich zwar nicht im Physikalischen auf einer Wellenlänge, dafür aber in Resonanz bei den wirklich wichtigen Dingen in unserem Leben. Eigentlich als Erstes müsste ich mich bei meinen Freunden bedanken, die mich auf meinem bisherigen Weg begleitet haben und auf die man auch in Zukunft bauen kann.

Selbstständigkeitserklärung

Ich erkläre hiermit, dass ich die vorliegende Arbeit selbstständig verfasst und noch nicht für andere Prüfungen eingereicht habe. Sämtliche Quellen einschließlich Internetquellen, die unverändert oder abgewandelt wiedergegeben werden, insbesondere Quellen für Texte, Grafiken, Tabellen und Bilder, sind als solche kenntlich gemacht. Mir ist bekannt, dass bei Verstößen gegen diese Grundsätze ein Verfahren wegen Täuschungsversuchs bzw. Täuschung eingeleitet wird.

Berlin, 14.01.2022